

# **Digital Test of Composite Material Using X-Ray Tomography and Finite Element Simulation**

Bing Zhang

Dissertation submitted to the faculty of  
Virginia Polytechnic Institute and State University  
in partial fulfillment of the requirements for the degree of

Doctor of Philosophy

in

Civil Engineering

Linbing Wang, Chair  
Michael J. Duncan  
Gerardo W. Flintsch  
Marte S. Gutierrez  
John J. Lesko

May 14, 2007

Blacksburg, Virginia

Keywords: Digital Test, X-ray Tomography, Finite Element, Composite Material

Copyright 2007, Bing Zhang

# **DIGITAL TEST OF COMPOSITE MATERIAL USING X-RAY TOMOGRAPHY AND FINITE ELEMENT SIMULATION**

Bing Zhang

## **(ABSTRACT)**

Characterization of composite materials, such as Asphalt Concrete (AC) and other engineering materials is required to provide data for design and construction. This is usually carried out through various performance tests, which are always time consuming for specimen preparation, equipment calibration and test setting up. For materials with time- and temperature-dependent properties, this procedure requires fabrication of a large number of specimens in order to get reasonably comprehensive results. Furthermore, for materials that consist of phases with significant differences in properties, macroscopic homogeneous assumption or microscopic statistic approximation will lead to complex correction schemes. This will add complexity in material characterization. On the other hand, the homogeneity based interpretation of test results makes it difficult to understand the interaction between different components. The objective of this research is to develop a numerical testing method for material characterization based on x-ray tomography and finite element method. The introduction of tomography technology, such as x-ray tomography into engineering field makes it possible to obtain material microstructure without disturbing the phase configuration. Along with the development of image analysis technology, image data can be manipulated to obtain digitalized sample reconstruction and to build finite element geometric model. Based on well developed material models that sufficiently capture the essential behavior of individual material component, we developed a framework of numerical tests for characterization of composite material. The geometric model imports the microstructural data of the sample, the configuration of aggregates, voids and flakes, through x-ray tomography and image processing. The voids distribution as well as density variation was quantified to verify the model microscopic characteristics. FORTRAN programs were developed to automatically achieve data transfer and model generation, e.g. boundary identification and ABAQUS simulation model generation. Material model was studied and selected for different material components. Viscoplastic material models were evaluated and calibrated in ABAQUS. Monotonic loading and repeated loading were considered in the study to validate the model for most characterization needs. The digital model was validated through small sample tests and was implemented and used in various material characterizations. For the wood panel characterization, the anisotropic elastic properties were studied while the viscous and plastic responses were studied for asphalt concrete. Factors affecting the accuracy and the limitations of the application were determined. It is worth noting that further advance and data collection will make the calibration of material model more accurate. Nevertheless, the work can be extended to other regimes, such as high speed impact especially where the actual testing is complicated to setup.

**This dissertation is dedicated to my wife Yanli, and our son Yuning.**

## **ACKNOWLEDGEMENT**

The author wants to thank his advisor, Dr. Linbing Wang for his patient supervision, encouragement and support. His valuable and constructive advice and comments are greatly appreciated.

The author also wants to thank his advisory committee members, Dr. Michael J. Duncan, Dr. Gerardo W. Flintsch, Dr. Marte S. Gutierrez and Dr. John J. Lesko, for their valuable advices and support during coursework and dissertation preparation.

The author would like to thank his colleagues and friends for their help both in and out of office and laboratory.

The research was made possible with the support from the Department of Civil and Environmental Engineering and VTTI of Virginia Tech.

# CONTENT

<b>CHAPTER 1</b>	<b>INTRODUCTION .....</b>	<b>1</b>
1.1	BACKGROUND.....	1
1.2	RESEARCH OBJECTIVES .....	2
<b>CHAPTER 2</b>	<b>LITERATURE REVIEW .....</b>	<b>4</b>
2.1	X-RAY TOMOGRAPHY IMAGING.....	4
2.2	MATERIAL CONSTITUTIVE MODELS.....	4
2.2.1	<i>Viscoelastic material models .....</i>	<i>5</i>
2.2.2	<i>Viscoplastic material models.....</i>	<i>6</i>
2.2.3	<i>Strain decomposition models (strain additivity).....</i>	<i>9</i>
2.2.4	<i>Multi-layer models (stress overlay).....</i>	<i>10</i>
2.2.5	<i>Microstructural considerations .....</i>	<i>11</i>
2.3	PARAMETER ESTIMATION.....	13
<b>CHAPTER 3</b>	<b>METHOD AND ORGANIZATION.....</b>	<b>15</b>
3.1	APPROACH .....	15
3.2	ORGANIZATION .....	15
<b>CHAPTER 4</b>	<b>CHARACTERIZATION OF WOOD COMPOSITE.....</b>	<b>18</b>
4.1	VOID STRUCTURE CHARACTERIZATION .....	18
4.1.1	<i>Introduction .....</i>	<i>18</i>
4.1.2	<i>Material and method .....</i>	<i>19</i>
4.1.3	<i>Result and discussion.....</i>	<i>21</i>
4.1.4	<i>Conclusions .....</i>	<i>28</i>
4.2	THE INFLUENCE OF IN-PLANE DENSITY VARIATION ON ENGINEERING PROPERTIES OF ORIENTED STRANDBOARD: A FINITE ELEMENT SIMULATION .....	28
4.2.1	<i>Introduction .....</i>	<i>28</i>
4.2.2	<i>Materials and method.....</i>	<i>29</i>
4.2.3	<i>Results and discussion .....</i>	<i>33</i>
4.2.4	<i>Conclusions .....</i>	<i>42</i>
4.3	CHARACTERIZATION OF ENGINEERING PERFORMANCE OF ORIENTED STRANDBOARD WITH COMBINED COMPUTER TOMOGRAPHY AND FINITE ELEMENT TECHNIQUES .....	42
4.3.1	<i>Panel geometry model .....</i>	<i>42</i>
4.3.2	<i>Finite element model .....</i>	<i>43</i>
4.3.3	<i>Results and discussion .....</i>	<i>43</i>
4.3.4	<i>Conclusions .....</i>	<i>44</i>
4.4	ACKNOWLEDGMENT .....	45
<b>CHAPTER 5</b>	<b>STRESS NON-UNIFORMITY IN INDIRECT TENSILE TEST .....</b>	<b>61</b>
5.1	INTRODUCTION.....	61
5.2	METHODS.....	62
5.2.1	<i>X-ray tomography imaging, analysis and microstructure model.....</i>	<i>62</i>
5.2.2	<i>Theoretical solution for indirect tensile test.....</i>	<i>62</i>
5.2.3	<i>FEM model construction .....</i>	<i>63</i>
5.3	RESULTS AND DISCUSSIONS.....	64
5.4	CONCLUSIONS.....	65
5.5	ACKNOWLEDGEMENT.....	65
<b>CHAPTER 6</b>	<b>VISCOPLASTIC PARAMETRIC STUDY OF ASPHALT CONCRETE .....</b>	<b>79</b>
6.1	INTRODUCTION.....	79
6.2	THEORETICAL ELASTIC SOLUTION .....	80
6.3	MACROSCOPIC STUDY – VISCOPLASTIC SIMULATION .....	80

6.3.1	<i>Finite element model</i> .....	80
6.3.2	<i>Material model</i> .....	82
6.3.3	<i>Numerical experiment</i> .....	84
6.3.4	<i>Physical experiment</i> .....	85
6.3.5	<i>Parameter back calculation</i> .....	86
6.4	MICROSCOPIC STUDY .....	101
6.5	CONCLUSIONS .....	104
<b>CHAPTER 7 SMALL SAMPLE TESTING AND SIMULATION .....</b>		<b>105</b>
7.1	INTRODUCTION.....	105
7.2	METHODS.....	105
7.2.1	<i>Testing sample design and preparation</i> .....	105
7.2.2	<i>Sample scanning and testing</i> .....	110
7.2.3	<i>Sample reconstruction, test simulation and parameter back calculation</i> .....	112
7.3	RESULTS AND DISCUSSIONS.....	113
7.3.1	<i>Sample scanning and reconstruction</i> .....	113
7.3.2	<i>Volume fraction of aggregates and voids</i> .....	114
7.3.3	<i>Sample testing</i> .....	115
7.3.4	<i>3D visualization and test simulation</i> .....	118
7.4	CONCLUSIONS .....	126
<b>CHAPTER 8 CONCLUSIONS .....</b>		<b>128</b>
8.1	OVERVIEW .....	128
8.2	SUMMARY OF CONCLUSIONS .....	128
8.3	IMPLICATIONS .....	130
8.4	RECOMMENDATIONS OF FUTURE RESEARCH.....	130
<b>REFERENCES .....</b>		<b>131</b>
<b>VITA .....</b>		<b>140</b>

## LIST OF FIGURES

Figure 2-1	Illustration of viscoplastic strain evolution and stress-strain relationship.....	7
Figure 4-1	Typical gray images from X-ray scanning with slice thickness of 0.5 mm (sample S15), Images show large wood strands (left) and small ones (right) from panel surface and core layers, respectively .....	22
Figure 4-2	Visualization of voids structure of a typical OSB sample from scanned images (sample S15).....	23
Figure 4-3	Void ratio distribution across panel thickness (Threshold value =100). .....	24
Figure 4-4	Measured void ratio in relation with sample mean density and threshold level..	24
Figure 4-5	Void ratio – mean density correlation along panel thickness at different threshold levels (Sample S09).....	25
Figure 4-6	Density and pixel value correlation (Sample S15) .....	26
Figure 4-7	Contour plots of in-plane pixel value (left) and density (right) variations (sample S15) .....	27
Figure 4-8	Density Distribution .....	30
Figure 4-9	Boundary and Loading condition for the simulation test .....	31
Figure 4-10	Simulated Tensile and Shear Tests.....	33
Figure 4-11	Elastic Modulus vs. Flake Orientation at Various Density Deviation Levels .....	35
Figure 4-12	Poisson’s Ratio vs. Flake Orientation at Various Density Deviation Levels .....	35
Figure 4-13	Shear Modulus vs. Flake Orientation at Various Density Deviation Levels.....	35
Figure 4-14	Elastic modulus vs. density deviation at deferent density deviation levels.....	36
Figure 4-15	Poisson’s ratio vs. density deviation at different density deviation levels .....	37
Figure 4-16	Shear modulus vs. density deviation at different density deviation levels.....	37
Figure 4-17	Stress concentration factors at different density deviation levels.....	40
Figure 4-18	Out-of-Plane Stress (Mean density = 0.7, POA = 0): (a) Uniform density; (b) Deviation = 0.07; (c) Deviation = 0.10; (d) Deviation = 0.15 .....	41
Figure 4-19	Maximum stress differential of out-of-plane stresses at different density deviation levels.....	42
Figure 4-20	Pixel value contour plot (S09).....	46
Figure 4-21	Pixel value contour plot (S15).....	47
Figure 4-22	Density contour plot (S09) .....	48
Figure 4-23	Density contour plot (S15) .....	49
Figure 4-24	E1 contour plot (S09) .....	50
Figure 4-25	E1 contour plot (S15) .....	51
Figure 4-26	E2 contour plot (S09) .....	52
Figure 4-27	E2 contour plot (S15) .....	53

Figure 4-28	Mesh of three-layer OSB simulation model.....	54
Figure 4-29	Boundary and loading condition of three-layer OSB simulation model .....	55
Figure 4-30	Deformed shape (S09).....	56
Figure 4-31	Deformed shape (S15).....	57
Figure 4-32	Overall Elastic modulus from prediction and measurement .....	58
Figure 4-33	Stress distribution under uniaxial tension (S09).....	59
Figure 4-34	Stress distribution under uniaxial tension (S15).....	60
Figure 5-1	Gray image from x-ray scan.....	70
Figure 5-2	Three dimensional internal microstructure of a testing sample is reconstructed from series of x-ray tomography images. The phase configuration can be quantitatively determined with a data matrix that can be imported into finite element model. ....	71
Figure 5-3	Three dimensional FE model .....	72
Figure 5-4	Stresses distribution for the fine-mix sample .....	73
Figure 5-5	Stresses distribution for the fine-plus mix sample .....	74
Figure 5-6	Stresses distribution for coarse-mix sample .....	75
Figure 5-7	Stresses distribution along sample diameters (theoretical solution).....	76
Figure 5-8	Stress concentration comparison.....	77
Figure 5-9	Stress distributions and stress concentration factors for different E ratios.....	78
Figure 6-1	Elastic solution of stresses for IDT test.....	80
Figure 6-2	Geometry model of simulation IDT test.....	81
Figure 6-3	Indirect tensile test pulse loading .....	81
Figure 6-4	Finite element model for dynamic modulus test .....	82
Figure 6-5	Dynamic modulus test sinusoidal loading.....	82
Figure 6-6	Two layer viscoplastic model.....	83
Figure 6-7	Stress distributions for elastic and viscoplastic solutions.....	84
Figure 6-8	Displacement for elastic and viscoplastic solutions .....	85
Figure 6-9	Illustration of setting ups for indirect tensile test and dynamic modulus test .....	85
Figure 6-10	Illustration of the process of parameter adjustment .....	87
Figure 6-11	Sensitivity of parameter m on the deformation profile in IDT simulation with haversine pulse loading .....	88
Figure 6-12	Sensitivity of parameter A on the deformation profile in IDT simulation with haversine pulse loading .....	88
Figure 6-13	Sensitivity of parameter E on the deformation profile in IDT simulation with haversine pulse loading .....	89
Figure 6-14	Sensitivity of parameter f on the deformation profile in IDT simulation with haversine pulse loading.....	89

Figure 6-15	Sensitivity of parameter $\sigma_{yp}$ on the deformation profile in IDT simulation with haversine pulse loading .....	90
Figure 6-16	Sensitivity of parameter n on the deformation profile in IDT simulation with haversine pulse loading .....	90
Figure 6-17	Parameter sensitivity to deformation profile .....	91
Figure 6-18	Sensitivity of parameter f on the deformation profile in dynamic modulus test simulation with haversine pulse loading .....	92
Figure 6-19	Sensitivity of parameter n on the deformation profile in dynamic modulus test simulation with haversine pulse loading .....	93
Figure 6-20	Sensitivity of parameter A on the deformation profile in dynamic modulus test simulation with haversine pulse loading .....	93
Figure 6-21	Sensitivity of parameter m on the deformation profile in dynamic modulus test simulation with haversine pulse loading .....	94
Figure 6-22	Parameter sensitivity to deformation profile in dynamic modulus simulation, the deformation is for permanent value after 10 cycles .....	94
Figure 6-23	Simulation and experimental result at 5°C for macroscopic dynamic modulus testing, an actual test with 1Hz frequency was used .....	96
Figure 6-24	Simulation and experimental result at 40°C for macroscopic dynamic modulus testing, an actual test with 1Hz frequency was used. ....	96
Figure 6-25	Steady state deformation profiles for parameter m (-1.0 < f < 0), plot shows both load and deformation profiles than can be used to obtain the dynamic modulus	97
Figure 6-26	Effect of parameter m on the phase angle for numerical dynamic modulus test.	98
Figure 6-27	Effect of parameter A on the phase angle for numerical dynamic modulus test.	99
Figure 6-28	Effect of parameter n on the phase angle for numerical dynamic modulus test	100
Figure 6-29	Effect of parameter f on the phase angle for numerical dynamic modulus test	101
Figure 6-30	Microscopic finite element model for the indirect tensile test .....	102
Figure 6-31	Microscopic numerical testing of samples from WesTrack mixtures .....	103
Figure 6-32	Displacement profile for mesh size 5mm, 3mm, and 2mm.....	103
Figure 7-1	Testing sample geometry.....	106
Figure 7-2	Mould design.....	108
Figure 7-3	Testing stage of the microscopy system (SKYSCAN, 2006).....	111
Figure 7-4	Samples with different aggregate volume fraction during scanning and before testing, (left) ~50% aggregates and (right) ~5% aggregates .....	113
Figure 7-5	(left) Reconstructed sectional image used for 3-D visualization of the digital sample and (right) processed image generated during microscopic finite element model generation.....	114
Figure 7-6	Aggregate volume fraction and void volume fraction statistical relationship, obtained from small sample 3-D analysis .....	115
Figure 7-7	Typical force-displacement curves for different sample categories .....	116

Figure 7-8	Load-displacement curve for pure binder under uniaxial compression.....	116
Figure 7-9	Stress-strain curve for pure binder under uniaxial compression .....	117
Figure 7-10	Force-displacement curves for samples with aggregates, sample2 (5%), sample3 (25%) and sample4 (50%), under uniaxial compression.....	117
Figure 7-11	3-D visualization of small samples with different aggregate volume fractions: (left to right) 50%, 25% and 5%.....	118
Figure 7-12	Finite element model for small samples, one quarter of the digital sample is taken out to show the internal microstructure.....	119
Figure 7-13	Finite element simulation model for the uniaxial compressive test of small asphalt samples, (upper) displacement before loading, (lower) displacement after loading.....	120
Figure 7-14	Finite element model for the pure binder sample simulation .....	121
Figure 7-15	Simulation of pure binder samples with initial parameters from the sample test for the viscoplastic network of the model .....	121
Figure 7-16	Force-displacement relationships from pure binder simulation and test, the back calculated parameters were used in the simulation .....	123
Figure 7-17	Force-displacement relationship from simulation .....	123
Figure 7-18	Simulation results with calibrated material parameters comparing with testing results .....	124
Figure 7-19	Stiffness vs. aggregate volume fraction for small samples at the deformation of 0.01mm.....	125
Figure 7-20	Stress distribution along the main axis of sample4a .....	126
Figure 7-21	Displacement magnitude along the main axis of sample4a.....	126

## LIST OF TABLES

Table 4-1	Summary of Basic Sample Information .....	20
Table 4-2	Elemental engineering constants of OSB .....	32
Table 4-3	Predicted material constants (mean density =0.7 g/cm <sup>3</sup> ).....	34
Table 4-4	Predicted In-plane Stress Concentration Factors at Different Density Deviation and Flake Orientation Levels .....	39
Table 4-5	Summary of Basic Sample Information and measured void ratios .....	45
Table 5-1	Stress concentration of the three WesTrack mixtures .....	66
Table 5-2	Stress statistic study for the fine-mix sample .....	67
Table 5-3	Stress statistic study for the fine-plus mix sample .....	68
Table 5-4	Stress statistic study for coarse-mix sample .....	69
Table 6-1	Aggregate gradation for the sample used in the comparison.....	86
Table 6-2	Percentage change of deformation caused by 10% change of parameters .....	92
Table 6-3	Optimized material parameters used simulation .....	95
Table 7-1	Testing sample designation .....	106
Table 7-2	Weight of aggregates and binder for the sample size .....	109
Table 7-3	Weight of aggregates and binder for different volume fractions.....	109
Table 7-4	Sample dimensions.....	110
Table 7-5	Volume fraction (%) of aggregates and voids .....	114
Table 7-6	Material parameters from back calculation .....	122

## NOTATIONS

$C_{ijkl}$ or $\mathbf{C}$	Elasticity tensor
$D_{ijkl}$ or $\mathbf{D}$	Compliance tensor
$E$	Young's modulus
$e_{ij}$ or $\mathbf{e}$	Deviatoric strain tensor
$I_1$	The first stress invariant, $I_1 = \sigma_{ii} = tr(\boldsymbol{\sigma})$
$J_2$	The second deviatoric stress invariant, $J_2 = \frac{1}{2} S_{ij} S_{ij} = \frac{1}{2} tr(\mathbf{S})^2$
$J_3$	The third deviatoric stress invariant, $J_3 = \frac{1}{3} S_{ij} S_{jk} S_{ki} = \frac{1}{3} tr(\mathbf{S})^3$
$p$	Hydrostatic pressure, $p = -\frac{1}{3} \sigma_{ij} \delta_{ij}$
$\nu$	Poisson's ratio
$S_{ij}$ or $\mathbf{S}$	Deviatoric stress tensor
$\gamma_{ij}$ or $\boldsymbol{\gamma}$	Shear strain tensor
$\varepsilon_{ij}$ or $\boldsymbol{\varepsilon}$	Strain tensor
$\bar{\varepsilon}^{vp}$	Effective viscoplastic strain, $\bar{\varepsilon}^{vp} = \sqrt{\varepsilon_{ij}^{vp} \varepsilon_{ij}^{vp}}$
$\bar{\varepsilon}_m^{pl}$	Equivalent plastic strain in matrix, $\bar{\varepsilon}_m^{pl} = \sqrt{\frac{2}{3} \varepsilon_{ij}^{pl} \varepsilon_{ij}^{pl}}$
$\sigma_{ij}$ or $\boldsymbol{\sigma}$	Stress tensor
$\sigma_e$	Effective Mises stress, $\sigma_e = \sqrt{\frac{3}{2} S_{ij} S_{ij}} = \sqrt{3J_2}$
$\tau_{ij}$ or $\boldsymbol{\tau}$	Shear stress tensor

# Chapter 1 Introduction

## 1.1 Background

Composite infrastructure materials, such as cement concrete, asphalt concrete and wood panels play important roles in the engineering field for commercial and residential buildings and roadways. They are usually inexpensive but always used in large quantities. Any improvement in the mix or fabrication design will significantly affect the service life and hence the maintenance cost. Although these composite materials are composed of different constituents, they have similar material structures, i.e. stiff particles or fibers bonded by matrix media with certain void content. They perform differently due to the properties of different constituents. However, they share some similar behaviors due to similar configuration. Study of one material may lead to a better understanding of another, especially when they are computationally simulated. Furthermore, modeling procedures can be unified to save equipment costs. Although our research emphasis is characterization of asphalt concrete, we will demonstrate its particular application on wood panels as well. On the other hand, the application will help to verify the methodology we used in the study.

Many of paved highways are constructed with asphalt concrete. Although it has been used for decades, improvement in design and construction is still a demand. Material characterization test is a premise of proper design and construction. For material tests, normally the equipment and procedures have been developed and used as standard. However, asphalt concrete shows viscous behavior that is sensitive to loading rate and temperature. Its test involves boundary conditions that vary in time and temperature and becomes complicated. The simulation of real condition becomes relatively time consuming. So it is necessary to develop an alternative test method that utilizes available resources and technologies.

Asphalt concrete consists of three phases, i.e. aggregates, asphalt binder, and air voids. Mix design is the process of determining types of aggregate and binder to use and the optimum combination of these three ingredients. The laboratory procedure uses several critical tests to characterize each trial blend. These characterization tests, although are not comprehensive, will predict how a particular mix will perform in the field during construction and under subsequent traffic loading. The Simple Performance Test (SPT) is defined as a test method that accurately and reliably measures a mixture's response characteristics or parameters that is highly correlated to the occurrence of pavement distress (e.g., cracking and rutting) over a diverse range of traffic and climatic conditions. Based on the definition, it is not necessary for SPT to predict the entire distress or performance history of the Hot Mix Asphalt (HMA) mixture, but the test

results must allow a determination of a mixture's ability to resist fracture and permanent deformation under defined conditions. Among pavement distresses, rutting, fatigue cracking and thermal cracking are major concerns.

Indirect tensile test and dynamic modulus test have been widely used in the evaluation of the performance of asphalt concrete. Dynamic modulus test is used to determine the characteristics and parameters for permanent deformation which related to the rutting performance of the pavement while the indirect tensile (IDT) test mainly for fatigue properties. However, it is difficult to understand the fundamental mechanisms through individual test. Better understanding can be obtained through formulation of models which are clearly defined and capture material responses and interactions between major constituents. Many models, mainly based on continuum media, have been developed to simulate the performance of asphalt mixes. However, due to the complex interaction of the three major constituents, models intended to include the response of all kinds of mixes always become complicated and tremendous efforts are needed for model calibration. In reality, mechanical models for aggregates or asphalt alone are relatively simple and well developed. So, if we can establish a numerical test procedure that associates material property, phase configuration and performance, we will get better understanding of the fundamentals affecting mixture performance. This will also lead to rational design instead of a trial and error process.

Different mixtures with same material properties for each component will produce different performance due to different configurations of phases. The mixture should be considered as heterogeneous under loading. Material models based on homogeneity need to reflect the heterogeneous behavior will lead to complexity in model formulation and calibration. This also leads to difficulties in understanding the interaction between aggregates and asphalt binder. However, asphalt binder itself can be modeled as homogeneous material with adequate accuracy for typical loading encountered in service.

## **1.2 Research objectives**

The overall objective of this research is to build the digital test model in the manner of establishing a realistic material model for each of the constituents and to simulate the behavior of the composite in the sense of understanding the interactions among these constituents. The major advantage of this method lies in that there is a well defined model for each constituent that avoids the parameters for random anisotropy, which is difficult to calibrate. More generally, the complicated test can be conducted numerically in which parameters can be obtained by running simple physical tests. Further advance in computing capacity and data networking will make the calibration of material models more accurate. Nevertheless, the approach is not limited in this area and can be extended to the cases where the actual testing is difficult to setup, such as high speed impact and coupled mechanism tests.

X-ray computerized tomography (CT) was introduced into civil engineering area to obtain material internal microstructure and detect fault. Recent development in image analysis has made it possible to deal with three-dimensional (3-D) microstructural characterization and individual material modeling separately. Combined with numerical methods, they can be used to conduct digital test as an alternative of laboratory and field tests.

Therefore, the first specific objective was to quantify the void distribution and volume fraction of components in the composite as influenced by raw material type and matrix structures. The second objective is to simulate the effect of in-plane density variation on engineering constants of wood panel and stress distributions for panels at various densities and flake alignment levels. The third objective is to build a model which reflects sample internal structure to calculate anisotropic engineering constants of oriented strand-board (OSB). This is the first attempt to optimize the OSB design based on density characterization using x-ray tomography imaging and finite element (FE) simulation. We then apply the same method to the identification of the stress nonuniformity induced by material heterogeneity for asphalt concrete. Furthermore, we use the model along with viscoplastic material model to conduct parameter sensitivity study that forms the basis of back calculation of model parameters. The sensitivity of mesh size is also studied. During the process, we determine the effect of image resolution and element type on the simulation results. Finally, we follow this method to simulated uniaxial compression test on small samples and conduct back calculation of material parameters. This will be used to verify the algorithms we developed in the study. The digital testing results can be used to conduct material characterization of mixtures with different levels of aggregate content.

This research focuses on establishing the numerical experiment model and procedure. It includes x-ray tomography imaging, microstructure reconstruction, phase quantification, finite element model generation, material model development and calibration, and digital experiments. The experiments are limited to Indirect Tensile (IDT) test and Dynamic Modulus (DM) test configuration for material parameter sensitivity study and to uniaxial compression test on a limited number of small samples for procedure verification. All the work is concentrated on the development of a solution for the problem raised above following the defined approaches.

## Chapter 2      Literature Review

Development of x-ray tomography imaging and its application in civil engineering area lead to many research efforts in material characterization and subsequent microstructure based modeling.

### 2.1    X-ray tomography imaging

X-ray is photons with high energy. It can penetrate through objects. X-ray beams, usually shaped as a horizontal planar fan or cone, slice through the object which rotates and moves vertically. Due to the different absorptions caused by density variation through the section, the intensities of X-rays pass through the object will indicate the structural variation which is captured and converted into measurable signals. Image intensifier converts x-ray energy into light, which is then captured by video camera and turns into image pixels. Many slices are then combined by mathematical operations to create CT image. So, the CT system allows the visualization and digitalization of internal structure without breaking the object.

X-ray tomography imaging can distinguish the different phases in a material in a non-destructive manner and has been widely applied to medical science since the 1970s. In the last decade, it has been introduced into engineering field to conduct microstructural measurement and characterization, or to identify flaws such as cracks. In recent years, x-ray tomography image analysis has also been applied to the microstructural characterization of wood and wood products (Funt and C., 1987; Chang *et al.*, 1989; Sugimori and Lam, 1999), asphalt concrete (Braz *et al.*, 1999; Shashidhar, 1999; Wang *et al.*, 2001; Wang *et al.*, 2002), cement concrete (Landis and Denis, 1999; Hall *et al.*, 2000), soil (Desruses *et al.*, 1996; Rogasik *et al.*, 1999; Shi *et al.*, 1999), and rock (Radaelli *et al.*, 1998). Among them, Sugimori and Lam (1999) successfully measured the size and position of the macro-voids using medical x-ray CT scanning techniques. A database from a series of cross-sectional density distributions in a long specimen was developed. X-ray Tomography is also a valid tool for damage characterization, voids quantification and density variation mapping of engineering materials (Wang *et al.*, 2001; Masad *et al.*, 2002; Wang *et al.*, 2004; Zhang *et al.*, 2005a). Some preliminary work by the author will be introduced in following chapters.

### 2.2    Material Constitutive Models

Constitutive equations describe the stress-strain relationship of a material during loading and unloading. Engineering material responds macroscopically to an applied stress either in elasticity or plasticity. In elastic region strain is recoverable. It is

proportional to stress in linear elasticity, which is characterized by Young's modulus. In plastic region strain usually relates to stress in a nonlinear form due to work hardening. The plastic strain is not recoverable. Creep is usually a plastic type deformation at the stress below the yield stress and usually at a relatively high temperature, which is usually greater than one third of the melting temperature of the material. Material can be characterized as viscoelasticity for this condition. For real material, the plastic strain evolution is dependent on loading rates and can be characterized by viscoplasticity.

For time dependent material under loading, strain creep usually includes three phases according to stress (or strain) level, i.e.

- Primary creep, during which unloading will lead to elastic and viscoelastic strain recovery, is strongly dependent on the history of the material. However primary creep strain is usually minimal, i.e. less than one percent of the total strain range.
- Steady state creep, during which unloading will lead to elastic and viscoelastic strain recovery, as well as unrecoverable viscoplastic strain, and
- Tertiary creep, during which the material is unstable and failure will take place within a short range (Desai, 2001).

Most of the creep time is in the steady state region, which dominates the effects of creep. The tertiary creep is usually a short-period fracture failure of a material and should be avoided. It should be pointed out that the elastic, primary creep and tertiary creep regions are very minimal in the total strain range. The whole phenomenon can be described with material models, such as elastic, viscoelastic, viscoplastic through strain decomposition or stress overlay assumptions.

Asphalt Concrete (AC) shows rate and temperature dependent characteristics, which are caused by the viscous properties of asphalt binder (bitumen) and the interaction among the three constituents. For commonly used bitumen, the softening point is around 45 to 60 °C and the melting point is around 150 °C (Dolinsek *et al.*, 2000). So the creep of the asphalt concrete needs to be considered. Constitutive models allowing elastic, plastic and viscous or creep deformation have been attempted to account for certain aspects of material responses.

Triaxial compression tests of asphalt concrete showed that the deviatoric response can be treated as combination of elastic, plastic, viscoelastic and viscoplastic contributions which are slightly dependent on the hydrostatic stress and are linear functions of stresses. It was found that there is no apparent yield limit. The viscoelastic and viscoplastic deviatoric strains can be described by simple power law. It was also found that the volumetric strain is independent of the cycle duration or load repetitions and the hydrostatic response can be assumed as purely elastic. The presence of voids affects the behavior of the mixture (Kim *et al.*, 1997).

In order to sufficiently describe the response of asphalt concrete, it is necessary to choose efficient material models and a proper association mechanism.

### **2.2.1 Viscoelastic material models**

Viscoelastic material exhibits the characteristics of a viscous liquid and an elastomeric solid. It experiences hysteretic stress-strain response, stress relaxation, and strain creep.

If the stress (or strain) level is small, the constitutive relationship can be described by linear viscoelastic theory in form of a Volterra equation, which is separable in both

creep and load responses. Three dimensional linear viscoelastic model is provided in commercial Finite Element package (e.g. ABAQUS, 1995). It was established under the assumption of volumetric and deviatoric decoupling of stresses and strains. The reduced time is used in the equation to account for temperature effects through time-temperature superposition. Relaxation functions for shear and bulk modulus are expressed in Prony series based on experimental data. The model can well describe material response at small stress level.

If nonlinear response dominates the strain range before yielding, or if the material property changes, nonlinear viscoelastic theory is necessary in order to get accurate analysis results. Based on thermodynamic theory, parameters reflecting strain or stress dependent properties were added in the linear-viscoelastic-type equation to account for higher order strain or stress effects on Helmholtz or Gibb's free energy (Schapery, 1969). The model gets good results at various stress levels for both creep and relaxation tests under uniaxial and multiaxial loadings. Similarly, effects of damage were successfully considered with damage variables in the constitutive equation (Dai and Sadd, 2004) that are functions of applied stress or strain (Simo, 1987; Sadd *et al.*, 2004). A piecewise linear Prony series was used to account for nonlinearity in a microstructural model (Abbas *et al.*, 2004). It was indicated that at moderate strain levels there is little difference between the linear and the nonlinear mastic models. However at higher strain (> 0.01%), the difference between the linear and the nonlinear formulations becomes significant.

For asphalt concrete, which has a very low yielding stress (Kim *et al.*, 1997), it is sufficient to use a linear viscoelastic model. At higher stress level, strain hardening plastic or viscoplastic model can be used instead of nonlinear viscoelastic model so that complex correction due to damage could be avoided.

## 2.2.2 Viscoplastic material models

### 2.2.2.1 Viscoplastic formulations

The Perzyna (1966b) viscoplastic formulation defines the viscoplastic strain rate tensor as equation (2-1).

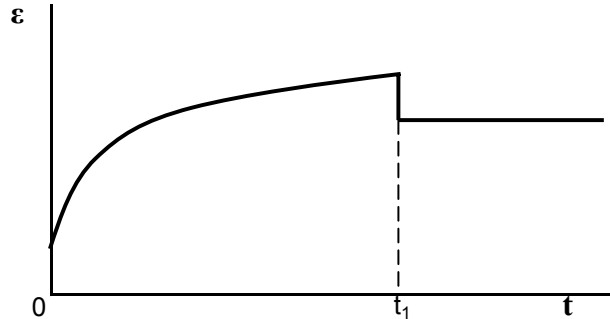
$$\dot{\boldsymbol{\epsilon}}^{vp} = \Gamma \langle \phi(F) \rangle \frac{\partial Q}{\partial \boldsymbol{\sigma}} \quad (2-1)$$

where  $\Gamma$  is the material parameter reflecting fluidity,  $F$  is the yield function, and  $Q$  is the plastic potential. The operator  $\langle X \rangle = (X + |X|)/2$  and  $|X|$  is the absolute value of  $X$ . The function of the yield function,  $\phi$ , can be in a power law or exponential form. The disadvantage of this model is that its implementation in numerical simulation is difficult because of the lack of consistent conditions. Figure 2-1 illustrates the stress and strain responses of the model.

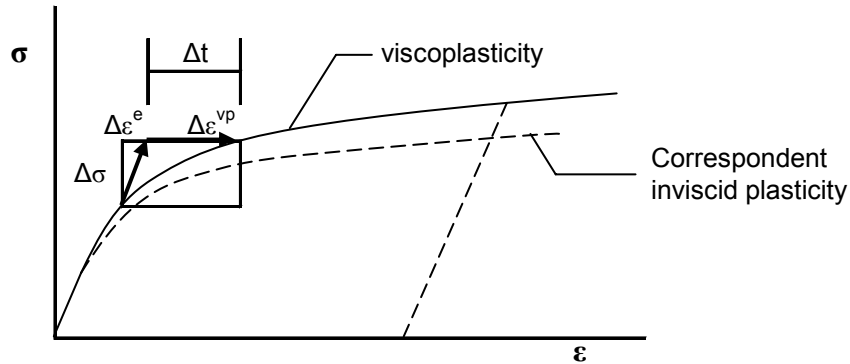
In contrast to the Perzyna model, the Duvaut-Lions formulation (Duvaut and Lions, 1972) uses over-stress as in equation (2-2).

$$\dot{\boldsymbol{\epsilon}}^{vp} = \frac{1}{\tau} \mathbf{C}^{-1} (\boldsymbol{\sigma} - \bar{\boldsymbol{\sigma}}) \quad \dot{\kappa} = \frac{1}{\tau} (\kappa - \bar{\kappa}) \quad (2-2)$$

where  $\tau$  is the relaxation time,  $\mathbf{C}$  is the linear elasticity tensor, and  $\bar{\sigma}$ ,  $\bar{\kappa}$  are the backbone stress tensor and the internal state variable of the corresponding rate independent plastic model, respectively. The advantage of this model is that it can be used with non-smooth yield surface.



(a) Strain-time curve for a constant stress (0 to  $t_1$ ) followed by a rest period ( $t > t_1$ )



(b) stress-strain curve for viscoplasticity and correspondent inviscid counterpart

Figure 2-1 Illustration of viscoplastic strain evolution and stress-strain relationship

Stability study shows that the Perzyna formulation performs better than the Duvaut-Lions formulation in suppressing localization when the relaxation time is small (Etse and Willam, 1999). Three failure mechanisms, diffuse, localize and discrete were analyzed on a triaxial extended Leon model using non-associated plastic flow rule with isotropic hardening in the pre-peak region and isotropic softening in the post-peak region. For both formulations, the inelastic strains are smaller than that of the underlying inviscid material. However, the Perzyna formulation may become unstable when viscosity value is very small. Another study of the Duvaut-Lions viscoplastic extension of an elastoplastic concrete model (Kang and Willam, 1999; 2000) also indicated that the viscoplastic model suppresses the onset of localization of the elastoplastic model and improves mesh-sensitivity. The results showed rate dependent of strength and ductility. The dynamic

strength enhancement in tension due to strain rate increase is significantly higher than that in compression.

Besides the overstress formulations, consistency model (Wang *et al.*, 1997) uses rate-dependent yield surface to account for the viscosity and the Kuhn-Tucker conditions are satisfied, i.e. equations (2-3) and (2-4).

$$\dot{\boldsymbol{\varepsilon}}^{vp} = \dot{\lambda} \frac{\partial F}{\partial \boldsymbol{\sigma}} \quad (2-3)$$

$$F = F(\boldsymbol{\sigma}, \boldsymbol{\kappa}, \dot{\boldsymbol{\kappa}}) = 0, \quad \text{and} \quad \dot{F} = 0 \quad (2-4)$$

where  $\boldsymbol{\kappa}$  is the internal state variable and  $\lambda$  is the plastic multiplier, which can be determined with consistency conditions. The model takes into account of the effect of strain hardening (or softening) rate ( $\dot{\boldsymbol{\kappa}}$ ).

Although direct integration of constitutive equations may give solution to viscoplastic problems on specific boundary conditions, in most cases, numerical solution should be used through iteration process. The implicit method (e.g. Wang *et al.*, 1997) involves local iterations therefore is more expensive in computation, especially for simulations with several thousand loading repetitions. The explicit method is relatively easy to implement, but the time step size should be limited to ensure the accuracy of the explicit integration (Zienkiewicz and Corneau, 1974). It usually should be very small to receive the stability of the system as well as the accuracy of the result (Hughes and Taylor, 1978). For rate dependent solids, Peirce *et al.* (1984) developed a one-step forward gradient time integration scheme, which leads to a rate dependent tangent modulus method. An near-exact explicit algorithm for elastic-viscoplasticity can give solutions with large total time increment (Nemat-Nasser and Chung, 1992).

#### 2.2.2.2 Yield, hardening, and damage

The widely used yielding functions civil engineering materials include von Mises yield criterion and Drucker-Prager yield criterion. The von Mises yield function is usually used for metals and the Drucker-Prager yield function for bonded granular materials. Studies showed that the Drucker-Prager yield function is suitable for modeling AC material (e.g. Seibi *et al.*, 2001; Oeser and Moller, 2004a). In these yield functions, microstructural evolutions, such as density and void ratio change, are not considered. For AC mixture, the energy dissipation mainly lies in aggregate rotation, inter-particle sliding and debonding which leads to continuous change of yielding function. Microstructural parameters can be included in the yielding function to account for microstructural evolution (Gurson, 1977; Tvergaard, 1981; Ju and Tseng, 1996; Guler *et al.*, 2002; Tseng, 2004; Panoskaltis and Panneerselvam, 2005; Tashman *et al.*, 2005a). However, these methods only considered macroscopic evolution of the fraction or orientation of the inclusions. Many of them are based on 2-D microstructural analysis. Therefore, the calibration of the parameters in 3-D condition will be complicated.

The hardening laws can be categorized into isotropic hardening, kinematic hardening and the combination of both. The former describes the growth of the yielding surface, which can be defined as a function of accumulative plastic work or plastic strain in power law or exponential format. The exponential format is appropriate for cases

where hydrostatic loading is significant (Desai *et al.*, 1986). The kinematic hardening defines the motion of the center of the yielding surface as a linear or nonlinear function of plastic strain. Complicated hardening law is needed to describe the full range behavior of a material under cyclic loading, especially with anisotropic characterizations (Faruque and Desai, 1985). This will lead to complexity in parameter calibration and model implementation. In this research, individual component will be modeled as isotropic material and relatively simple hardening law will be suitable.

The evolution of damage is usually considered using effective stress tensor (from damage effect tensor), continuity function, or damage parameter (e.g. Schapery, 1999; Chow *et al.*, 2001; Collop *et al.*, 2003; Gibson *et al.*, 2003; Chehab and Kim, 2005; Panoskaltzis and Panneerselvam, 2005; Uzan, 2005). For asphalt concrete at high temperature, healing can be considered in simulations (e.g. Lee and Kim, 1998b; Kim *et al.*, 2003; Oeser and Moller, 2004a). In this study, the damage and healing effects will be considered minimal and will be a future extension of current work.

### 2.2.3 Strain decomposition models (strain additivity)

Sides *et al.* (1985) developed a viscoelastoplastic constitutive model for sand asphalt mixture under cyclic loading. The total strain is composed of elastic, viscoelastic, plastic, and viscoplastic strain components (also see Perl *et al.*, 1983) and equation (2-5).

$$\varepsilon = \varepsilon_e(\sigma) + \varepsilon_p(\sigma, N) + \varepsilon_{ve}(\sigma, t) + \varepsilon_{vp}(\sigma, t_n, N) \quad (2-5)$$

where  $t$  is loading time and  $N$  is loading repetitions. Each strain component is formulated for different stress levels with different sets of regression parameters. Generally, the inelastic strains are expressed in a form of power function of stress that is modified according to loading duration and repetitions. The model is based on comprehensive tests and describes entire response of the material under loading. Parameters were determined with a series of repeated uniaxial creep and recovery experiments at a constant temperature. The model can reflect the rest and healing behavior of asphalt concrete at each loading stage. However, the calibration involves determination of many regression coefficients hence is very complicated. It was found that the plastic strain component usually is very small and hardly distinguishable from viscoplastic part.

Besides elastic, viscoelastic (Kelvin body) and viscoplastic (Newton body) strain components, tertiary strain component was used to describe damage and healing responses (Oeser and Moller, 2004b). It was assumed that the elastic strains are dependent on the total stresses and the inelastic strains are dependent only on deviatoric stresses. The model reflects cyclic loading sequences composed of positive and negative (healing) loading phases. The von Mises type creep surface was used for the tension zone and the Drucker-Prager type function in the compression zone with isotropic and kinematic hardening. Non-measurable parameters were optimized by comparing the simulation results with the experimental ones with a modified evolution strategy, which combines classical evolution strategy with Monte Carlo simulation and gradient methods. This shows a feasible method for the estimation of model parameters.

Seibi *et al.* (2001) used a Perzyna (1963) viscoplastic model for asphalt concrete in a loading-rest period test with high loading rates. The Drucker-Prager yield criterion with isotropic work hardening was used. For one dimensional state, the material constants

and plastic deformation function were obtained from stress-plastic strain curve and yield stress-plastic strain rate curve constructed from uniaxial compression tests. However, for multiaxial cases, it is difficult to obtain the material constants and functions from the tests. In their study, the model parameters were optimized with CONMIN provide by NASA-AMES research center. It was found that the binder and mixture followed a similar strain evolution pattern but with different magnitudes. It was concluded that the asphalt concrete at elevated temperature and high loading rate is controlled by elasto-viscoplastic response, which can be defined using Drucker-Prager yielding surface. According to the sensitivity analysis, the material response was found to be most sensitive to the viscosity coefficients and least affected by the friction angle. It was suggested that the optimization method is suitable for model calibration.

The assumption of time-temperature superposition was found to be valid for both small strain viscoelastic and large strain viscoplastic responses at high temperature (Schwartz *et al.*, 2002). In their study, the microstructural damage was considered based on the viscoplastic extension of Schapery (1999) framework. The viscoplastic strain creep was assumed in a strain-hardening form. Viscoplastic component was calibrated through uniaxial creep and recovery tests.

Collop *et al.* (2003) developed an additive constitutive model composed of viscoelastic and viscoplastic creep component. A power law function was used for the steady-state viscoplastic creep. Viscoplastic damage evolution was considered in the creep function with a damage parameter. It was suggested that the effect of stress dependency on the permanent deformation is important, especially when the stress level is high. It was stated that the elastic and viscoelastic material properties are of less significance compared to the viscoplastic material properties for the evaluation of permanent deformation.

A model with viscoelastic and viscoplastic strain decomposition was used to characterize asphalt concrete (Uzan, 2005). The undamaged viscoelastic component was solved using correspondence principle. The damage was considered in both components with the effective stress evaluated in different form. An exponential continuity equation, which is a function of an internal state variable, was used in viscoelastic component and a damage parameter was used in the viscoplastic component. The characterization of material parameters for each component was separated using different tests, i.e. the frequency sweep test for viscoelastic component, repeated load test for viscoplastic part, and fracture test for damage parameters. It was shown that the viscoelastic component dominates the post-peak deformation and the viscoplastic component increases at a decreased rate.

#### 2.2.4 Multi-layer models (stress overlay)

The model generally assumes that the material is composed of two or more components with different mechanisms acting in parallel with certain contribution ratios. We assume that the strains in all components are the same and the stresses are additive, i.e.  $\boldsymbol{\varepsilon} = \boldsymbol{\varepsilon}_1 = \dots = \boldsymbol{\varepsilon}_n$  and  $\boldsymbol{\sigma} = \boldsymbol{\sigma}_1 t_1 + \dots + \boldsymbol{\sigma}_n t_n$ .

Kichenin *et al.* (1996) proposed a two-mechanism parallel model to simulate the viscous and plastic responses of a polymer. The model associates a simple Maxwell

viscoelastic component that represents creep and relaxation, with an elastoplastic component that accounts for residual stress and strain as in equations (2-6) to (2-8).

$$\sigma = \sigma_{ve} + \sigma_{ep} \quad (2-6)$$

$$\begin{aligned} \sigma_{ve} &= \eta \dot{\epsilon}_{ve} \\ &= E_{ve} (\epsilon - \epsilon_{ve}) \end{aligned} \quad (2-7)$$

$$\begin{aligned} \sigma_{ep} &= E_{ep} \epsilon && \text{for } \sigma_{ep} < \sigma_p^c \\ \sigma_{ep} &= E_{ep} (\epsilon_c + g(\epsilon - \epsilon_c)) && \text{for } \sigma_{ep} \geq \sigma_p^c \end{aligned} \quad (2-8)$$

where the model parameters  $(E_{ve}, \eta, E_{ep}, \sigma_p^c, \alpha)$  were obtained through series of uniaxial tests by constructing strain- and stress-time curves, such as traction-stress relaxation-strain recovery sequences. The model quantified both plastic and viscous response of material with memory effects. It can identify residual strain for relaxation and residual stress for recovery. It shows transfer of stress between two mechanisms, i.e. the domination of viscous mechanism decays with relaxation while response of plasticity increases gradually. However, the model disregarded thermal effects. The yield limit plays an important role for the description of early stage response. A three-dimensional cyclic experiment was conducted and the results were consistent with literature.

A generalized overlay model (2-9) based on Disturbed State Concept can account for elastic, viscoelastic, viscoplastic, and viscoelasticviscoplastic material response (Desai, 2001). The response of each component can be achieved by assigning proper material parameters (including 0 and  $\infty$ ) to each component, which is an elastoviscoplastic reference unit (Perzyna formulation).

$$\begin{aligned} d\sigma &= d\sigma_i t_i \\ d\sigma_i &= C_i d\epsilon \end{aligned} \quad (2-9)$$

where  $t_i$  is the contribution ratio for  $i$ -th component.

The disturbance or damage resulting from viscous creep was expressed in terms of the sum of accumulative creep strain or strain work from recoverable and irrecoverable parts. The material parameters, which have physical meanings, can be obtained from strain- and stress-time curves. The number of parameters in this model is less than that in strain decomposition models. It was suggested that the overlay model is relatively easier for implement and extension.

### 2.2.5 Microstructural considerations

Gurson (1977) proposed a porous material model considering the effects of voids evolution. The model assumes plastically incompressible matrix with randomly distributed air voids. Therefore the composite material is pressure dependent due to the voids growth and contraction. Tvergaard (1981) modified void fraction and hydrostatic stress with modification factors based on FE simulation results as equation (2-10).

$$F = \left( \frac{\sigma_e}{\sigma_y} \right) + 2q_1 f \cosh \left( -q_2 \frac{3p}{2\sigma_y} \right) - (1 + q_3 f^2) = 0 \quad (2-10)$$

where  $f$  is the void volume fraction,  $q_1$ ,  $q_2$  and  $q_3$  are material parameters. The model is available in ABAQUS and these parameters can be defined in tabular form for different temperatures. Guler et al. (2002) used this model in the simulation of laboratory compaction of cylindrical specimens under uniaxial compaction pressure and cyclic shear strain. It gives reasonable results for void volume fraction smaller than 10%. However, the porous model was developed for metals. For asphalt concrete, interaction between matrix and inclusions and shear dilation are more critical. The calibration of the evolution of voids is therefore difficult. Furthermore, the rate dependent response should be considered for asphalt concrete.

A Network model based on branch vectors for circular or ellipsoidal particles was found to be more computationally efficient than continuum models (Sadd *et al.*, 2002). Rigid aggregates and elastic binder were used in the model. However, the model assumed no inter-particle contact. This makes it less accurate than continuum model for asphalt concrete for which the interactions between aggregates are very important.

Tseng (2004) extended an porous model for elastoplastic material with randomly distributed spherical voids (Ju and Tseng, 1996) to elastoviscoplastic materials with Duvaut-Lion formulation. The consistent tangent modulus for the elastoviscoplastic response was derived from the elastoplastic one with introduction of a relaxation parameter. The model assumes von Mises yield criterion and isotropic hardening. Parameters accounting for phase configuration, i.e. phase volume fraction and interaction between inclusions, were included in the formulation. It was found from statistical studies that the increase of voids fraction caused decrease of the stiffness and higher rate of loadings led to stronger material responses. However, the void volume fraction was assumed to be constant during the deformation. The inclusions were considered as elastic spheres but with uniform size. The tensor reflecting inter-particle interaction effects was derived micromechanically with pair-wise interaction among voids. So the model is not accurate for materials with high level of voids fraction.

Tashman et al. (2005b) developed a microstructural viscoplastic continuum model for asphalt concrete considering the orientation of aggregates and the growth of voids. The viscoplastic strain rate was defined using Perzyna (1966a) formulation with a power law function of linear Drucker-Prager yield criterion. The aggregate anisotropy was accounted for with a microstructure tensor that reflects the orientation of non-spherical particles through a vector magnitude, which ranges from zero to unity. The damage was accounted for with damage parameter, which is expressed as area ratio of voids. They were incorporated into the yield function by modifying stress invariants based on effective stress theory as equation (2-11).

$$F = \sqrt{J_2^e} - \alpha I_1^e - \kappa = 0 \quad (2-11)$$

where the superscript  $e$  denotes effective values. Hence, the direction of the viscoplastic strain rate is dependent on anisotropy and damage. Isotropic hardening was defined in a power law function of effective stresses. The evolution of the damage defined as a function of viscoplastic strain energy rate, confining pressure, and effective viscoplastic

strain. The model parameters were obtained through laboratory triaxial strength test and static creep test. It was found that the material response for stiffness was affected by material anisotropy as well as loading rate. The damage evolution was suppressed by confining pressure. A similar anisotropy consideration was successfully used in a model composed of hyperelastic and Perzyna viscoplastic response with a three stress invariants flow rule (Panoskaltsis and Panneerselvam, 2005). However, the microstructure analysis results were still used for macroscopic simulations in these models.

## 2.3 Parameter estimation

There are many method can be used to conduct the parameter estimation.

### 2.3.1.1 Genetic Algorithm

The genetic method was considered as one of the best method to optimize the material parameters. The concept can be briefly described as:

Gene:  $\Lambda_i = (q_1^i, q_2^i, q_3^i, \dots, q_k^i)$

Fitness function:  $\Pi(\Lambda_i)$

Rank of fitness:  $\Lambda'_i$

Mate nearest pairs:  $\Theta_i = \Phi^i \Lambda'_{i-1} + (1 - \Phi^i) \Lambda'_i$

where  $\Phi^i = A\phi^i$  is random numbers from uniform distribution with A can be set  $=\sqrt{2}$ .

The process can be outline as:

- generate gene with parameter set,
- evaluate fitness function with simulation and test results,
- rank the genes according to the value of fitness function,
- improve the gene set, and
- repeat the processes 1 to 4 until fitness function satisfy preset value.

The method was used in many structural analysis and optimization studies (e.g. Chiroiu *et al.*, 2000; Chakraborty *et al.*, 2002; Chau and Albermani, 2003; Reddy *et al.*, 2004; Aguilar Madeira *et al.*, 2005; Schmidt and Thierauf, 2005). However, the gene size and the number of generations are critical to the accuracy of the estimation. In the case that each simulation takes long time, a method with more guidance in evolution is necessary.

### 2.3.1.2 Sensitivity analysis based method

For one simulation, we can get the deformation,  $D_i$ , at several points, which can be used to calculate the value of the objective function  $\Pi(\Lambda)$ . The parameters then will be changed for certain percentages to obtain a new set of  $D_i$  and new value of the objective function. The selection of parameter is based on the sensitivity analysis. The objective function can be in the form of Equation (2-12)

$$\Pi(\Lambda) = \sum_i^N (D_i - \bar{D}_i)^2 \quad (2-12)$$

where  $\Lambda = \Lambda(E, \nu, r, q_1, q_2, \dots)$  is the tensor of parameters to be optimized.

It is usually difficult to calculate the derivative or object function respect to a parameter that requires optimization. Therefore, non-derivative algorithms are suitable for this study. Since the process is carried out in the order of the sensitivity and there are more results can be used for one simulation, generally this may speed up the process of the estimation (e.g. Guler *et al.*, 2002). This method will most likely be used in the study.

## **Chapter 3      Method and organization**

### **3.1    Approach**

The asphalt mixture is composed of two different materials with significantly different mechanical properties. It is recognized that there is a 20  $\mu\text{m}$  to 50  $\mu\text{m}$  wide interfacial transition zone (ITZ) between aggregates and matrix, which has unique properties (Garboczi and Bentz, 1991; Bentur and Odler, 1996; Scrivener and Pratt, 1996). However, cement-aggregate bond strength has only minor effect on the elastic modulus and compressive strength of concrete (Darwin and Slate, 1970). The strength of concrete is governed by flaws of the order larger than the width of ITZ (Mindess, 1996). In this work, we assume that the strain should be continuous between phases as long as there is no significant damage. The ITZ was not considered and the continuum FE method with phase variation was used to carry out stress-strain analysis.

The strain additive models illustrated in previous chapter showed relative importance of each component. The yielding limit of asphalt material is sufficiently small to use linear viscoelastic theory in the pre-yielding region. The viscoplastic component is dominant in plastic deformation region. However, the stress overlay model has clear physical meaning for parameters and is easy to calibrate. Therefore, a two component stress overlay model was used in this research. Finite element package ABAQUS provides a wide range of material models including a two layer model, which was used in the study to validate the model implementation and calibration procedures.

The first major task in this research is to develop procedures for x-ray tomography imaging and model construction. The second task is to select proper material model for each constituent and to improve it based on physical performance tests. The third task is to estimate material parameters using inverse algorithms and to calibrate the material models with uniaxial test on small samples. Further comparison of digital and physical test is to be conducted to verify the method. Then we can use the method to conduct digital performance test to obtain mixture characteristics and evaluate mixture performances. The research involves both computer simulations and experiments. The outputs are programs or codes written in FORTRAN, IDL, Image-Pro and MATLAB to enable the construction of microstructural model of digital samples for numerical material performance tests.

### **3.2    Organization**

In this research, the test samples were scanned using x-ray tomography to obtain a series of sectional image slices. 3-D microstructure of the sample was digitally

reconstructed by stacking these sectional images. Several computer codes were developed to carry out the quantitative 3-D reconstruction. The 3-D microstructural data was mapped into FE model. FORTRAN programs were developed to automatically generate the simulation model with sample geometry, phase configuration, loading pattern and boundary conditions. Different constituents were assigned with different material properties to account for the effects of the microstructure on stresses and deformations. Alternatively, material properties were varied based on density variations, which is obtained from image analysis. This was used in the material characterization of wood OSB panels. The detailed processes for different studies for wood panel and asphalt concrete are illustrated in Chapter 4 and Chapter 5, respectively.

Chapter 4 demonstrated the characterization of anisotropic properties of wood panels using combined x-ray tomography imaging and FE simulation. Three-layer wood panel samples were prepared and the density distribution through sample thickness was measured with an x-ray based densitometer. Three dimensional visualization of internal structure was carried out by developing computer source codes in IDL. The voids were identified based on the threshold values back calculated from actual void volume fraction. The in- and out-of-plane void distributions were obtained and the distribution pattern was compared with the actual measurement. The FE model was built based on the density variation of the wood panels. The overall material constants were then determined. Modeling the mechanical response of wood panels with such variation of density and flake orientation in plane can obtain the equivalent material properties that are essential in design and construction.

Chapter 5 presented a study of the effect of phase variation on the performance of asphalt mixture. The elements representing aggregates and asphalt binders were assigned with different elastic material properties while the elements representing voids were removed during the loading steps. The results of the simulation were compared with the analytical elastic solution (Hondros, 1959a) to illustrate the stress non-uniformity. The stress concentration factor was obtained as an indicator of mixture performance. It is expected that due to the existence of aggregates and voids in the mixture, the stress distribution will no longer follows that of either the theoretical elastic solution or the FE solution assuming homogeneous material properties for asphalt mixtures. The performance of different mixtures can be classified. The variation of stress concentrations due to different ratios of elastic modulus between aggregates and asphalt binder were also studied.

In chapter 6, a macroscopic parametric study was conducted to obtain the sensitivity of each parameter to the deformation response of the asphalt concrete sample. A two-layer material model was used for the mixture. The model associates linear viscoelasticity with elastoplasticity in a stress overlay form. The sensitivity study was conducted through the form of numerical indirect tensile test and dynamic modulus test. It will serve as a guide for the calibration of the material model so that simulation results can be matched with actual test results. Then, a microscopic model was built considering the viscous behavior of the asphalt binder and the phase configuration of the mixture. The effect of image resolution on the simulation result was conducted. Simulation techniques were also studied to enable large number of repetitions. In the microscopic model, only the binder is considered as viscoplastic material. This will leads to relatively easy and accurate model characterization.

Chapter 7 presented the experimental program, parameter estimation and digital test verification. Eight small samples were prepared for the model calibration and procedure verification. This was done in the asphalt lab at VTTI. All samples were scanned to build the microstructure model following the approach developed in previous chapters. Uniaxial compressive tests were carried out with monotonic loading at small loading magnitude. Deformations and loads were measured and recorded along time. The results contain information that was used for parameter calibration with sensitivity based back calculation. The parameters were adjusted according to their sensitivities studied in previous parametric simulations. Finally, the tests on samples with different aggregate contents were conducted and the simulations of the corresponding tests were carried out with optimized model parameters. The comparison of the actual and virtual tests verifies the method.

The concluding chapter 8 summarized the achievements and key findings. The major result is a procedure of the construction of digital testing samples, characterization of anisotropic material properties of wood panels, identification of the stress non-uniformity as an indicator of performances for different mixtures, and determination of composite performance with different aggregate configurations. Finally, further research to improve the method and its possible extension to other studies were recommended.

## Chapter 4      Characterization of wood composite

### 4.1    Void structure characterization<sup>†</sup>

#### 4.1.1    Introduction

Strand-based composites such as oriented strand-board (OSB) are formed by arranging wood strands in a mat and bonding them together with adhesives under heat and pressure. The reconstitution process disperses natural defects in the wood, resulting in more consistent and uniform mechanical and physical properties of the composites. The performance of these products is governed by the properties of wood strands, adhesive, manufacturing strategy, and production process (Sugimori and Lam, 1999; Barnes, 2000). As a result, significant opportunities exist for refinement and optimization of the mechanical and physical properties of the composites through controlling raw material input and manufacturing process.

The importance of flake mat structure and its influence on panel properties is well known. Suchsland (1962) investigated the density variation in the plane of the panel, known as Horizontal Density Distribution (HDD), and determined that flake geometry will affect the relative void volume in a mat. Suchsland and Xu (1989) continued their investigation to develop a model for simulation of the HDD in flake board. It was concluded that both internal bond and thickness swell properties were directly affected by HDD. Dai and Steiner (1994a; 1994b) developed a probability-based model to describe randomly packed, short-fiber-type wood composites. The model uses the approach that the structural properties of a randomly formed flake network are random variables, essentially characterized by Poisson and exponential distributions and predicts the distribution of number of flake centers per unit of flake area, flake area coverage, free flake length, and void size (area as viewed from above). Lang and Wolcott (1996) developed a Monte Carlo simulation procedure that predicts the number of strands in the centroid of imaginary strand columns, the vertical distance between adjacent strands and the position of the column centroid in relation to strand length based on data from laboratory mats.

In strand-based wood composites, the presence and distribution of macro-voids are generally governed by the random lengths of the wood strands and their partial random deposition during the forming process. For a long time, the OSB industry has been searching for ways to reduce board density. Lower panel density means lower manufacturing costs and more macro-voids in the panel. Although the presence and distribution of macro-voids influence the structural and physical properties of strand-

---

<sup>†</sup> Excerpt reprinted from Zhang, B. et al. (2005a).

based wood composites, their measurement and quantification are difficult. Shaler (1986) used a mercury intrusion method to estimate void content in flake-boards of various densities, resin levels, flake orientations, and species composition. The specimens used were rather small (about 0.25 inch cubes) which may not adequately represent the actual void distribution in the panel. Lenth and Kamke (1996) developed an image analysis procedure for estimating void shape and size during the consolidation process. No attempt was made in using the method to determine internal void content of a fully pressed and resin-cured panel. Ellis et al. (1994) investigated the measurement of macro-void areas using two imaging systems: a video camera and a line scan camera. Such methods are useful, but they are time-consuming; and the internal presence and distribution of macro-voids cannot be obtained without cutting open the specimens.

X-ray is photons with high energy so it can penetrate through objects. In engineering field, it can be used to conduct microstructural measurement and characterization, or to identify flaws such as cracks.

In the last decade, advanced imaging techniques such as the x-ray tomography imaging technique and the magnetic resonance imaging (MRI) technique have been used to study the structure of granular materials. X-ray tomography imaging can distinguish the different phases in a material in a non-destructive manner and has been widely applied to medical science since the 1970s. In recent years, x-ray tomography image analysis has also been applied to the microstructural characterization of wood and wood products (Funt and C., 1987; Chang et al., 1989; Sugimori and Lam, 1999), asphalt concrete (Braz et al., 1999; Shashidhar, 1999; Wang et al., 2001; Wang et al., 2002), cement concrete (Landis and Denis, 1999; Hall et al., 2000), soil (Desruses et al., 1996; Rogasik et al., 1999; Shi et al., 1999), and rock (Verhelst et al., 1995; Radaelli et al., 1998). Among the studies for wood-based composites, Sugimori and Lam (1999) successfully measured the size and position of the macro-voids in Parallam using medical x-ray CT scanning techniques. A database from a series of cross-sectional density distributions in a long specimen was developed.

In this study, x-ray tomography imaging technique was developed and used to characterize internal void structure of strand-based structural wood composites. The specific objective was to quantify the void distribution and volume fraction in the composite as influenced by raw material type and mat structures.

## **4.1.2 Material and method**

### *4.1.2.1 X-ray Tomography System*

The x-ray tomography system used in this research is a Model ACTIS 225 System. The system consists of x-ray source generator, collimator, sample holder and detector array. The system uses up to 225kV x-ray source and has up to 10 micron resolution.

During scanning, cone shaped x-ray beams pass through the sample, which is rotated and moved vertically. Due to the different absorptions caused by density and/or material variation through the sample, the intensities of X-rays passing through the object vary depending on structural difference in the sample. The detector array captures and converts the transmitted x-ray beams into measurable signals. Image intensifier further converts the x-ray energy into light which is then digitalized into numerical data by a

video camera and turns into image with the computer system. By moving the sample vertically, many slices can be taken through the sample thickness and then combined by mathematical operations to create three-dimensional CT images. The system allows the visualization and digitalization of internal structure without breaking the object.

#### 4.1.2.2 Wood Composite Sample Preparation

Three-layer OSB was manufactured using mixed hardwood flakes with various combinations of furnish quality (i.e., large wood flake versus fines). Related panel production information is summarized in Table 4-1. Two replicate OSB samples with nominal size of 76-mm (length) by 76-mm (width) by 12-mm (thickness) were prepared from each panel group. The samples were conditioned for several months at 25C and 65% relative humidity prior to testing. Sample dimension and weight were measured to determine their volume and mean density. Density distribution through sample thickness was measured with an x-ray based densitometer for all samples.

Table 4-1 Summary of Basic Sample Information

Sample ID	Panel Construction <sup>a</sup>	Density <sup>b</sup> (g/cm <sup>3</sup> )
S07	Face: 55%WFL	0.73
S08	Core: 45%WFL	0.70
S09	Face: 55%WFL	0.69
S10	Core: 10%WCM & 35%WFL	0.71
S11	Face: 55%WFL	0.75
S12	Core: 20%WCM & 25%WFL	0.73
S13	Face: 55%WFL	0.64
S14	Core: 30%WCM & 15%WFL	0.62
S15	Face: 55%WFL	0.71
S16	Core: 45%WCM	0.69

<sup>a</sup> WFL – Wood face large (flake); and WCM – Wood core material.

<sup>b</sup> Volume based on 6% moisture content.

#### 4.1.2.3 X-Ray Scanning and Image Analysis

X-ray imaging of the OSB samples was done with 140 kV x-ray source. The system was calibrated according to the material properties and the size of the samples. It includes offset, gain, horizontal wire, vertical wire, and central ray and wedge calibration. This process is very important for obtaining good image in the scanning process. Due to the small density of OSB, lower x-ray source was used in the scanning. Eight slices were scanned in one rotation and the slice increment was about 0.5 mm. The average value of

eight shot at one position was used for following image reconstruction and analysis. For each sample, 24 slices was taken along the thickness direction with each slice representing about 0.5 mm thick of internal structure.

The image set from each sample was used to create three dimensional visualization of its internal structure. The grey images obtained were first processed by removing the border of each slice which is the area between reconstruction area and actual sample area. The reconstruction was carried out using ImagePro, IDL and Voxel program package. The IDL program allows making section or block view from the reconstructed three dimensional images. It also has other options to make the three dimensional visualization more vivid and colorful. Several computer source code based on this software language (IDL) was written to carry out three dimensional reconstructions of the panel and the voids as well as some void quantification.

#### *4.1.2.4 Voids Identification and Quantification*

In the binary image, voids and wood flakes were assigned with different digital values according to the computerized density obtained from scanning process. Voids were identified from the structure by setting a proper threshold in binarized images based on histogram analysis. The total area assigned as voids were then calculated and the voids ratio was quantified using these image tools. The threshold value selection plays a critical role for this process. However, only the boundary pixels of voids are sensitive to the threshold adopted in the quantification. The number of such boundary pixels depended on the size and shape of the voids, i.e. the ratio between total boundary pixel and total voids area influences the accuracy of the voids quantification. This may explain some diversity observed in samples with different core size which generate different size of voids. Many ways can be used to increase the accuracy of the quantification. One is to assign these boundary pixels as voids at a proper ratio.

The voids ratio distribution along the panel thickness was obtained from every slice. By measuring the void ratio for divided areas on each image slice, a voids distribution along the width and length direction can be created. Macros were made to carry out this calculation in image processing software package ImagePro and IDL, which can make contour plot of the pixel value. The total void ratio for a sample then was statistically summarized. Based on the binarized image, the three dimensional void structure of samples was created for visualization and characterization using IDL program. In this process, only voids data of each slice was filtered out and used to create the three dimensional visualization. From these three dimensional images, the general voids ratio magnitude can be visually characterized. The voids ration obtained for the samples are tabulated.

### **4.1.3 Result and discussion**

#### *4.1.3.1 Measured Void Distribution*

Typical gray images from x-ray scanning are shown in Figure 4-1. The images provide visualization of a section cut along the thickness. Voids (in dark color) are randomly distributed across the plane. There was a significant mix of large and small flakes in the images and flake boundaries are clearly seen. Thus, the section cuts and

surface view show internal structure intensively without really cutting the samples. Three-dimensional panel reconstruction was done using color image slices with software package ImagePro and IDL for the given panels. The corresponding three dimensional voids structure constructed based on binary image obtained with a threshold value of 100 is shown in Figure 4-2. The white areas in the individual binary image correspond to actual voids within the panel.

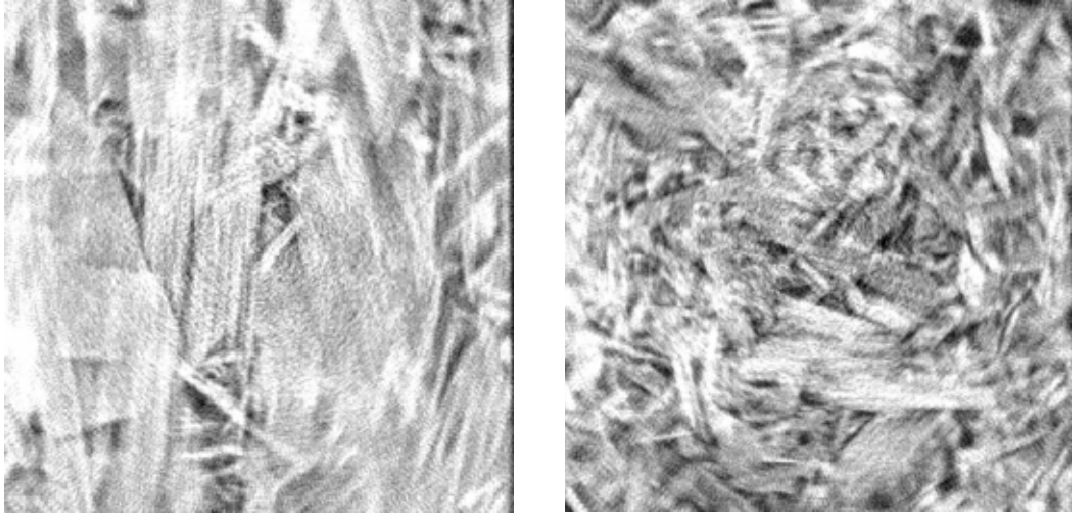


Figure 4-1 Typical gray images from X-ray scanning with slice thickness of 0.5 mm (sample S15), Images show large wood strands (left) and small ones (right) from panel surface and core layers, respectively

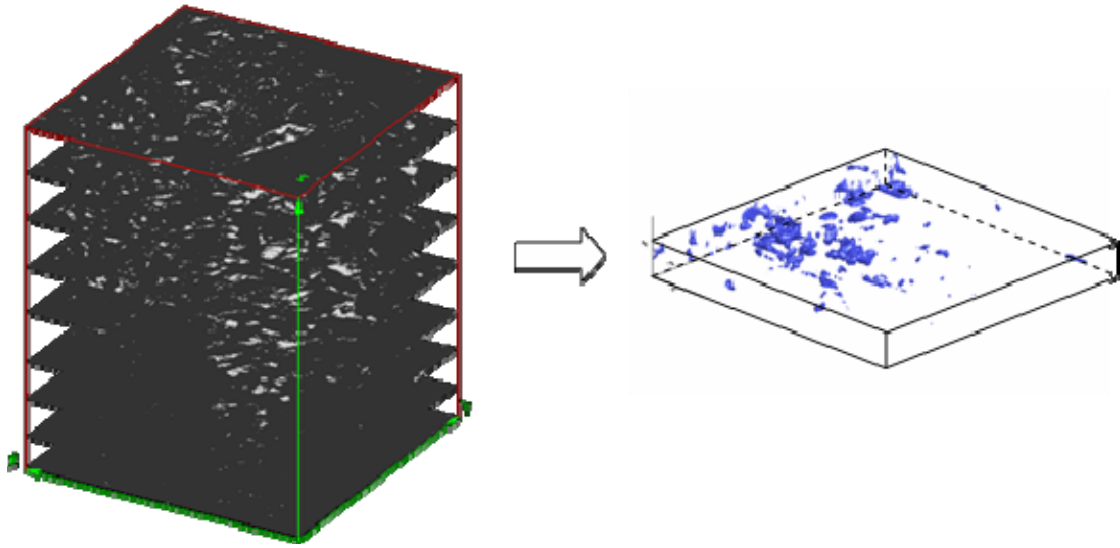


Figure 4-2 Visualization of voids structure of a typical OSB sample from scanned images (sample S15)

The void area and perimeter were measured using ImagePro and IDL for each slice for a given sample. The obtained void ratio distribution along the panel thickness with a threshold value of 100 is shown in Figure 4-3 for the selected samples. It can be seen that measured void ratios varied from sample to sample. The void value was high in the panel center and decreased toward panel surface. This trend agrees well with the through-thickness density variation of OSB. The measured void values decreased with increase in panel mean density (Figure 4-4) in rough linear fashion.

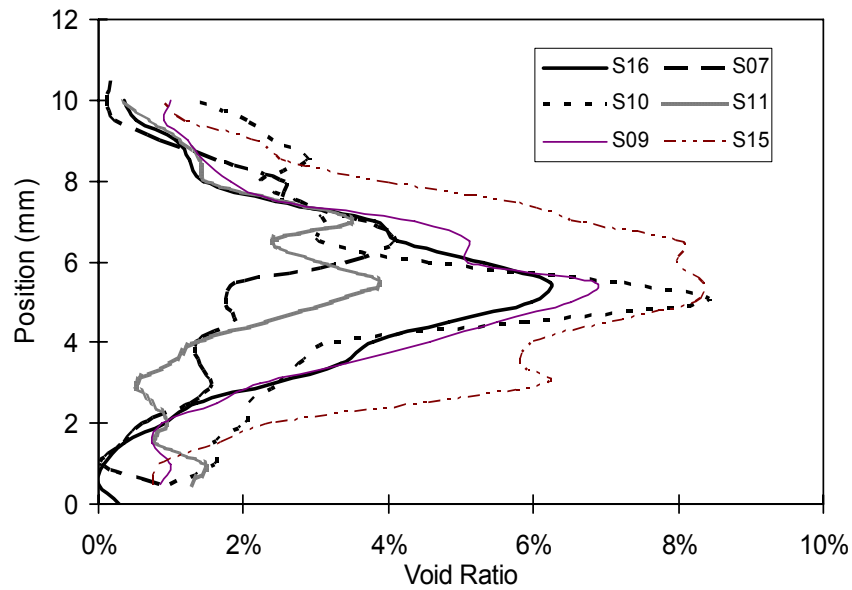


Figure 4-3 Void ratio distribution across panel thickness (Threshold value =100).

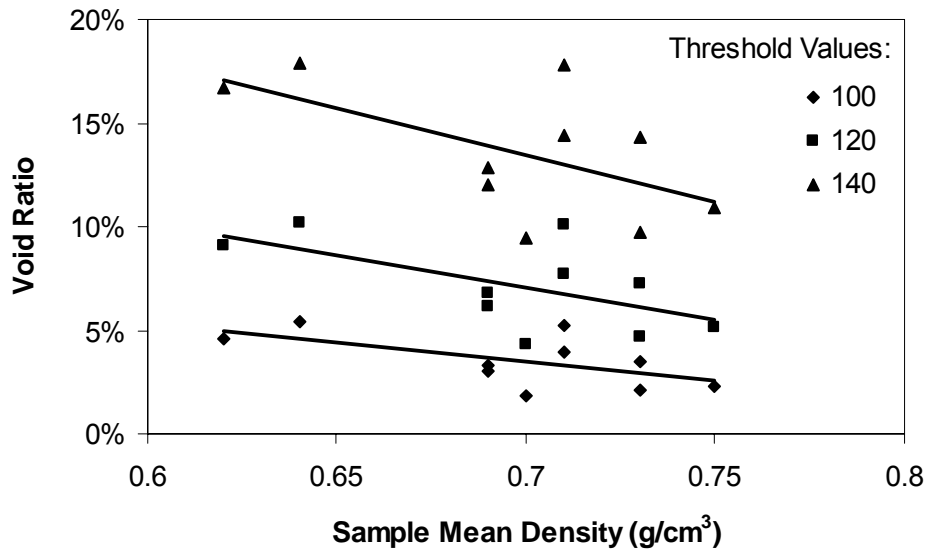


Figure 4-4 Measured void ratio in relation with sample mean density and threshold level.

Figure 4-5 shows the correlation between measured void ratio and layer density across the panel thickness (sample S09). Over a large density range, voids in OSB decreased exponentially with increase in density. At high density levels, compression of wood itself under heat and pressure led to little change in the between-strand voids. At the low density levels, the voids increased rapidly as density was reduced.

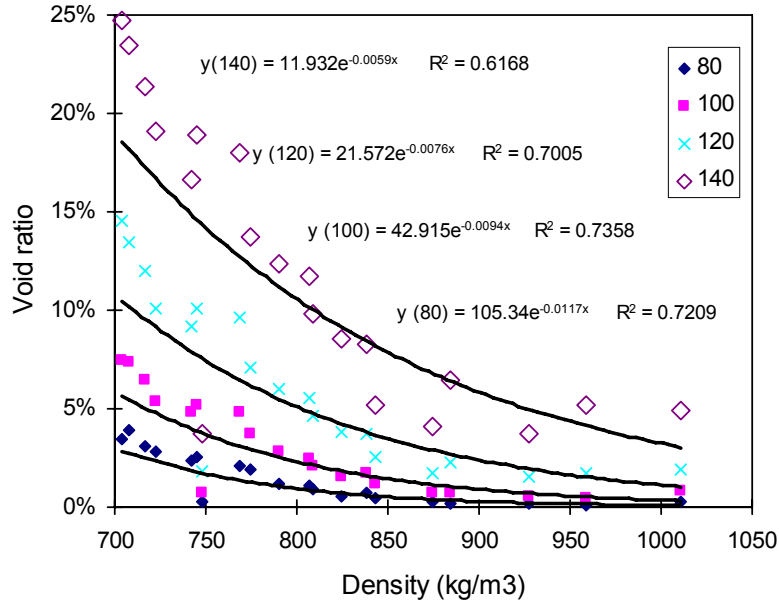


Figure 4-5 Void ratio – mean density correlation along panel thickness at different threshold levels (Sample S09)

#### 4.1.3.2 Effect of Threshold Level

The void ratios obtained from image processing depend on the selection of threshold value used (Figure 4-4 and Figure 4-5). At a given density level, measured void ratios increased with increase of the threshold value. Thus, for randomly distributed voids like these in OSB, defining the void boundary through properly thresholding the images had a large influence on actual void value. For all OSB samples, the general distribution trend of voids was the same.

In order to eliminate the effect of the threshold value selection, the total pixel value, which is related to image density intensity, was related to the measured layer density for each sample. Figure 4-6 shows a typical plot between layer density and total pixel values for sample S15. Sample density is linearly related to the pixel value for all the samples. The relationship can be used to predict density variation based on measured pixel values for a given panel type.

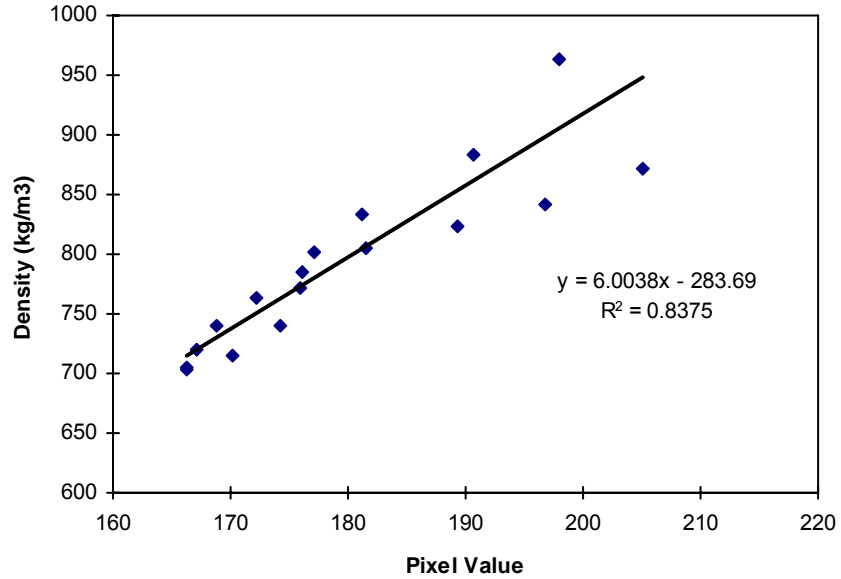


Figure 4-6 Density and pixel value correlation (Sample S15)

#### 4.1.3.3 Predicted In-plane Density Distribution

Figure 4-7 shows contour plots of in-plane pixel value (measured) and density (predicted) distributions (sample S15). The predicted density distribution was obtained using density-pixel value relationship established for the sample. Significant variability in both pixel value and density existed in OSB as shown in Figure 4-7.

The generated density map can be used to relate localized physical and mechanical properties of the OSB. This allows forming finite element models using x-ray images as geometric model for a given panel for optimizing composite properties.

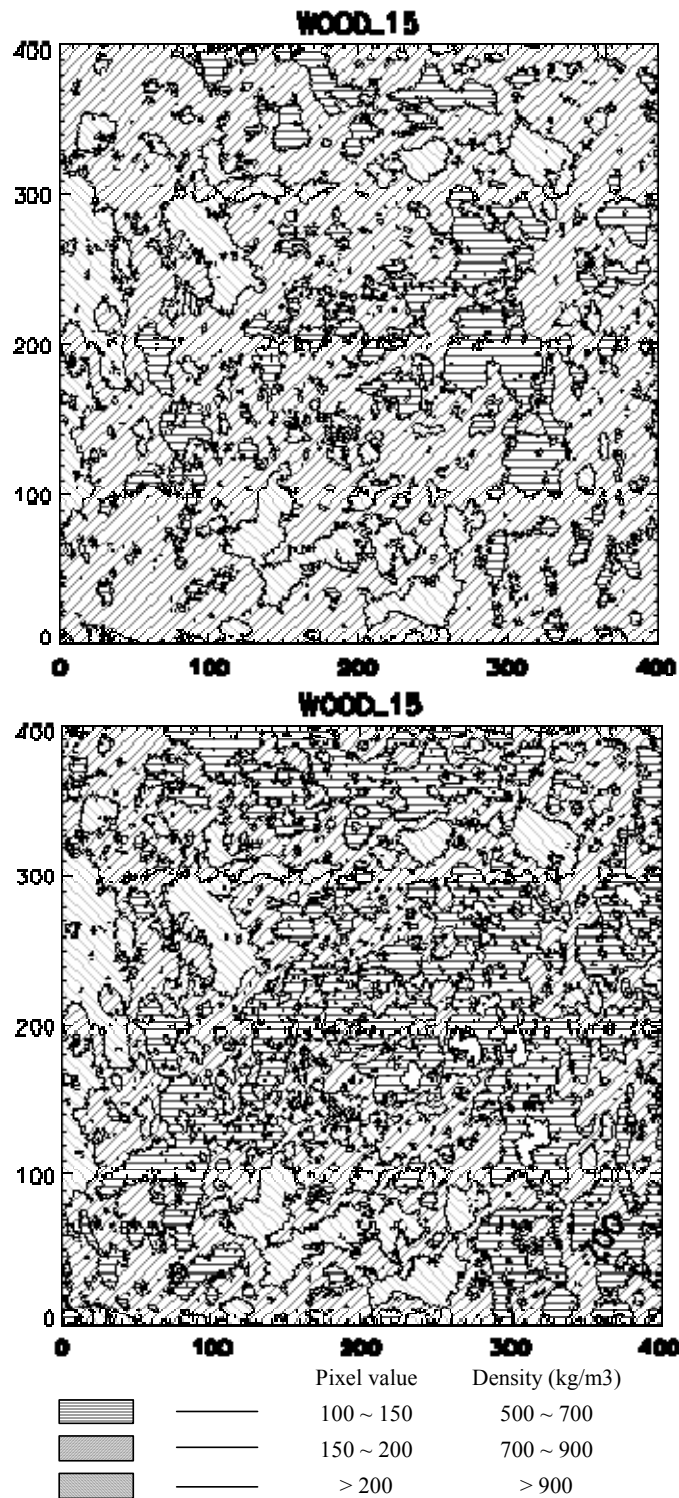


Figure 4-7 Contour plots of in-plane pixel value (left) and density (right) variations (sample S15)

#### 4.1.4 Conclusions

- X-ray scanning technology enables internal structure visualization and characterization of wood material.
- Image processing technology enables phase's identification and quantification (such as voids) in wood panel.
- Density profile can be obtained from image analysis through density – void ratio (or pixel value) correlations.
- This technique shows potential in other material with material density and orientation variance.

## 4.2 The influence of in-plane density variation on engineering properties of oriented strandboard: a finite element simulation<sup>†</sup>

### 4.2.1 Introduction

The formation of OSB mat results in density randomness in the board due to random distribution of air voids. In general, the presence of voids in OSB reduces its elastic moduli and influences its dimensional stability. Therefore, the void structure of OSB is critical for its micro-mechanical modeling (Lenth and Kamke, 1996).

Interest in predicting the performance of wood strand mats has led to research on effect of flake mat structure on panel properties. Suchsland (1962) investigated in-plane density variation and found that strand geometry affects the relative void volume in a mat. Suchsland and Xu (1989) developed a model to simulate in-plane density variation and found that it affects both internal bond and thickness swelling properties. Dai and Steiner (1994a; 1994b) developed a probability-based model for randomly packed, short-fiber-type wood composites assuming that the structural properties are random variables following Poisson and exponential distributions. Lang and Wolcott (1996) developed a Monte Carlo simulation procedure to predict the number of strands in the centroid of imaginary strand columns, the vertical distance between adjacent strands and the position of the column centroid in relation to strand length based on data from laboratory assembled mats. Lenth and Kamke (1996) developed a method to quantify the void structure of a flakeboard mat by analyzing cross sectional void fraction, individual void geometry and distribution.

As regard to the effect of void structure on OSB performance, resource is limited. Hunt and Suddarth (1974) developed a finite-element model to predict tensile and shear moduli of homogeneous flakeboard by assigning strand orientations with a distribution function without consideration of voids. Shaler (1986) developed a model based on the rule of mixture to predict elastic moduli of OSB varying densities, resin levels, strand orientations, and species composition. It was found that elastic modulus could be predicted reasonably well given the properly accounted void volume. However, strand alignment void geometry and distribution were not considered in the model. Lee and Wu

---

<sup>†</sup> Excerpt reprinted from Zhang, B. et al. (2005b).

(2003) developed a two-dimensional model based on continuum theory to predict engineering constants of void-free OSB with orthotropic strand properties, alignment, and panel shelling ratio for three-layer OSB. It was found that the laminate model is capable of predicting two-dimensional elastic moduli and linear expansion of OSB given the strand properties and strand alignment distributions. The orthotropy of the constituent matrix in OSB considerably increases the complexity of the micro-mechanical analysis of the influence of void on engineering constants of OSB, and no such analysis is readily available. The analysis of voids in an orthotropic matrix can, however, base on a numerical solution of certain boundary-value problems. The finite-element method (FEM) has been proven suitable for determining the effective mechanical properties of composite materials with uniform void inclusions (Adams and Doner, 1967; Subramanian, 1993). Wu *et al.* (2003) developed a laminate model based on continuum theory and combined with FEM to predict the effect of voids on engineering constants of OSB. The elemental model shows large effect of in-bedded voids on the engineering constants OSB. It was concluded that FEM shows potential in prediction of elastic properties of OSB. Therefore, a new approach accounting for the important processing parameters, strands alignment and void distribution, is needed to advance current efforts in OSB characterization. The objective of this study was to simulate the effect of in-plane density variation on panel engineering constants and stress distributions for panels at various densities and flake alignment levels.

The objective -- This paper is part of the effort building a model which reflects sample internal structure to calculate anisotropic engineering constants of OSB.

#### **4.2.2 Materials and method**

The engineering constants changes along with the variation of the mean density of OSB and the voids properties (Wu *et al.*, 2003). Modeling the mechanical response of OSB with such variation of density and flake orientation in plane can obtain the equivalent material properties which are essential in design and construction.

##### *4.2.2.1 Panel Considered*

Single layer OSB panels were created to simulate the effect of density distribution and strand alignment levels on elastic modulus and stress distribution of OSB. The strands in the panel were assumed to be aligned in one major direction throughout the board thickness with alignment levels varying from 0, 20, 40, 60, to 80 percent. All panels were assumed to have a mean density of  $0.7 \text{ g/cm}^3$ . Density in the plane of the panel varied according to normal distributions (Figure 4-8) with four standard deviations (0–uniform and control, 0.07, 0.10, and  $0.15 \text{ g/cm}^3$ ). Thus, up to 21.4% density variation was introduced to the panel in simulating its effect on the OSB performance.

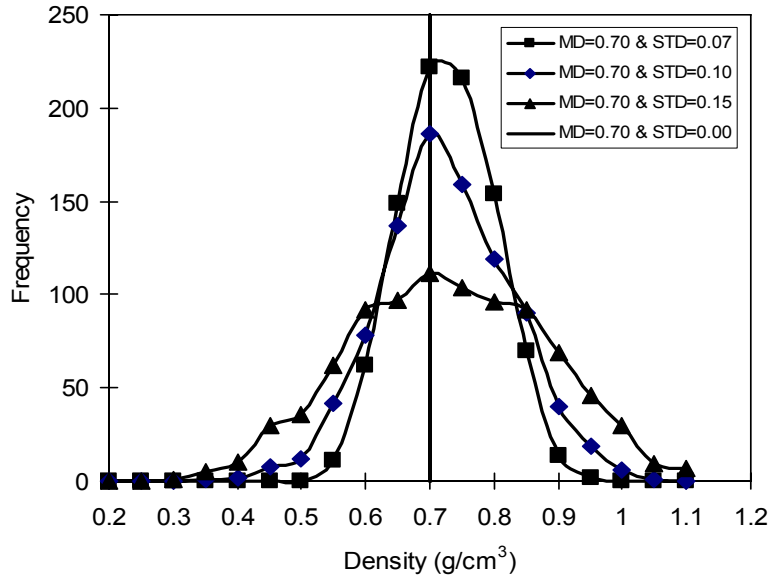


Figure 4-8 Density Distribution

#### 4.2.2.2 Finite Element Model

A square panel with 30 cm edge and 1cm thick was modeled under uniaxial tensile and shear load at two major directions to obtain panel engineering properties. The model was meshed into 900 elements with three dimensional 8-node solid elements (type C3D8 in ABAQUS). The load and boundary conditions were specified in the model as the actual conditions for uniaxial tensile and shear tests (Figure 4-9). The deformations of the panel were used to calculate the orthotropic elastic properties of OSB including Young's modulus, Poisson's ratio, and shear modulus. The stress concentration resulted from heterogeneity of the panel was considered by assigning distributed material constants, which are dependent of variation of density, to different elements. In the simulation, a unit stress was applied for tensile simulation and a unit force was applied for shear testing.

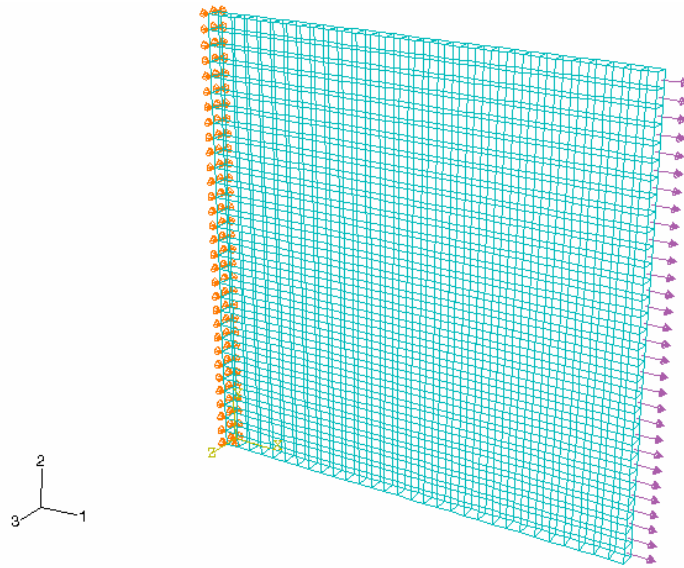


Figure 4-9 Boundary and Loading condition for the simulation test

#### 4.2.2.3 Elemental Material Properties

The anisotropic material properties including Young's modulus, Poisson's ratio, and shear modulus (Table 4-2) were obtained based on density variations and flake alignment levels for a given panel type (Geimer, 1976; Lee and Wu, 2003; Wu *et al.*, 2003). Material constants for each element were generated based on its density value for a panel at a given alignment level. The orientation was expressed in term of percent alignment. It reflects average angle deviation from the reference angle, which is 45 degrees to the principle alignment direction.

$$F.O.(%) = [(45 - \theta)/45] \cdot 100\% \quad (4-1)$$

where,  $\theta$  is the average absolute alignment angle of each panel based on measured angles ( $-90^\circ$  to  $90^\circ$ ).

The material local coordinates were set as the global coordinate system. Anisotropic elastic material properties (E11, E22, E33, G12, G23, G31,  $\nu_{12}$ ,  $\nu_{23}$ , and  $\nu_{31}$ ) were assigned to each element with a FORTRAN program in the format of ABAQUS input file.

Table 4-2 Elemental engineering constants of OSB

Engineering Properties	Flake Orientation (%)				
	0	20	40	60	80
E1 (GPa)	5.839	7.258	8.77	10.361	11.776
E2 (GPa)	5.827	4.496	3.16	1.816	0.454
E3 (GPa)	0.13	0.13	0.13	0.13	0.13
G12 (GPa)	2.33	2.268	2.12	1.891	1.586
G13 (GPa)	0.26	0.26	0.26	0.26	0.26
G23 (GPa)	0.12	0.12	0.12	0.12	0.12
$\nu_{12}$	0.219	0.272	0.34	0.479	1.237
$\nu_{13}$	1.70	1.70	1.70	1.70	1.70
$\nu_{23}$	1.02	1.02	1.02	1.02	1.02

#### 4.2.2.4 Predicting Panel Engineering Constants

Panel's material constants calculated in this study are Young's modulus, Poisson's ratio and shear modulus. They were calculated based on the FEM simulation of tensile and shear testing (Figure 4-10). Simple tensile tests in each of the two perpendicular directions and shear tests along these two perpendicular directions were conducted to obtain translate and rotational displacements in both directions, which were used to calculate the material equivalent constants. The Young's modulus and Poisson's ratio were determined through tensile tests along the two major directions and shear modulus through shearing condition simulation.

There were a total of 80 simulations for panels at one mean panel density with four density distributions. The results were used to establish the correlation of the material overall constants with the density variation in the panel plane.

The material constants determined in this study were those in the plane of wood panel, i.e. in the 1 and 2 direction of the simulation model ( $E_{11}$ ,  $E_{22}$ ,  $\nu_{12}$ ,  $\nu_{21}$ ,  $G_{12}$ ,  $G_{21}$ ). There were obtained through equations (4-2).

$$\begin{aligned} \varepsilon &= \frac{\Delta L}{L} \\ E &= \frac{\sigma}{\varepsilon} \\ G &= \frac{\tau}{\gamma} \end{aligned} \tag{4-2}$$

where  $\Delta L$ ,  $L$ ,  $\sigma$ ,  $\tau$  were specified in Figure 4-10.

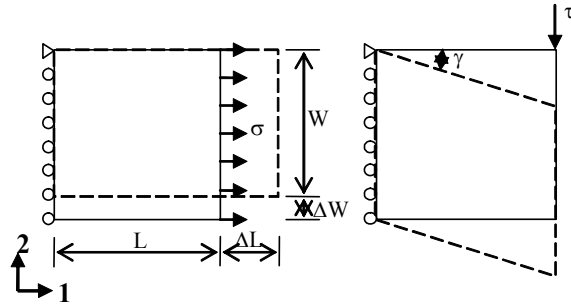


Figure 4-10 Simulated Tensile and Shear Tests

There were two different mean densities used in the simulation. For every mean density level, there were three standard deviations for the density variation as well as one uniform density sample as a comparison. Totally 160 simulations were carried out in order to obtain the material constant. These results were used to establish the correlation of the material overall constants with the density variation in the panel plane.

#### 4.2.2.4.1 Predicting in-plane stress variation

The in-plane stress variation was evaluated by calculating the stress concentration factor for each tensile stress simulation. Contour plots of in-plane stresses under tensile loading was made for each simulation condition and arranged according to the density distributions. The average stress was acquired for stress at the integration point of each element. The stress concentration factor was determined as the ratio of the stress at the integration point to the average stress. The maximum stress concentration factor for each simulation sample was obtained and studied against the variation of density deviation.

#### 4.2.2.4.2 Predicting out-of-plane stress variation

Since the out-of-plane stresses have both positive and negative values, the out-of-plane stress variation was analyzed by calculating the maximum differential of out-of-plane stresses for in-plane stress situation instead of the stress concentration factor. Maximum and minimum out-of-plane stresses were identified for every simulation and the maximum stress differential was determined and plotted with respect of density variation. Contour plots of out-of-plane stresses were made for each simulation condition and arranged according to the density variation.

### 4.2.3 Results and discussion

#### 4.2.3.1 *Predicted Engineering Constants*

The overall performance of the OSB board in this study was assessed in term of modulus (material constants) and strength (stress concentration). The material constants obtained from the FEM simulation are tabulated in Table 4-3 according to the density standard variation and flake orientation.

The simulated results (Table 4-3) show that with the increase of strand orientation in one direction, Young's moduli in that direction increase. And, a decrease of moduli occurs in the transverse direction (Figure 4-11). Poisson's ratios follow the similar characteristics (Figure 4-12). Shear moduli all decrease with the increase of flake alignment level (Figure 4-13). Thus, strand alignment level has large effect on the elastic constants of single-layer OSB. At the same flake orientation level, Young's moduli, Poisson's ratios, and shear moduli decrease slightly as the standard deviation of the density distribution increases (Figure 4-14 to Figure 4-16). This indicates that the overall panel elastic behavior may vary, but only slightly, with the density deviation at the same mean density level as long as there is no damage initiated in the board. However, the panel with large density deviation may incur high stress concentration which leads to early damage.

Table 4-3 Predicted material constants (mean density =0.7 g/cm<sup>3</sup>)

Dev.	F.O. (%)	E1 (GPa)	E2 (GPa)	v12	v21	G12 (GPa)	G21 (GPa)
0.00	0	5.84	5.83	0.22	0.22	0.21	0.23
	20	7.26	4.50	0.27	0.17	0.19	0.23
	40	8.77	3.16	0.34	0.12	0.17	0.21
	60	10.36	1.82	0.48	0.08	0.15	0.18
	80	11.77	0.45	1.24	0.05	0.10	0.08
0.07	0	5.83	5.82	0.22	0.22	0.20	0.22
	20	7.25	4.49	0.27	0.17	0.19	0.22
	40	8.66	3.13	0.34	0.12	0.18	0.21
	60	10.34	1.82	0.48	0.08	0.14	0.17
	80	11.75	0.46	1.24	0.05	0.09	0.08
0.10	0	5.77	5.76	0.22	0.22	0.21	0.23
	20	7.17	4.45	0.27	0.17	0.20	0.23
	40	8.75	3.16	0.34	0.12	0.17	0.21
	60	10.22	1.80	0.48	0.08	0.15	0.18
	80	11.61	0.45	1.24	0.05	0.10	0.08
0.15	0	5.75	5.72	0.22	0.22	0.20	0.21
	20	7.14	4.42	0.27	0.17	0.19	0.21
	40	8.61	3.12	0.35	0.13	0.17	0.20
	60	10.16	1.80	0.48	0.09	0.14	0.17
	80	11.46	0.45	1.24	0.05	0.09	0.08

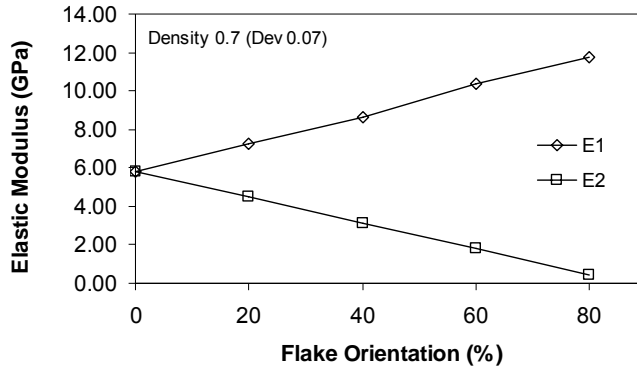


Figure 4-11 Elastic Modulus vs. Flake Orientation at Various Density Deviation Levels

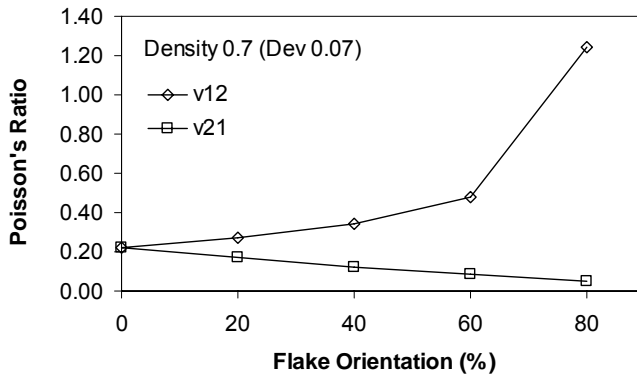


Figure 4-12 Poisson's Ratio vs. Flake Orientation at Various Density Deviation Levels

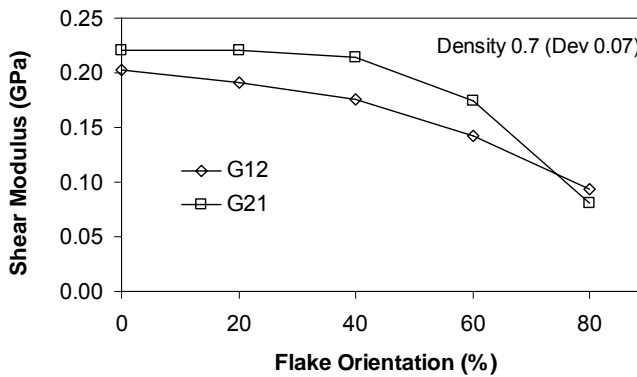


Figure 4-13 Shear Modulus vs. Flake Orientation at Various Density Deviation Levels

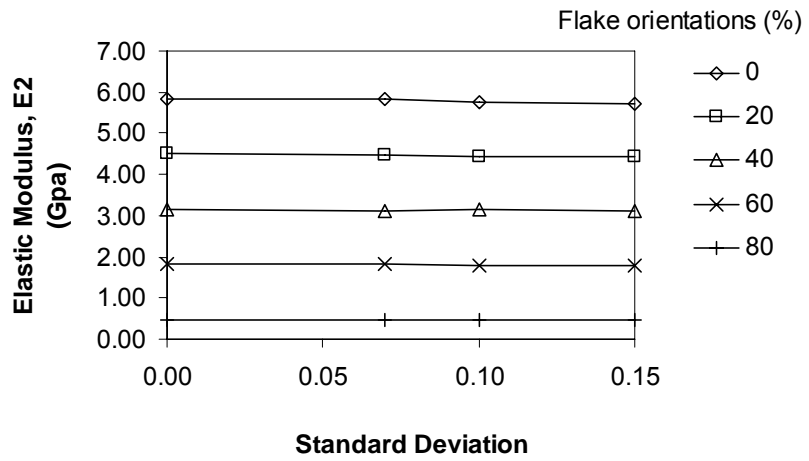
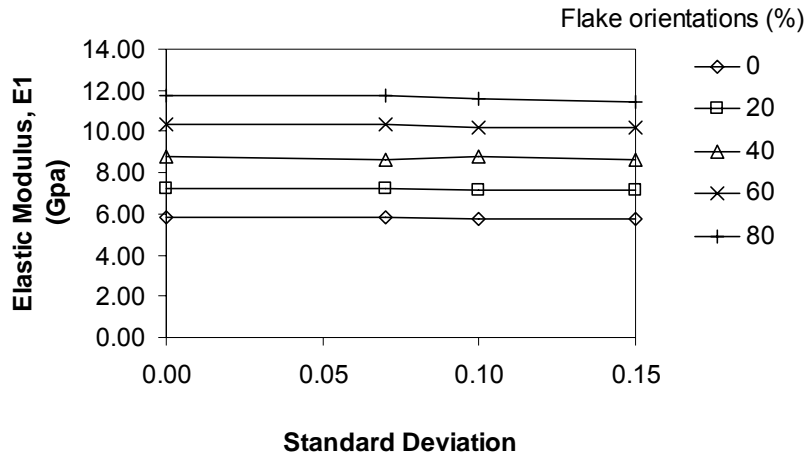


Figure 4-14 Elastic modulus vs. density deviation at deferent density deviation levels

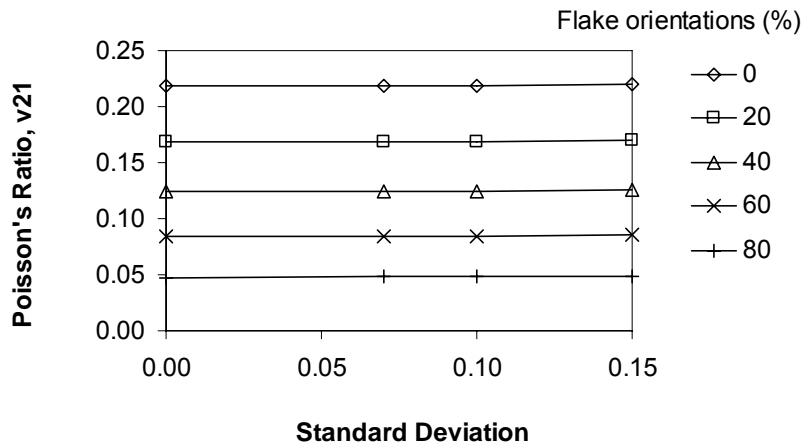
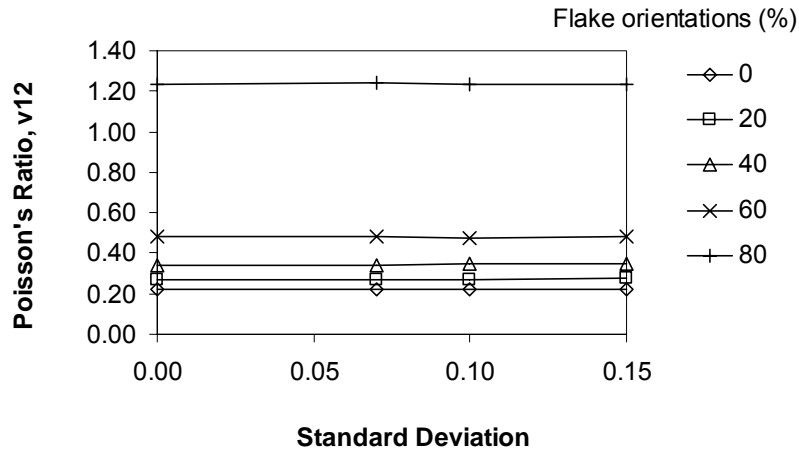


Figure 4-15 Poisson's ratio vs. density deviation at different density deviation levels

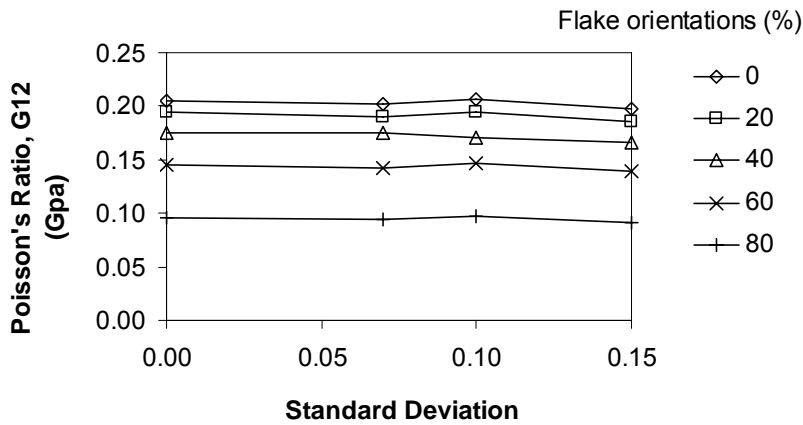


Figure 4-16 Shear modulus vs. density deviation at different density deviation levels

#### *4.2.3.2 Predicted In-Plane Stress Distribution*

The in-plane stress concentration factors were obtained based on the tensile tests with the change of the standard deviation of the density distribution and strand orientation. Results are tabulated in Table 4-4. The in-plane stress distributions are highly dependent on density variation. From the series of simulation results with various density deviations and flake alignment levels, it is observed (Figure 4-17) that the stress concentration factor increases with the increase of the standard deviation of the in-plane variation of the density of the OSB boards. However, at the same standard deviation level, the change of the stress concentration factor for different flake orientations was insignificant. This indicates that the density deviation of the OSB dominates the strength properties of the board and hence controls its quality. With additional density deviations in the simulation, the stress concentration factor vs. standard deviation curve for a given board type can be established. The information can be used to predict the strength properties of OSB based on quality control data or to set quality control target with the aimed strength expectation. From the previous study of the x-ray tomography and image analysis of OSB, the actual density deviation of the OSB can be obtained and used for such an analysis.

Table 4-4 Predicted In-plane Stress Concentration Factors at Different Density Deviation and Flake Orientation Levels

Density Deviation	Flake Orientation (%)	s11	s22
0.00	0	1.00	1.00
	20	1.00	1.00
	40	1.00	1.00
	60	1.00	1.00
	80	1.00	1.00
0.07	0	1.28	1.26
	20	1.27	1.27
	40	1.26	1.27
	60	1.26	1.29
	80	1.27	1.41
0.10	0	1.42	1.38
	20	1.43	1.38
	40	1.43	1.39
	60	1.43	1.40
	80	1.45	1.61
0.15	0	1.71	1.63
	20	1.71	1.61
	40	1.70	1.60
	60	1.70	1.59
	80	1.82	1.92

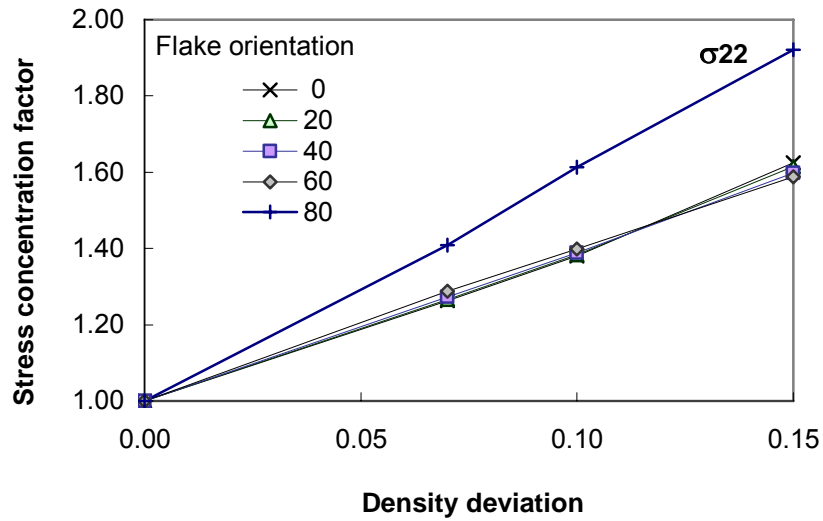
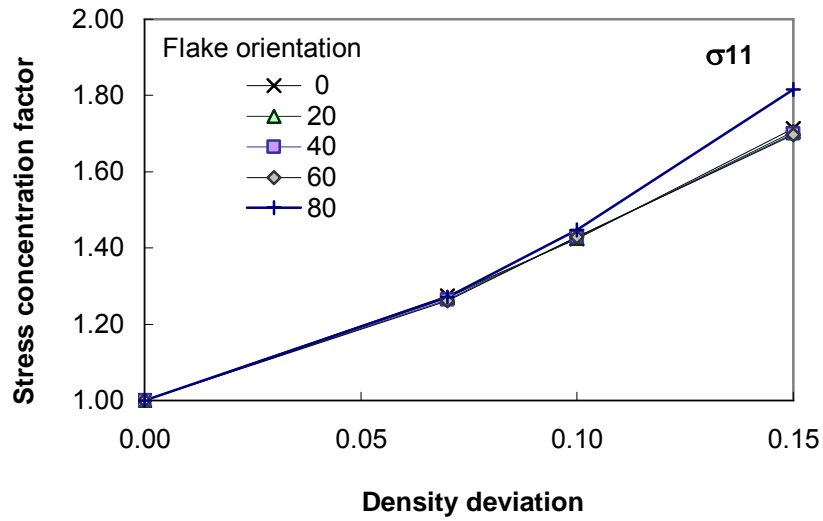


Figure 4-17 Stress concentration factors at different density deviation levels

#### 4.2.3.3 Predicted out-Plane Stress Distribution

With regard to the out-of-plane stresses (Figure 4-18), there is a trend showing clearly that the out-of-plane stress variation also increases with the increase of the in-plane density deviation of the panel. This indicates that the out-of-plane stress concentration is also strongly affected by the in-plane density deviation. These stresses will contribute to early damage or separation between strand layers. This is especially significant under swelling conditions with large normal swelling stresses. The maximum out-of-plane stress differential plot (Figure 4-19) shows a clear trend of the effect of density variation on the out-of-plane stress variation for each flake alignment level. Thus,

the out-of-plane stresses varied significantly with the increase of the in-plane density deviation.

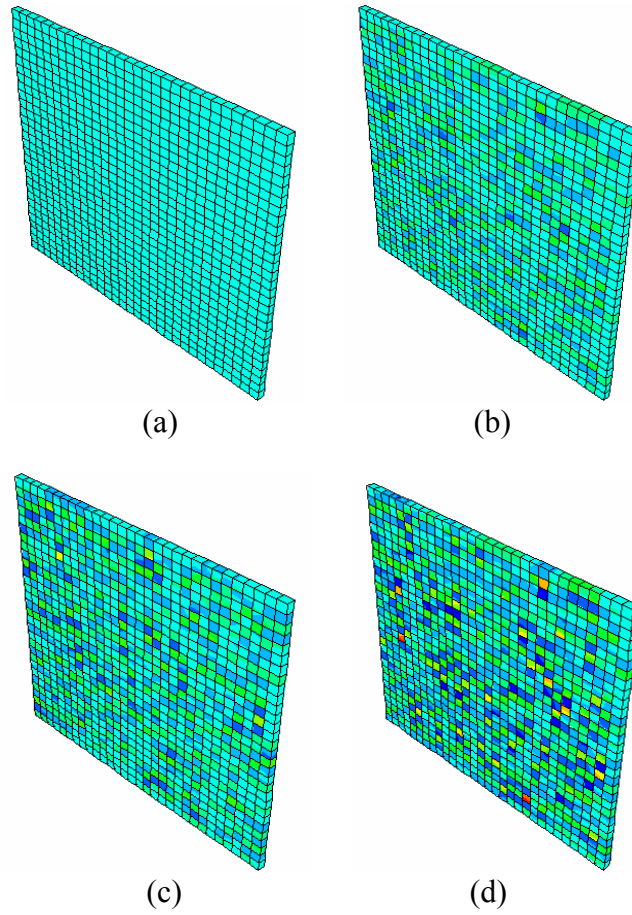


Figure 4-18 Out-of-Plane Stress (Mean density = 0.7, POA = 0): (a) Uniform density; (b) Deviation = 0.07; (c) Deviation = 0.10; (d) Deviation = 0.15

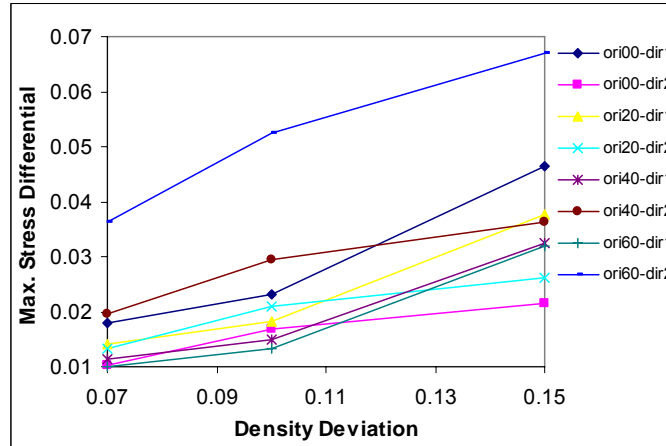


Figure 4-19 Maximum stress differential of out-of-plane stresses at different density deviation levels

#### 4.2.4 Conclusions

In-plane density variation in OSB is an inherent property due to randomness in mat forming. In this work, elastic properties and in-panel stress concentrations of single-layer OSB under several density distributions and flake orientations were predicted using a finite element model. A FORTRAN program was written to automatically create the simulation model in ABAQUS for sets of material property input. It was found that the variation of in-plane density resulted in significant variation of localized stress concentrations both in and out-of-the-plane. The overall panel elastic behavior varied slightly with the density deviations at the same mean density level, as long as there is no damage initiated in the board.

### 4.3 Characterization of engineering performance of oriented strandboard with combined computer tomography and finite element techniques

#### 4.3.1 Panel geometry model

Three-layer OSB with different flake orientation and flake quality for face and core layers was considered (i.e., large wood flake versus fines). Related panel production information is summarized in Table 4-5. Two OSB samples with nominal size of 76-mm (length) by 76-mm (width) by 12-mm (thickness) were prepared from each panel group. Density distribution through sample thickness was measured with an x-ray based densitometer for all samples.

Each sample was scanned with x-ray tomography imaging system to obtain 20 cross-section images through sample thickness. Eight slices was scanned in one rotation and the slice increment was about 0.5 mm. The average value of eight shot at one position was used for following image reconstruction and analysis. For each sample, each slice represents about 0.5 mm thick of internal structure.

The layer division for each sample includes 5 slices for each of the two face layers and 10 slices for the core layer. From the analysis, pixel-value map for each layer was obtained. The correlation between layer mean density and pixel value was obtained for each sample.

A four layer panel was formed by combining the outer five slices from each surface to form two face layers and combining and dividing the inner 10 slices to form two core layers with five slices for each layer (Figure 4-28).

The pixel-value map for each layer in the four-layer panel was generated by combining measured pixel values at each corresponding position of individual slices forming the layer.

2500 discrete pixel values were generated from the layer pixel-value map to represent the layer (Figure 4-20 and Figure 4-21).

Local density corresponding to each pixel value was predicted using the pixel value –density correlation (Figure 4-22 and Figure 4-23).

Elemental material properties were generated using regression models describing relationships among panel property, density, and fines content for the layer (Han and Wu Paper) (Figure 4-24 to Figure 4-27).

### **4.3.2 Finite element model**

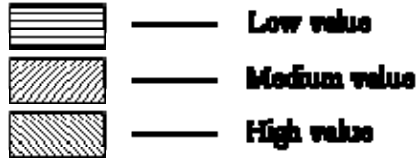
A model with totally 10000 elements for four layers was created to simulate each quarter of the testing sample. A 3-D 8-node element type was used in the modeling (Figure 4-28). Pixel variation for each layer of the panel was generated with IDL programming which can be read by FORTRAN program. A FORTRAN program was written to automatically import this information of pixel value variation and calculate elastic modulus based on pixel-density correlation and density-elastic modulus relation obtained from previous studies. It also generates ABAQUS input file and output request based on these information and intended test simulation. Considering the variation of material properties due considerable density variation of the OSB board, each element was assigned a set of material constants according to the local density obtained from image processing (described in detail in 4.1 at page 18). Orthotropic material properties were considered in this study and simulation. The loading and boundary conditions were set to be the same as real test conditions of uniaxial tensile test. They are illustrated in Figure 4-29.

### **4.3.3 Results and discussion**

#### *4.3.3.1 Legend of Contour Plot*

The pixel value ranges from 0 to 255 while density ranges from 0 to 100 and E1/E2 from 0 to over 30. However, in order to make the contour plot easy to read, the contoured lines were chosen at the medium value. For pixel value, 100, 150 and 200 were used. For density map, 600, 800 and 1000 were used. For material constants, E1 and E2, 5, 10 and 15 was used based on the mean value of about 10 in the measurement.

The legend of the contour plot is following the low, medium and high area as below:



#### 4.3.3.2 Elemental Pixel-value and Density Distribution

Typical pixel value map and corresponding density map (generated from data of panel S09 and S15) were shown in Figure 4-20 to Figure 4-21 and Figure 4-22 to Figure 4-23, respectively. From the pixel map, it was observed that the pixel value distributes more uniform in surface layer than in core layers and generally pixel value in surface layer is larger than in core layers. The map pattern is also different between sample S09 and sample S15. This may be due to the difference of fine levels. The fine level of S15 is 100% and S09 is 22.2%.

#### 4.3.3.3 Engineering Property Variation

The contour plots of elastic modulus across the panel plane were illustrated in Figure 4-24 to Figure 4-27. It can be observed from the graph that the face layer is generally stiffer than the core layer and the distribution of the elastic modulus is more uniform. Comparing S09 and S15, the elastic modulus of S15 is much more uniform than S09 which has smaller fine level.

The predictions of E1 and E2 for all samples are plotted against measurement in Figure 4-32. Besides the existing variations the general trends of E1 and E2 agree with that of measurement. This implies that the proposed methodology may be used to evaluate the performance of OSB board.

#### 4.3.3.4 Predicted Stress Distributions

Figure 4-30 and Figure 4-31 show deformed shape of sample S09 and S15 under uniaxial tensile loading. From the deformation data file, the Poisson's ratio of the panel can be calculated. Typical stress contours from the simulation results were plotted in Figure 4-33 and Figure 4-34 for sample S09 and S15. For the tension test along axis 1, the stress in face layer is considerably larger than in the core layer due to the different stiffness of these two layers.

The difference between the predicted and measured E2 may be due to the influence of the fiber orientation. Since the fiber orientation was mainly at the 1 direction, the modulus of the 2 direction will be considerably smaller than the situation there is no bias of the major fiber orientation.

### 4.3.4 Conclusions

A three-layer (two face layers and one core layer with different flake alignment level) FEM model was formulated to investigate performance of anisotropic wood composite based on the one-layer FEM study. The FEM geometry model was built based on X-ray tomography and image analysis reflecting the actual microstructure of the

testing samples to account for real density variation. Sample performance was characterized numerically with FEM simulation to conduct digital testing of wood composite material.

#### 4.4 Acknowledgment

This study was supported by the National Research Initiative of the USDA Cooperative State Research, Education and Extension Service, grant number 2003-35103-13677.

Table 4-5 Summary of Basic Sample Information and measured void ratios

Sample ID	Panel Construction <sup>a</sup>	Density <sup>b</sup> (g/cm <sup>3</sup> )	Sample Dimension		
			Length (cm)	Width (cm)	Thickness (cm)
S07	Face: 55%WFL	0.73	7.61	7.76	1.12
S08	Core: 45%WFL	0.70	7.77	7.56	1.18
S09	Face: 55%WFL	0.69	7.79	7.54	1.15
S10	Core: 10%WCM & 35%WFL	0.71	7.59	7.78	1.18
S11	Face: 55%WFL	0.75	7.78	7.59	1.18
S12	Core: 20%WCM & 25%WFL	0.73	7.79	7.57	1.18
S13	Face: 55%WFL	0.64	7.74	7.51	1.12
S14	Core: 30%WCM & 15%WFL	0.62	7.77	7.50	1.16
S15	Face: 55%WFL	0.71	7.56	7.78	1.19
S16	Core: 45%WCM	0.69	7.79	7.55	1.15

<sup>a</sup> WFL – Wood face large (flake); and WCM – Wood core material.

<sup>b</sup> Volume based on 6% moisture content.

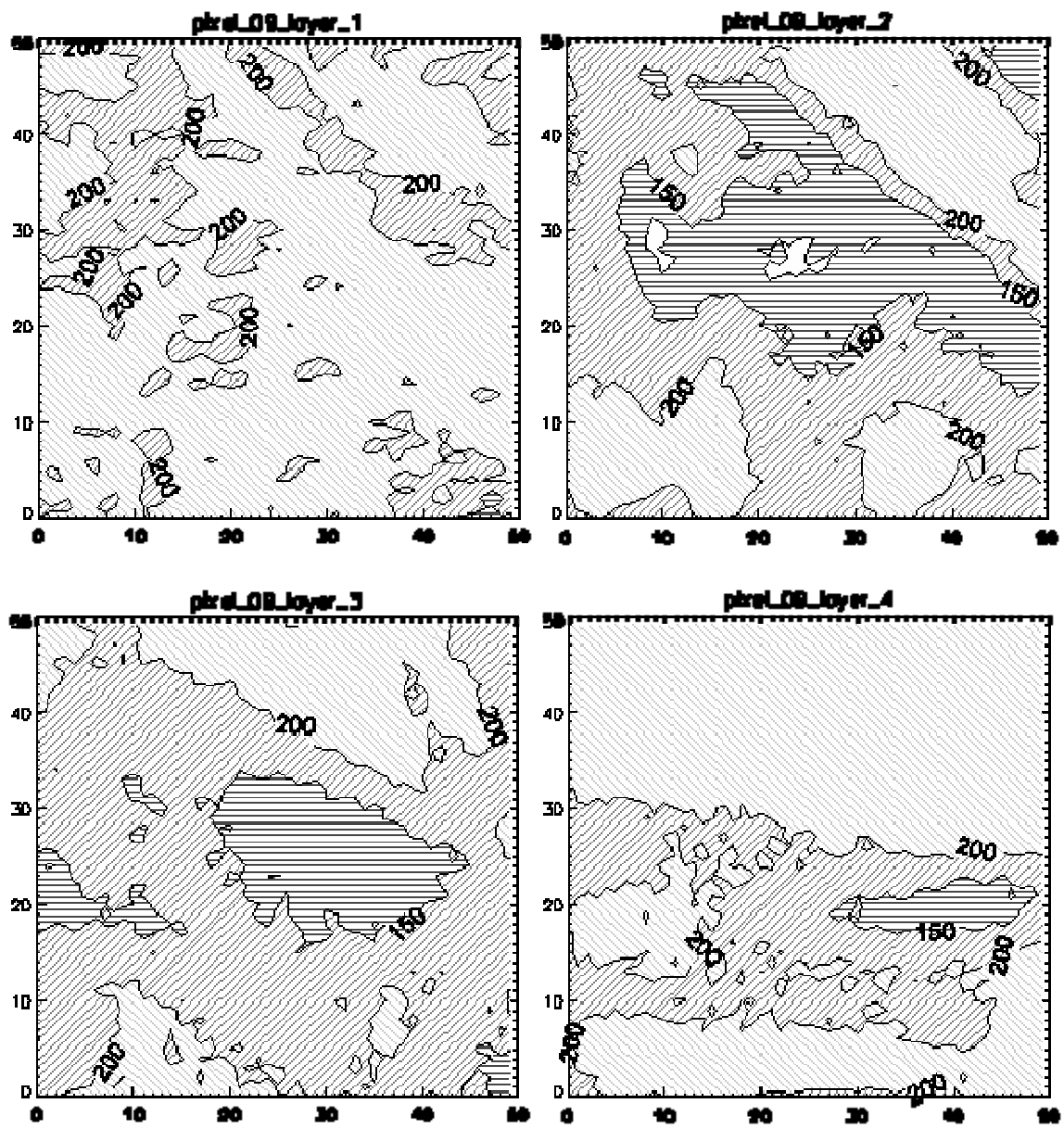


Figure 4-20 Pixel value contour plot (S09)

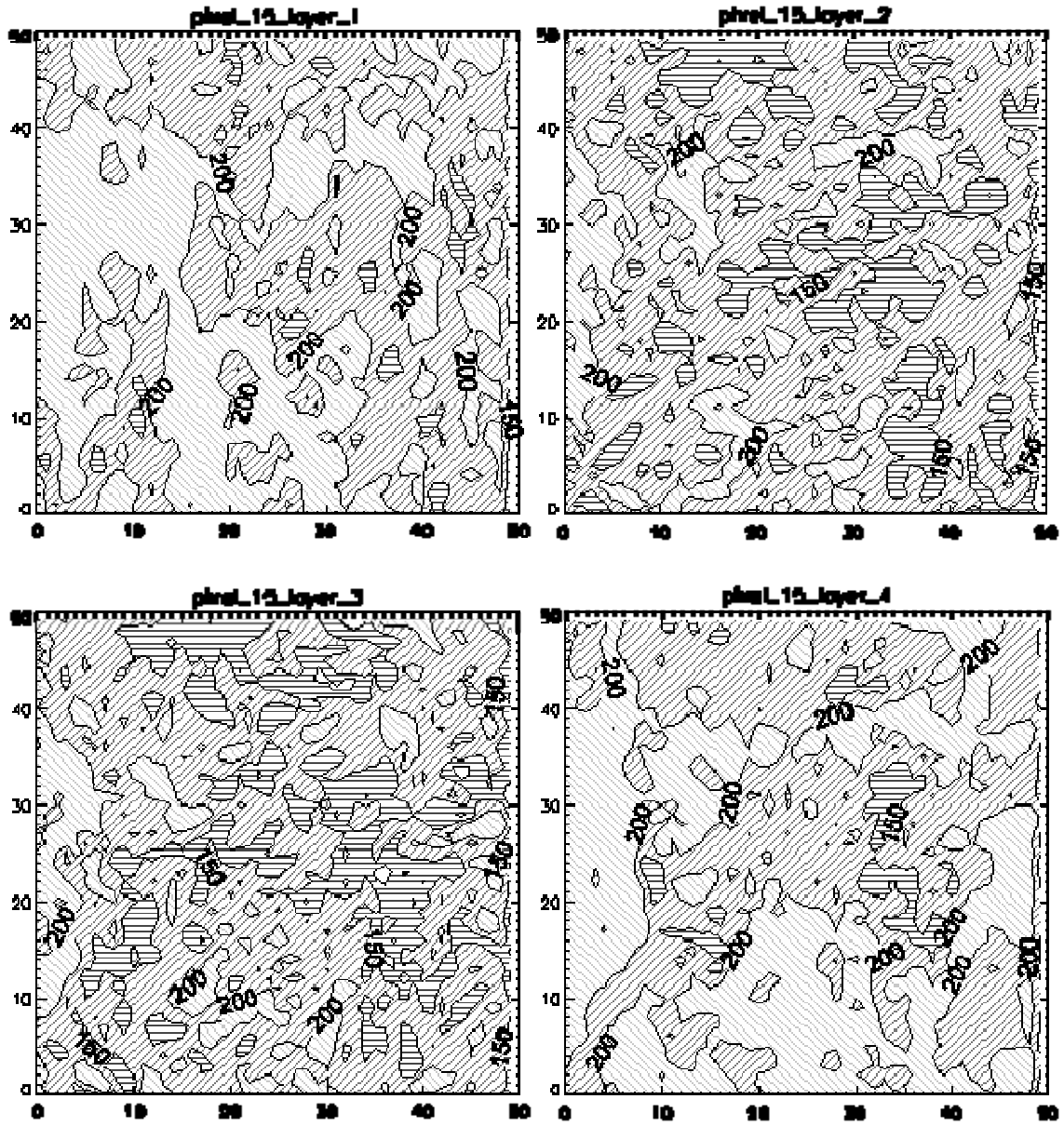


Figure 4-21 Pixel value contour plot (S15)

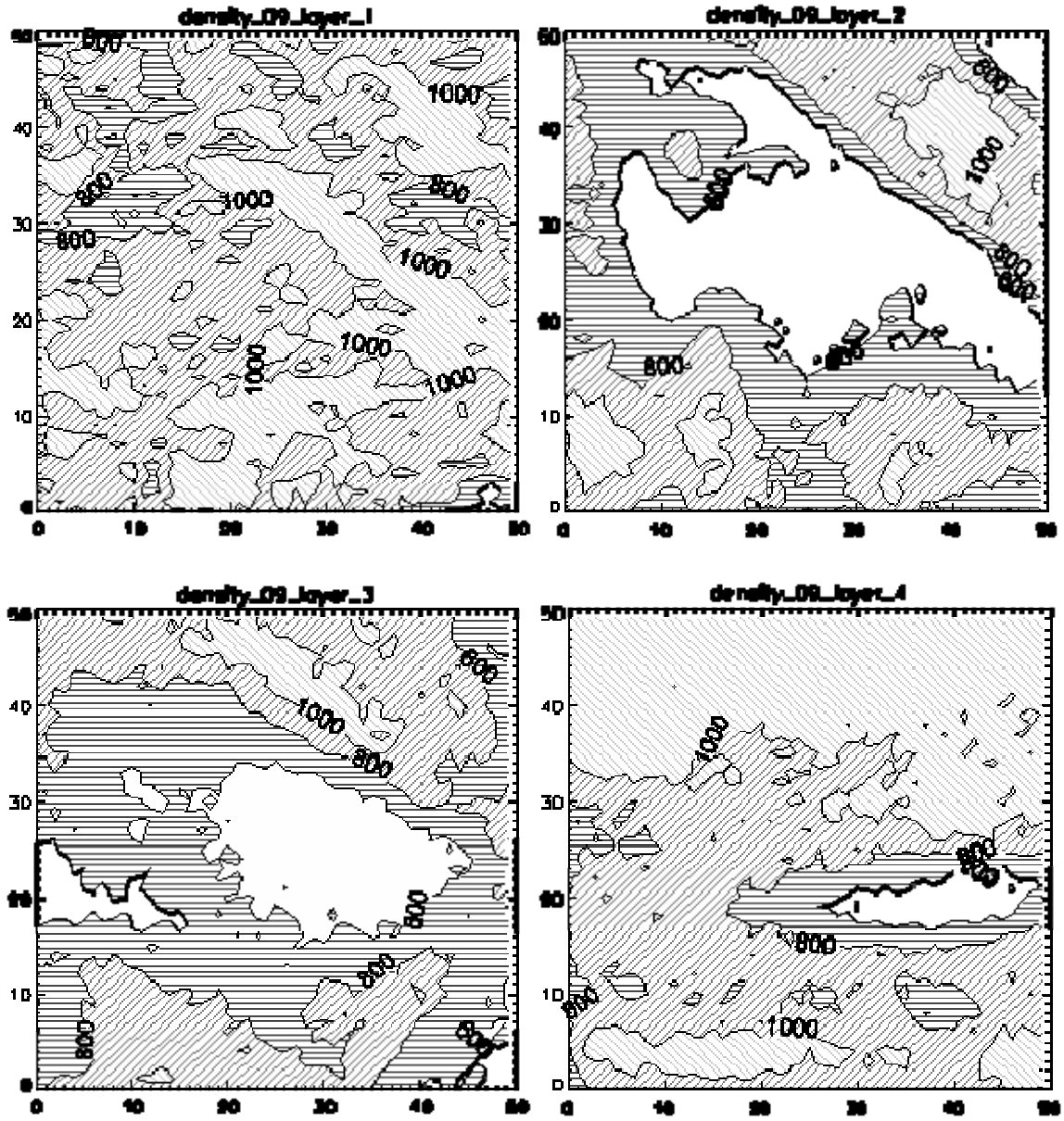


Figure 4-22 Density contour plot (S09)

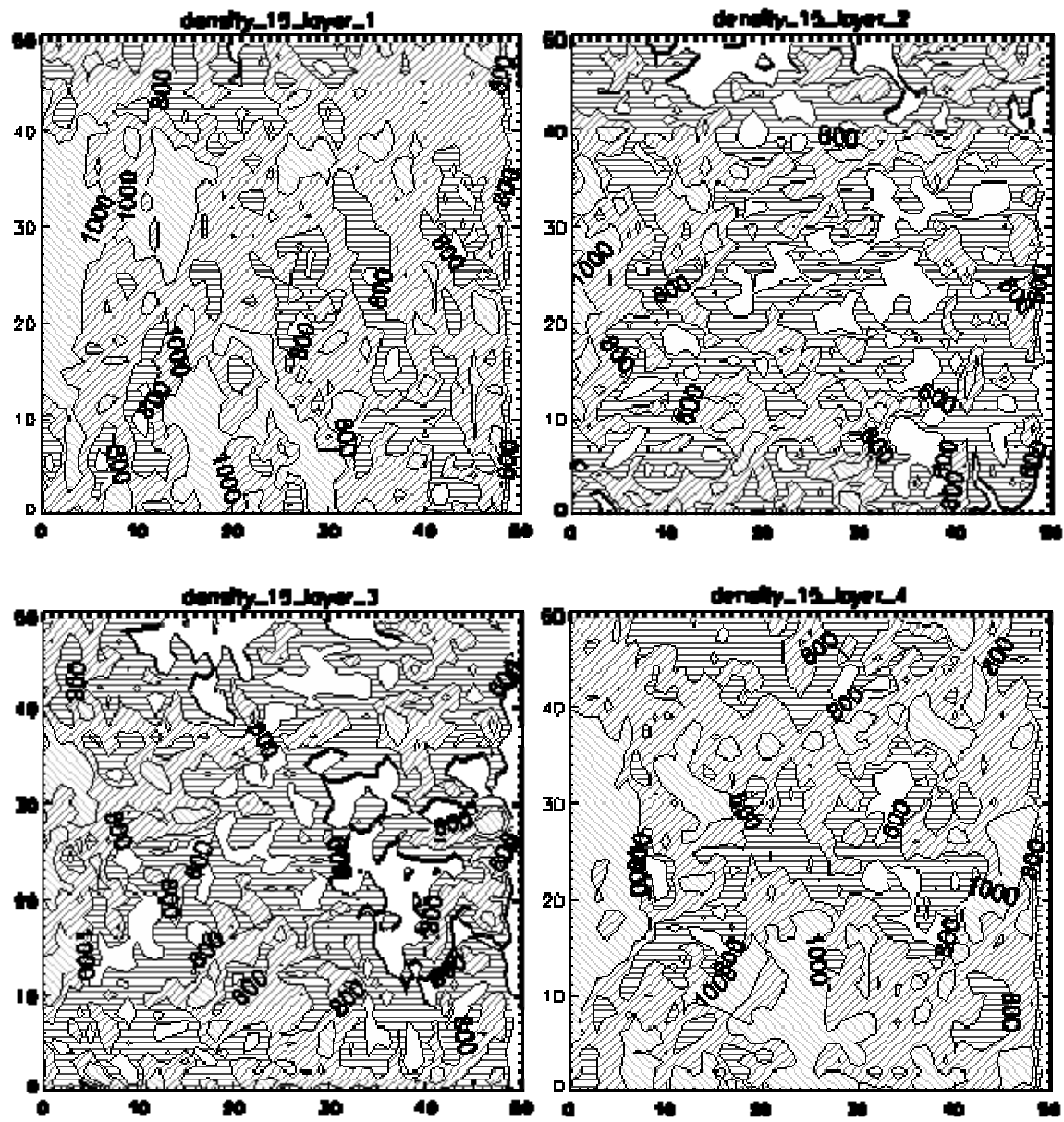


Figure 4-23 Density contour plot (S15)

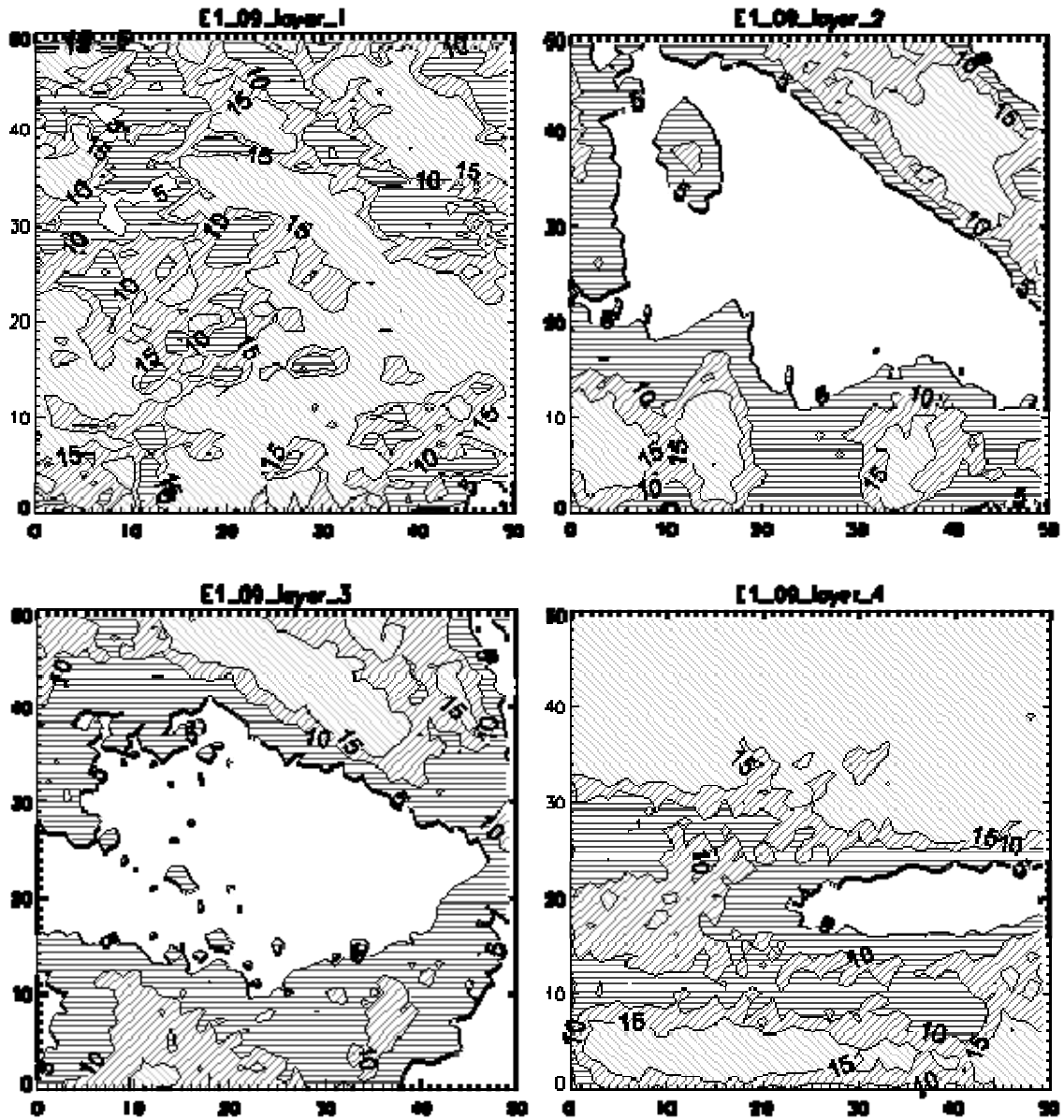


Figure 4-24 E1 contour plot (S09)

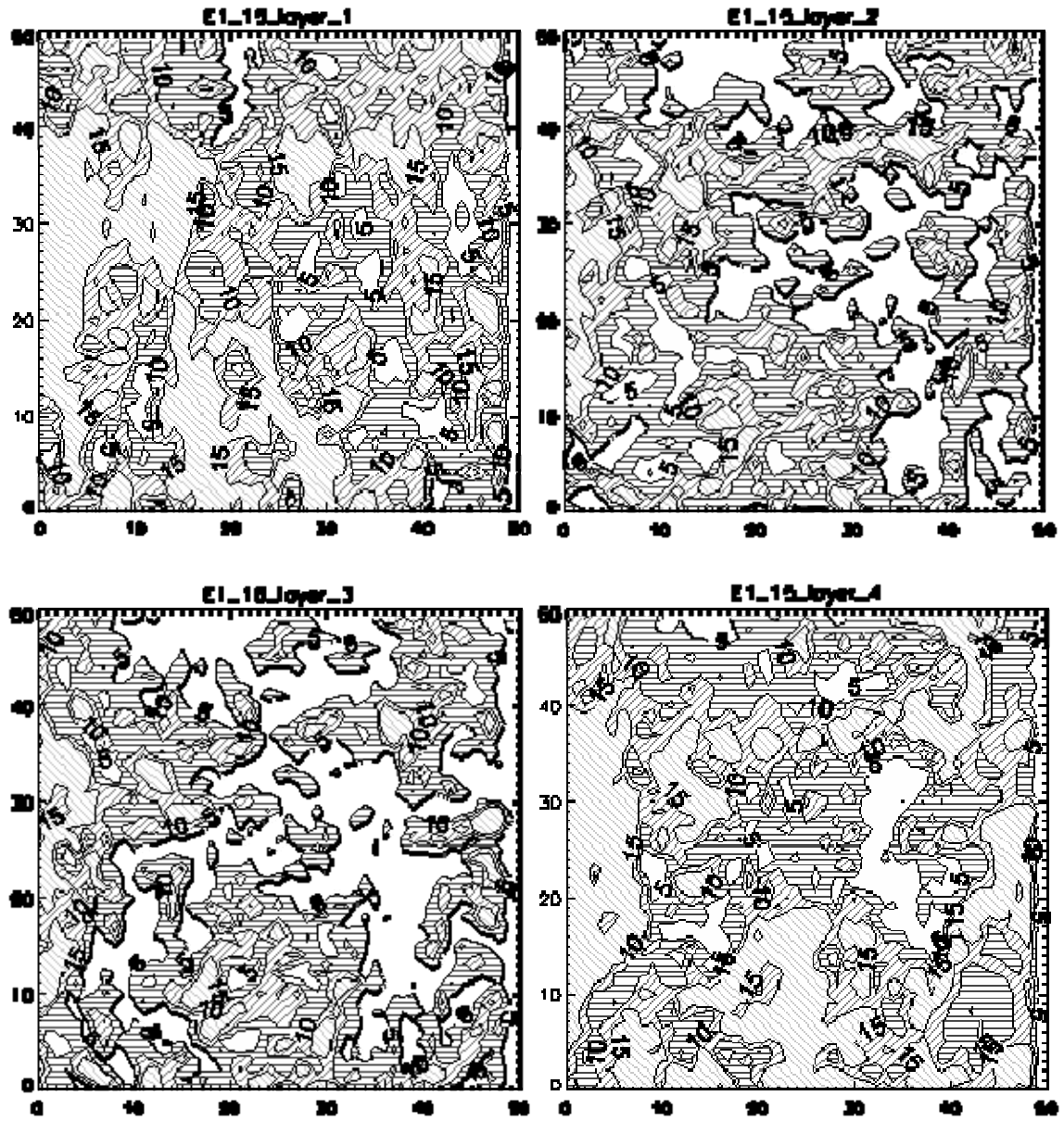


Figure 4-25 E1 contour plot (S15)

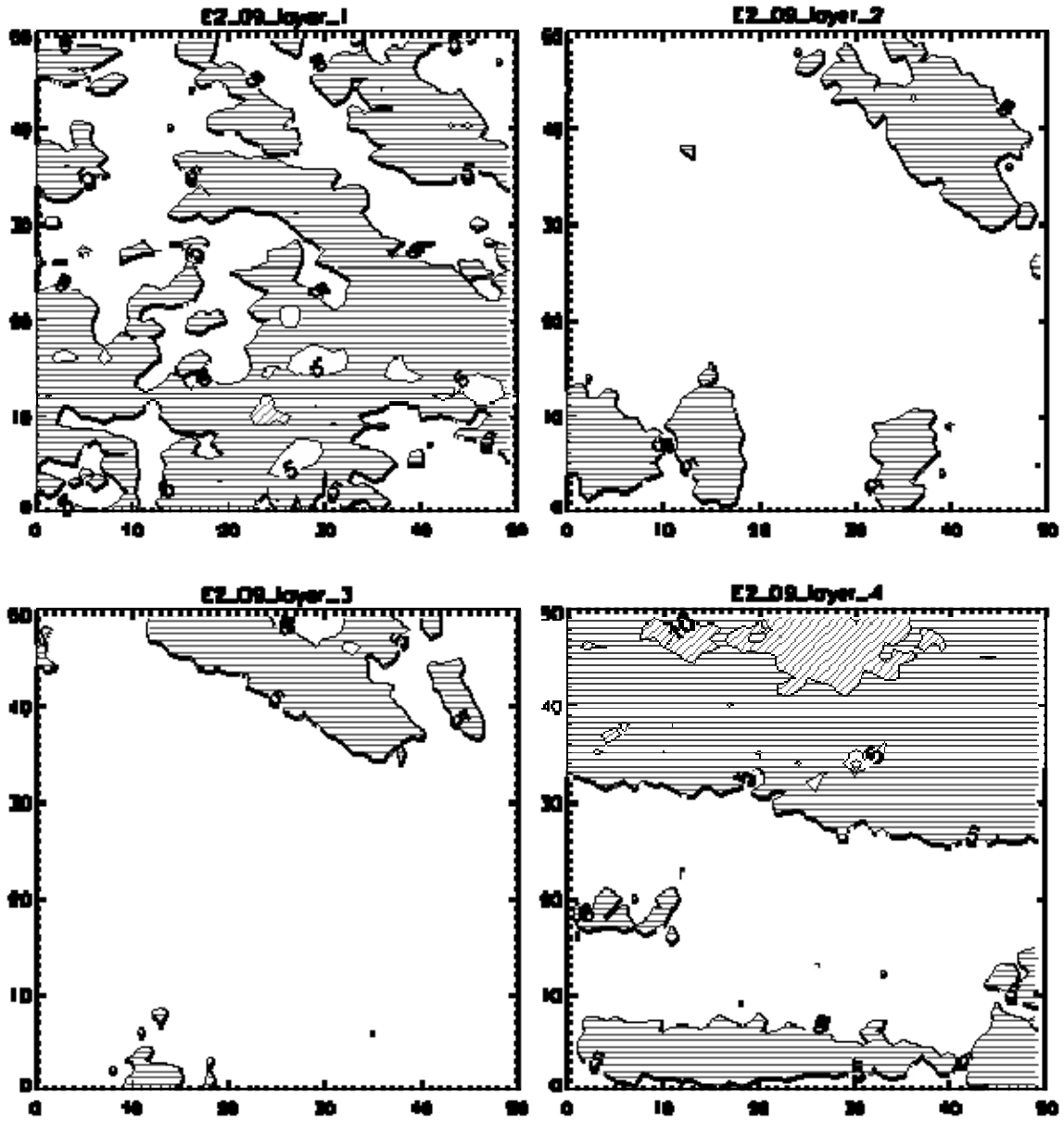


Figure 4-26 E2 contour plot (S09)

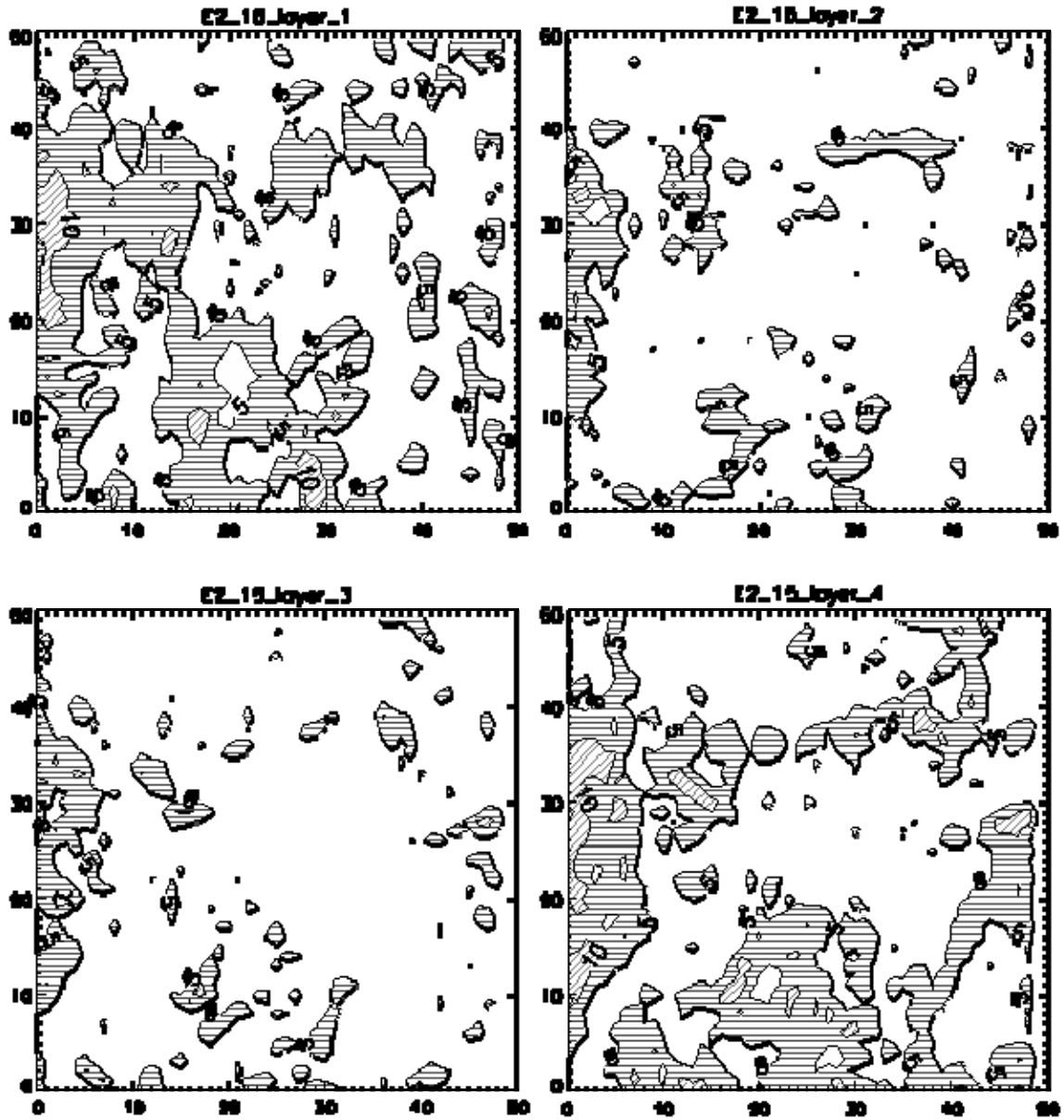


Figure 4-27 E2 contour plot (S15)

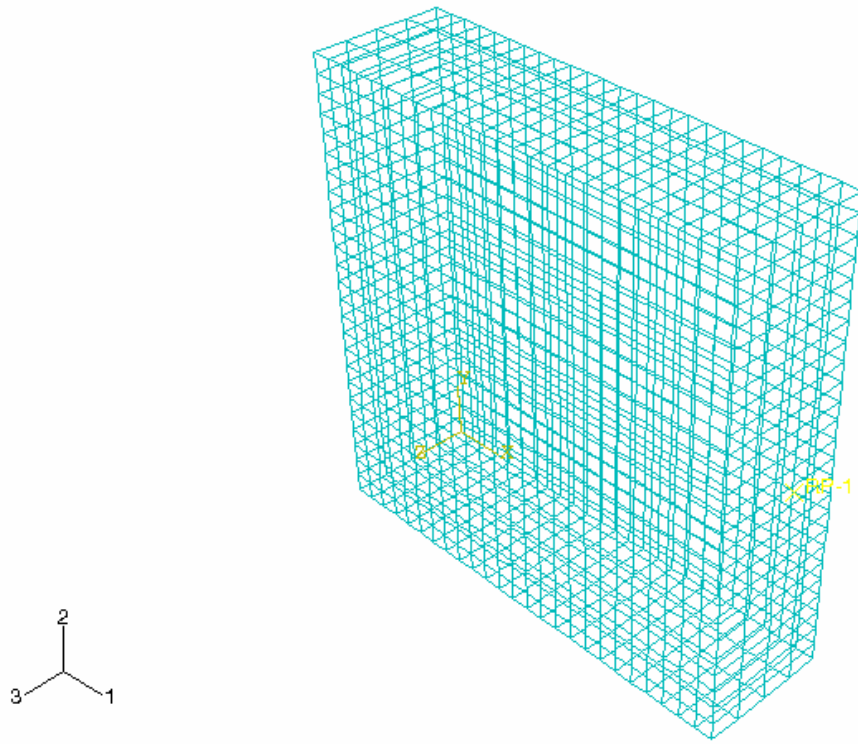


Figure 4-28 Mesh of three-layer OSB simulation model

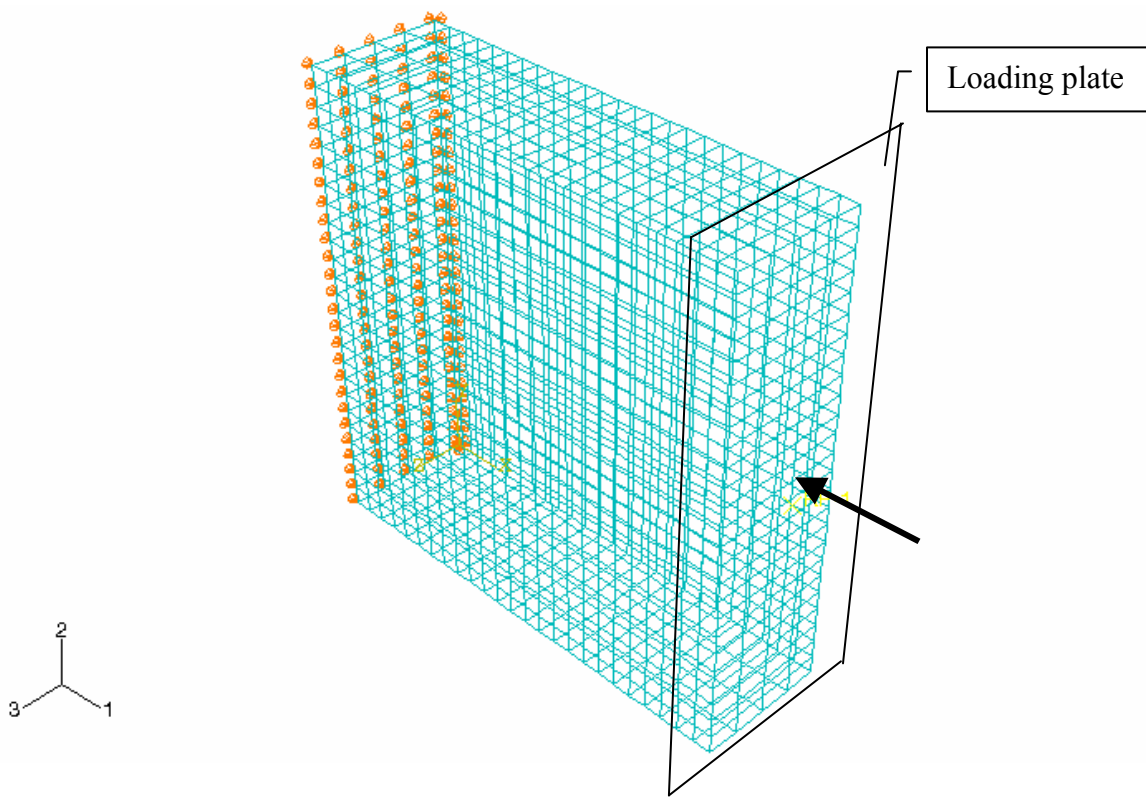


Figure 4-29 Boundary and loading condition of three-layer OSB simulation model

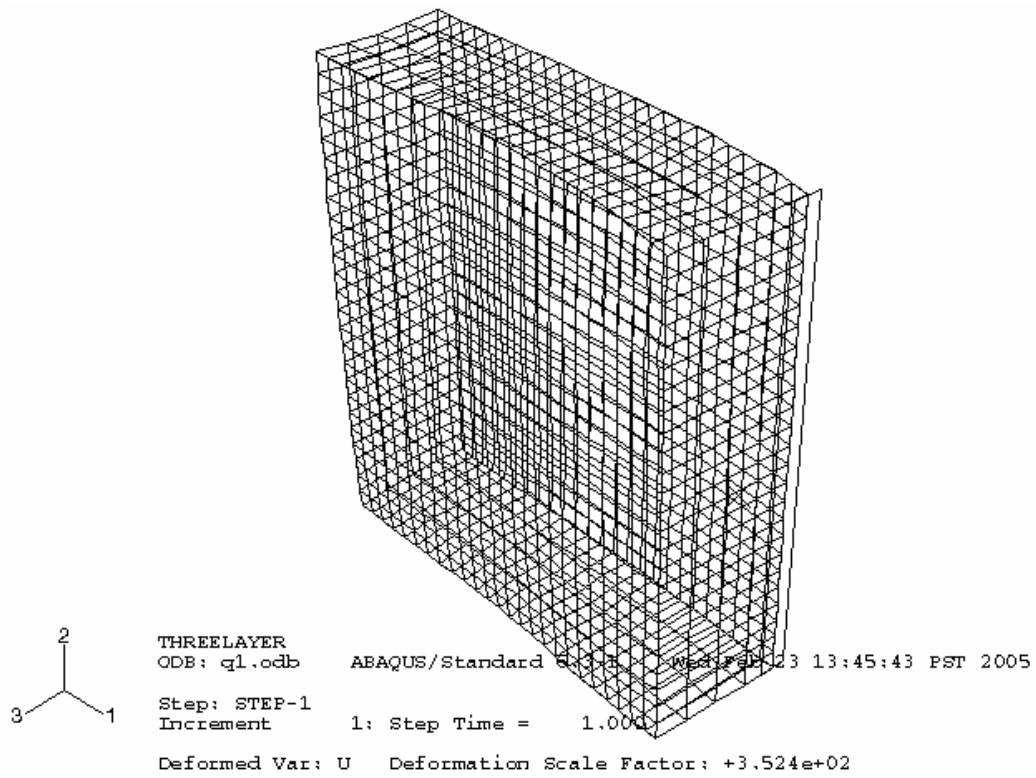


Figure 4-30 Deformed shape (S09)

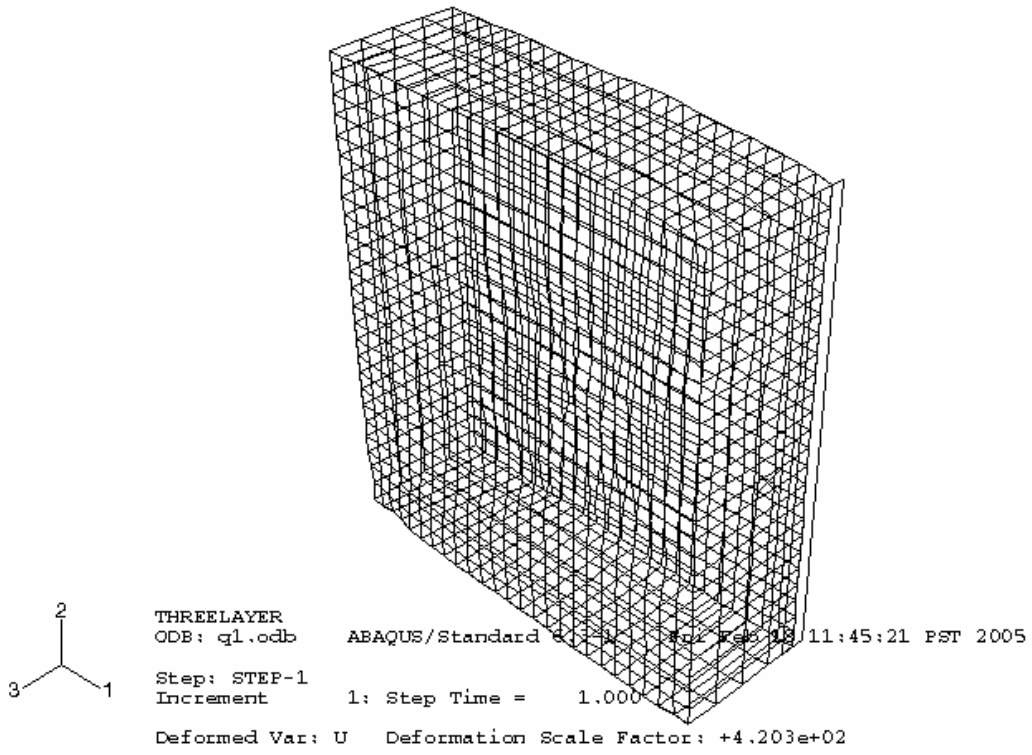


Figure 4-31 Deformed shape (S15)

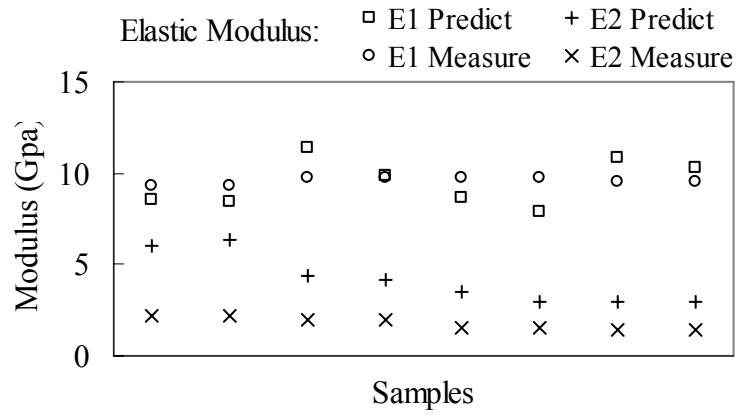


Figure 4-32 Overall Elastic modulus from prediction and measurement

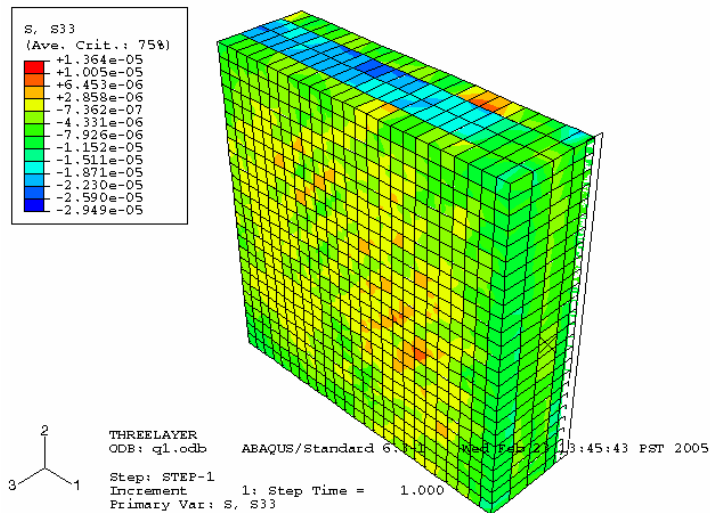
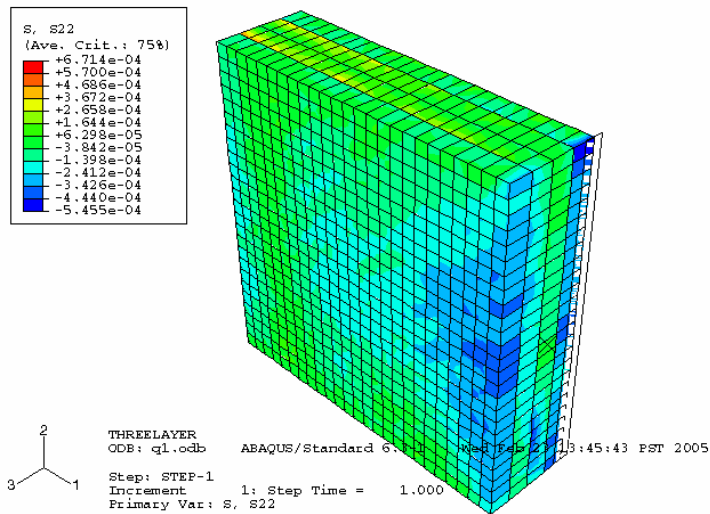
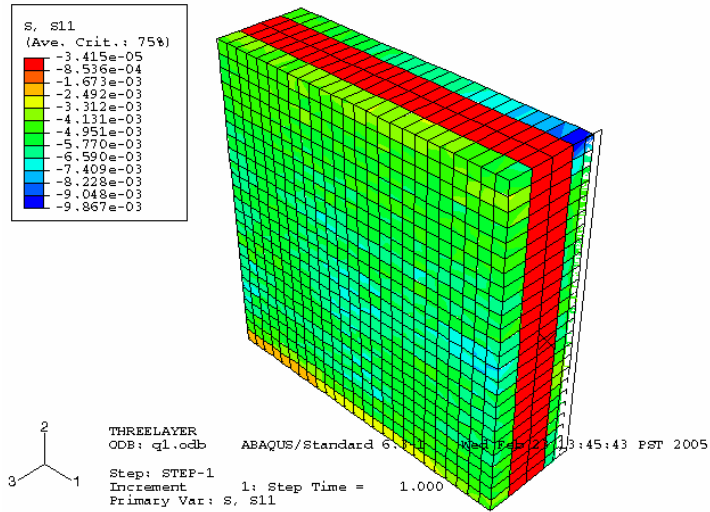


Figure 4-33 Stress distribution under uniaxial tension (S09)

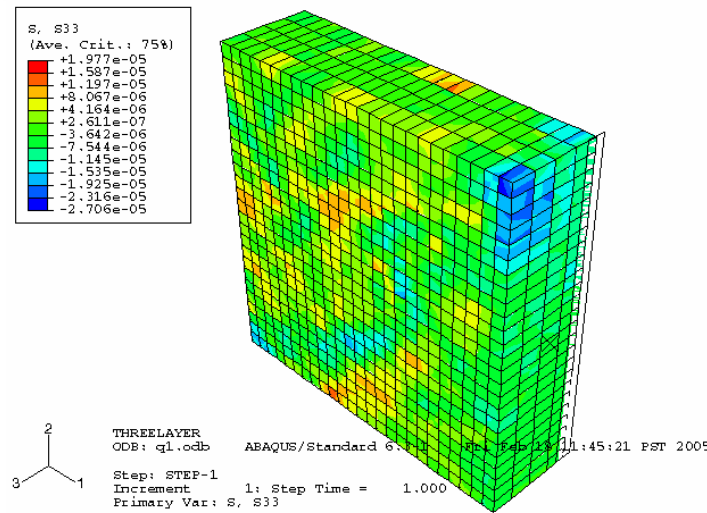
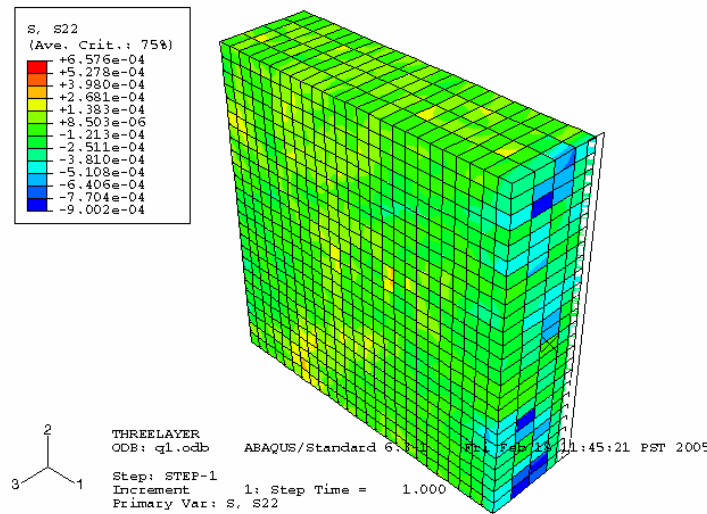
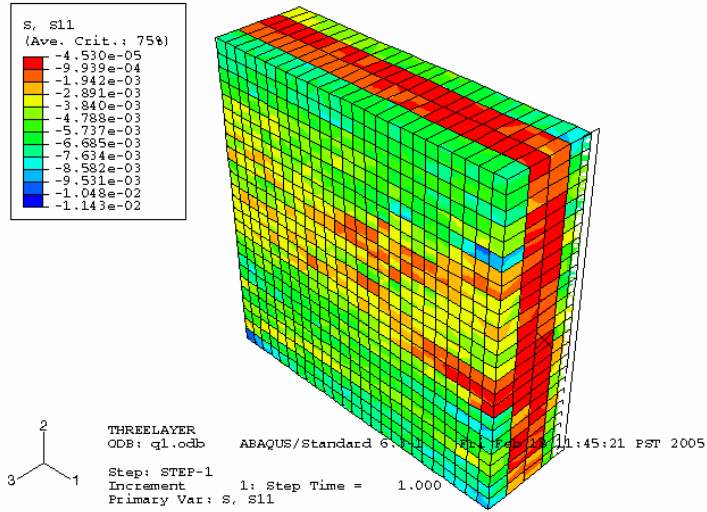


Figure 4-34 Stress distribution under uniaxial tension (S15)

## Chapter 5      Stress non-uniformity in indirect tensile test<sup>†</sup>

### 5.1 Introduction

Indirect Tensile (IDT) Test has been widely used to predict the fatigue performance of asphalt concrete. However the interpretation of the test is based on homogeneous elasticity. Historically the microstructure or the heterogeneity of the sample is not adequately reflected in detail for numerical simulation.

Various material models have been introduced to predict the behavior of asphalt concrete under both monotonic loading and cyclic loading. Schapery (1984) introduced a model by replacing physical strains with pseudo strains so that a viscoelastic problem can be transformed into an elastic problem through the correspondence principle. Work potential theory (Schapery, 1990) was used in constitutive and evolution description based on pseudo stresses and strains. The change of stiffness of the material due to accumulative damage or healing was also taken into account. Both monotonic loading and cyclic loading were investigated using this theory (Park *et al.*, 1996; Zhang *et al.*, 1997; Lee and Kim, 1998b; Lee and Kim, 1998a). Viscoplastic models were also introduced recently to describe the rate dependent plastic stress-strain relations of asphalt concrete. Collop *et al* (2003) implemented an elasto-viscoplastic constitutive model with damage for asphalt. It was formulated based on the generalized Burger's model: an elastic element in series with a viscoelastic element (linear Voigt) and a viscoplastic element (nonlinear). A power law function was assumed for the viscoplastic strain rate-stress relationship. Damage was accounted for by introducing parameters that modify the viscosity. Tashman *et al* (2005a) developed a microstructural viscoplastic continuum model for asphalt concrete. The viscoplastic strain rate was defined using Perzyna (1966a) flow rule and the linear Drucker-Prager yield function. The aggregate anisotropy was accounted for by introducing a microstructure tensor reflecting the orientation of non-spherical particles. Seibi *et al* (2001) used a Perzyna type viscoplastic constitutive model with isotropic hardening and Drucker-Prager yield criterion. Schwartz *et al* (Schwartz *et al.*, 2002) developed a model based on the extended viscoplastic Schapery continuum damage model. The model compared favorably with experimental measurements and it was concluded that the assumption of time-temperature superposition is valid for both viscoelastic and viscoplastic strain responses.

The literature indicates that asphalt concrete is controlled by viscoplastic response and dominated by plasticity that can be defined by Drucker-Prager criterion. However, these continuum models are based on homogeneous material properties derived from

---

<sup>†</sup> Excerpt reprinted from Zhang, B. *et al.* (2006) "An Evaluation of the Stress Non-uniformity due to the Heterogeneity of AC in the Indirect Tensile Test", ASCE Geotechnical Special Publication No. 146, pp.29-43, with permission from ASCE.

various experimental data on representative volumes or specimens. The microstructure is not considered in these models. In this study, the x-ray tomography technology was used to obtain the internal microstructure of the specimens. Image analysis method was developed to translate the acquired gray images into binary images to reconstruct the three dimensional (3D) microstructure that reflect the geometric configuration of voids, aggregates, and binder of the asphalt concrete specimens. This method can effectively reflect the discontinuous distribution of stresses, which is critical for damage incurrence.

This chapter compares the theoretical solution for the IDT test with Finite Element Method (FEM) simulations, and evaluates whether a parameter, the stress concentration factor (Wang, 2003) could capture the essential performance of asphalt concrete in terms of fatigue properties.

## **5.2 Methods**

### **5.2.1 X-ray tomography imaging, analysis and microstructure model**

X-ray Tomography is a valid tool for quantifying the microstructure of asphalt concrete (Wang *et al.*, 2001; Masad *et al.*, 2002; Wang *et al.*, 2004). In this study, the asphalt concrete sample was scanned using x-ray tomography to obtain a series of gray image slices that reflect density variation of the major constituents such as asphalt binder, aggregates and voids (Figure 5-1). Calibration was carried out according to the density of the material the size of the sample. It is very important to obtain good images in the scanning process so that accuracy can be established from the very beginning. When multiple slices are stacked together they created a 3D visualization of the internal structure of the specimen. Several computer codes, using IDL (Interactive Data Language), were written to carry out the 3D reconstruction and quantification (illustrated in Figure 5-2). Through image processing, the series of images were transformed into a 3D data array that can be mapped into FEM elements. Voids and aggregates were identified by setting proper thresholds in the data array. The threshold values play a critical role in this process. The proper threshold value can be obtained through comparison between image measurements and the actual void content and/or aggregate volume fractions. After identification of the material components, proper material properties (such as elastic modulus and Poisson's ratio) can be assigned to the corresponding components. A FORTRAN program was written to automatically generate the simulation model to implement this methodology. Three constituents namely asphalt binder, aggregates and voids with different material properties were considered in the simulation to account for the different mechanical properties of them. With this method, only the binder is considered as a rate and temperature dependent material. Its characterization is simpler and requires much less time and effort. A statistical study with elastic material model for small strains was conducted here to study the relative effect of mix properties on the performance of asphalt concrete and validate whether the simulation method can capture the essential data to represent performance.

### **5.2.2 Theoretical solution for indirect tensile test**

Due to the geometry of the specimen and the loading characteristics of IDT, the stress and strain in the specimen during loading are complicated. The simplified

theoretical solution for the plane stress condition along the horizontal and the vertical diameter is formulated as equations (5-1) and (5-2), respectively (Hondros, 1959a).

Along the horizontal diameter:

$$\sigma_{11} = \frac{2P}{\pi aL} \left[ \frac{\left(1 - \frac{x^2}{R^2}\right) \sin 2\alpha}{1 + 2\frac{x^2}{R^2} \cos 2\alpha + \frac{x^4}{R^4}} - \tan^{-1} \left( \frac{1 - \frac{x^2}{R^2}}{1 + \frac{x^2}{R^2}} \tan \alpha \right) \right]$$

$$\sigma_{22} = -\frac{2P}{\pi aL} \left[ \frac{\left(1 - \frac{x^2}{R^2}\right) \sin 2\alpha}{1 + 2\frac{x^2}{R^2} \cos 2\alpha + \frac{x^4}{R^4}} + \tan^{-1} \left( \frac{1 - \frac{x^2}{R^2}}{1 + \frac{x^2}{R^2}} \tan \alpha \right) \right]$$
(5-1)

Along the vertical diameter:

$$\sigma_{11} = \frac{2P}{\pi aL} \left[ \frac{\left(1 - \frac{y^2}{R^2}\right) \sin 2\alpha}{1 - 2\frac{y^2}{R^2} \cos 2\alpha + \frac{y^4}{R^4}} - \tan^{-1} \left( \frac{1 + \frac{y^2}{R^2}}{1 - \frac{y^2}{R^2}} \tan \alpha \right) \right]$$

$$\sigma_{22} = -\frac{2P}{\pi aL} \left[ \frac{\left(1 - \frac{y^2}{R^2}\right) \sin 2\alpha}{1 - 2\frac{y^2}{R^2} \cos 2\alpha + \frac{y^4}{R^4}} + \tan^{-1} \left( \frac{1 + \frac{y^2}{R^2}}{1 - \frac{y^2}{R^2}} \tan \alpha \right) \right]$$
(5-2)

where  $P$  is the magnitude of the applied force,  $a$  is the width of the loading plate,  $L$  and  $R$  are the length and radius of the cylinder, respectively, and  $\sigma_{11}$  and  $\sigma_{22}$  are the direct stresses in the horizontal and vertical directions, respectively.

The 3D solution was formulated with a potential function by (Wijk, 1978). However, it is more complicated and is close to the plane stress solution. The influence of the loading plate stiffness and geometry is in the vicinity of the plate only (Zhang, 1997). For our case, the thickness of the model was very small. Therefore the above equations were used to draw the stress distribution of the specimen for the purpose of comparison.

### 5.2.3 FEM model construction

A FEM model geometry (Figure 5-3) was built to reflect the actual microstructure of specimens from the WesTrack project (Epps *et al.*, 1997). By importing the three dimensional data obtained from image analysis and reconstruction, the elements representing aggregates and voids were grouped and separated from the elements representing binder or mastics. Element groups representing aggregates and asphalt binders were assigned different elastic material properties while the element group for voids was removed during the loading steps. In this study, all the non-voids components

were assigned elastic properties that may represent the behavior of the binder at low temperature and small loading magnitude. The result of the FEM simulation was compared with the analytical elastic solution to verify the accuracy of FEM simulation so that proper mesh size could be determined. Due to the large memory and disk space requirement of the simulation, all the images with 512×512 resolution were transformed into 100×100 resolution and the volume fractions of the constituents were maintained. In addition to stresses, strains, and displacements that result from the FEM simulation, the stress concentration factor (the ratio between the largest tensile stress and that of the elastic solution assuming homogeneity) was also computed. The stress concentration factor is a comprehensive indicator of the rationality of the material structure.

To validate these concepts, the three mixtures of the WesTrack project were evaluated using the procedure developed. In the WesTrack project, a single asphalt binder, PG 64-22, was used. There are three levels of aggregate gradation (fine, fine plus, and coarse) with single source of aggregates, three levels of asphalt content (%) (For fine and fine plus gradations: 4.7, 5.4 and 6.1, for coarse gradation: 5.0, 5.7 and 6.4), and three levels of air void content (4%, 8% and 12%). For the samples used in our study, the asphalt content is the optimum asphalt content determined with the Superpave Volumetric Design method (i.e. 5.4% for fine and fine plus mix and 5.7% for coarse mix). The air voids content is 8%. The fine plus gradation is formed by add extra fines into the fine gradation.

### 5.3 Results and discussions

Due to the existence of aggregates and voids in the mixture, the stress distribution no longer follows that of either the theoretical elastic solution or the FEM solution assuming homogeneity of the material.

The typical stress distributions along vertical and horizontal diameter for these three samples are plotted in Figure 5-4 through Figure 5-6. It can be seen that the coarse mix had the largest stress variations, followed by the fine plus mix and the fine mix. It should be noted that the performance of the mixes followed the same order (from poor to good).

The analytical solution for the IDT test model used in the FEM simulation was calculated and illustrated in Figure 5-7. While assigning the same property for aggregate and asphalt binder, the two-constituent FEM model yields a solution that agrees well with the analytical elastic solution in the average sense.

By comparing the stress distributions of the FEM simulations that include voids, aggregates and binder and those of the analytical solution, one can obtain the stress concentration factor conveniently. It is found that the fine mix sample had the least stress concentration while the coarse mix showed significantly larger stress concentration (See Figure 5-8). However, the stress concentrations are similar if voids were not removed, indicating the importance of void structure on the behavior of the mixture. The field performance indicates that the coarse mix had more fatigue cracking and it increases with the increase of the air voids (Kim *et al.*, 2002). The significant stress concentration observed in this study for coarse mixes may be the cause of large fatigue stresses that initiated microcracking in the pavement. In the calculation of the average stress (needed for calculating the stress concentration factor), the stresses along the 20mm and the 80 mm position (with a height of 60mm) were averaged to avoid the local effect in the

vicinity of the loading plate. The results are tabulated in Table 5-1. The result shows that the coarse mix has largest stress concentration that may lead to more fatigue cracking, which was observed in the field performance test.

The simulations are for thin disks. Generally, the stress distribution for all fine mix specimens (thin disks) is consistent. The same is true for the coarse mix specimens and the fine plus mix specimens, indicating that thin disks may be used for simulations to reduce memory and time requirements. In order to verify the statistical consistency of the simulations, simulations for ten different pieces were performed for each mixture. The average stress and its standard deviations were collected for every simulation. The results (Table 5-2 to Table 5-4) show that for every sample (a mix), the consistency is good and therefore the solutions were distinguishable among the three mixtures of the WesTrack project.

The variation of stress distribution due to the different ratios between the elastic modulus of aggregates and that of asphalt binder was also studied by comparing simulation results of samples with 1:1 ratio (aggregate modulus to binder or mastic modulus) up to 100:1 ratio. The results were plotted in Figure 5-9 for stresses along vertical and horizontal diameters respectively. It can be seen that large difference in constituent properties will lead to significant stress concentration even if there were no voids presented. This indicates that the relative stiffness between aggregates and the asphalt binder (or mastics) plays an important role in the mixture performance. It also implies that the damage may become more significant due to a softer binder or mastics. It should be noted that for the simulations with E ratio of 20:1 and 100:1, a more refined mesh might be needed to catch the accurate stress distribution and hence stress concentration.

## **5.4 Conclusions**

This chapter presents the generation of microscopic simulation model for IDT test configuration. The simulative test renders non-uniform stress and strain responses in the testing sample comparing with analytical solutions based on homogeneity. In the study, an evaluation of the stress distribution with and without consideration of voids indicated that voids induce significant non-uniform stress distribution. The modeling includes segmented sample simulations with statistically acceptable consistencies. The stress concentration varies significantly with the void distribution and the relative stiffness between aggregate and binder. We suggest that the IDT test should be combined with FEM simulation to offer better interpretation of the test results. The stress concentration factor may serve as a good simple performance indicator.

## **5.5 Acknowledgement**

This study is based upon work supported by the National Science Foundation under Partnership for Innovation Grant No. 0438480. Any opinions, findings, and conclusions or recommendations expressed in this material are those of the authors and do not necessarily reflect the views of the National Science Foundation.

Table 5-1 Stress concentration of the three WesTrack mixtures

Mixtures	Phases <sup>1</sup>	Average	Maximum	S.C.F. <sup>2</sup>
Fine	2	0.0363	0.0658	1.81
	3	0.0333	0.0728	2.18
Fine Plus	2	0.0337	0.0641	1.90
	3	0.0362	0.1985	5.48
Coarse	2	0.0313	0.0676	2.16
	3	0.0354	0.2144	6.05
Theoretical solution		0.0364	0.0375	1.03

<sup>1</sup> 2 phases: binder (with voids), aggregates

3 phases: aggregates, binder, voids

<sup>2</sup> Stress concentration factor

Table 5-2 Stress statistic study for the fine-mix sample

Segment	before void removal			after void removal		
	Average	Maximum	S.C.F.	Average	Maximum	S.C.F.
1	0.03638	0.06577	1.81	0.03499	0.06840	1.95
2	0.03591	0.04486	1.25	0.03108	0.04284	1.38
3	0.03647	0.05088	1.40	0.03236	0.07280	2.25
4	0.03738	0.06138	1.64	0.03077	0.05027	1.63
5	0.03639	0.06064	1.67	0.02723	0.04643	1.71
6	0.03715	0.05797	1.56	0.04224	0.07277	1.72
7	0.03665	0.05287	1.44	0.03879	0.05836	1.50
8	0.03590	0.06026	1.68	0.03510	0.06213	1.77
9	0.03493	0.05057	1.45	0.02866	0.04429	1.55
10	0.03576	0.06429	1.80	0.03200	0.05744	1.79
STDEV	0.07%	0.68%	18.24%	0.46%	1.14%	24.61%

Table 5-3 Stress statistic study for the fine-plus mix sample

Segment	Before void removal			After void removal		
	Average	Maximum	S.C.F.	Average	Maximum	S.C.F.
1	0.03519	0.05505	1.56	0.03931	0.07033	1.79
2	0.03331	0.05491	1.65	0.01387	0.03542	2.55
3	0.03452	0.05704	1.65	0.03694	0.08786	2.38
4	0.03328	0.06415	1.93	0.04403	0.16453	3.74
5	0.03161	0.05040	1.59	0.02370	0.12659	5.34
6	0.03287	0.05068	1.54	0.04236	0.10995	2.60
7	0.03365	0.05140	1.53	0.03826	0.19846	5.19
8	0.03327	0.05574	1.68	0.04221	0.10105	2.39
9	0.03532	0.05204	1.47	0.04277	0.12222	2.86
10	0.03403	0.05656	1.66	0.03864	0.10459	2.71
STDEV	0.11%	0.41%	12.51%	0.97%	4.58%	121.38%

Table 5-4 Stress statistic study for coarse-mix sample

Segment	before void removal			after void removal		
	Average	Maximum	S.C.F.	Average	Maximum	S.C.F.
1	0.03312	0.05041	1.52	0.04467	0.10635	2.38
2	0.03398	0.06763	1.99	0.03856	0.18578	4.82
3	0.03186	0.04622	1.45	0.02858	0.10865	3.80
4	0.03352	0.05181	1.55	0.03000	0.09078	3.03
5	0.03178	0.04507	1.42	0.02636	0.11865	4.50
6	0.03021	0.05118	1.69	0.03716	0.16080	4.33
7	0.02723	0.04594	1.69	0.04396	0.21444	4.88
8	0.03121	0.05546	1.78	0.03292	0.13823	4.20
9	0.03018	0.04060	1.35	0.03666	0.16088	4.39
10	0.02968	0.05724	1.93	0.03563	0.12001	3.37
STDEV	0.20%	0.77%	21.72%	0.61%	3.93%	81.57%

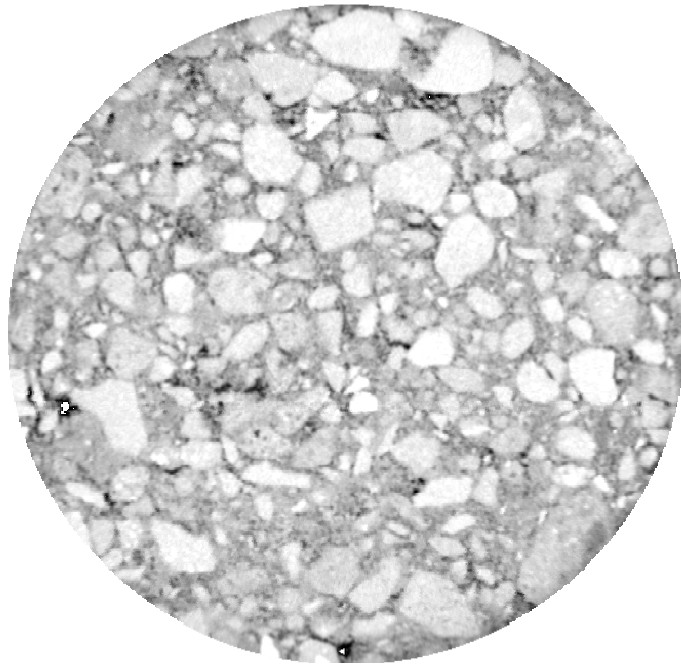


Figure 5-1 Gray image from x-ray scan

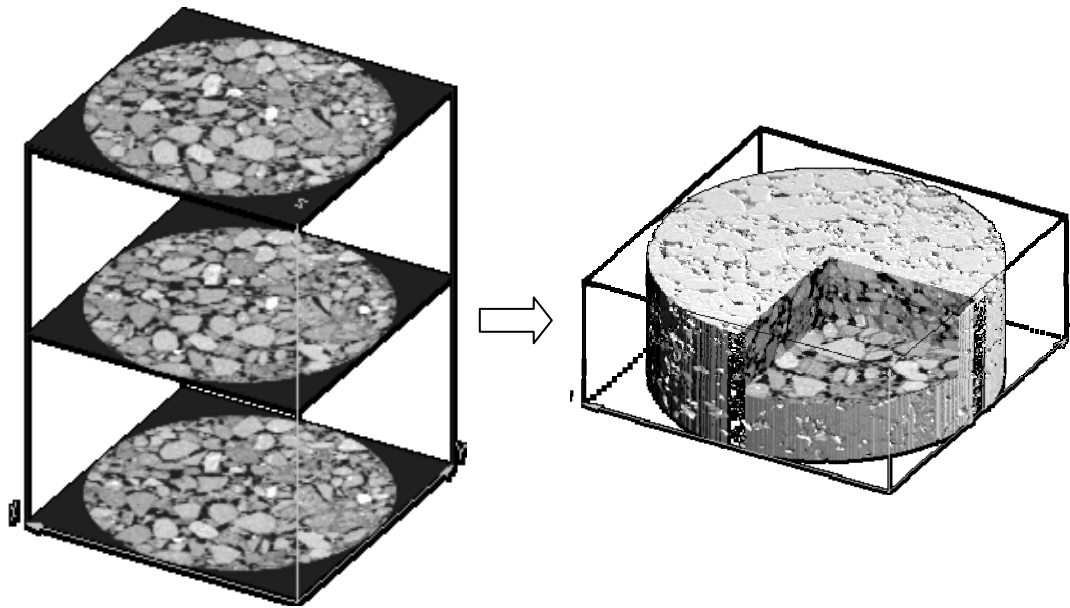


Figure 5-2 Three dimensional internal microstructure of a testing sample is reconstructed from series of x-ray tomography images. The phase configuration can be quantitatively determined with a data matrix that can be imported into finite element model.

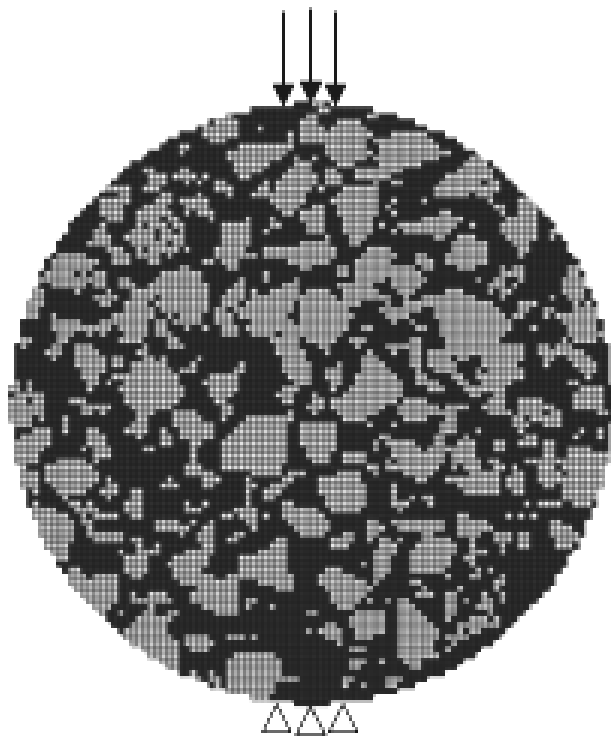


Figure 5-3 Three dimensional FE model

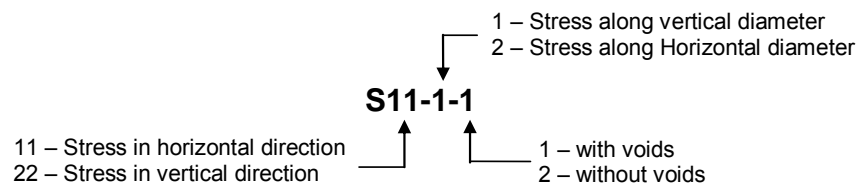
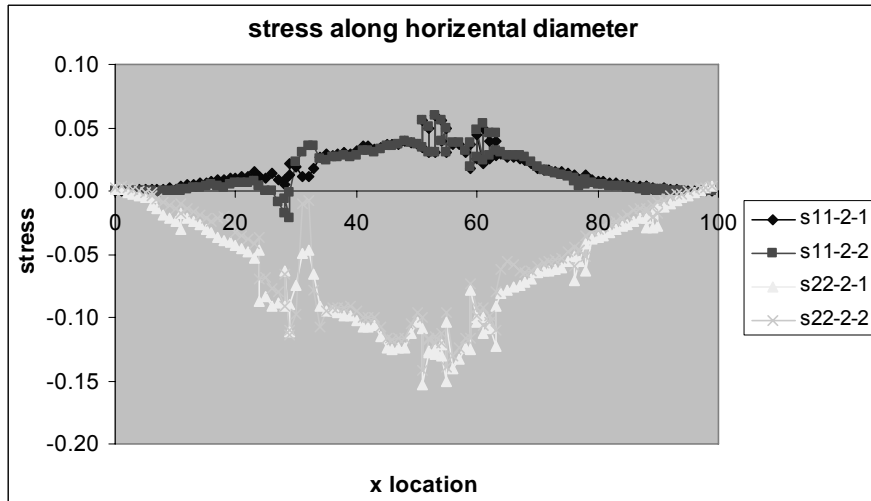
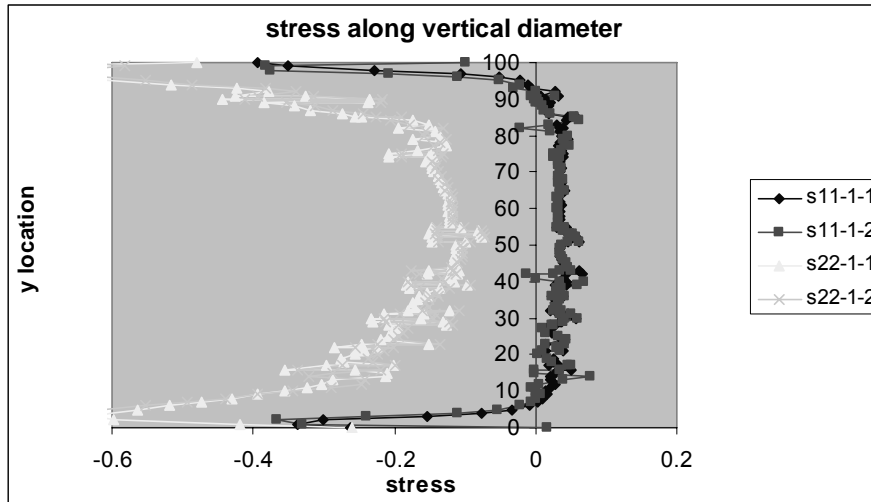


Figure 5-4 Stresses distribution for the fine-mix sample

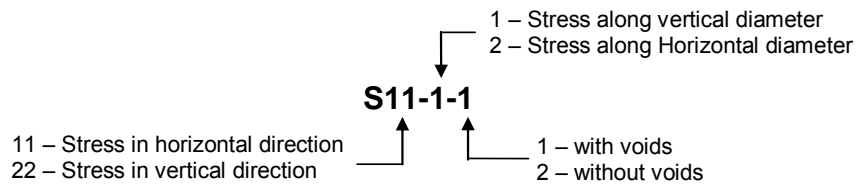
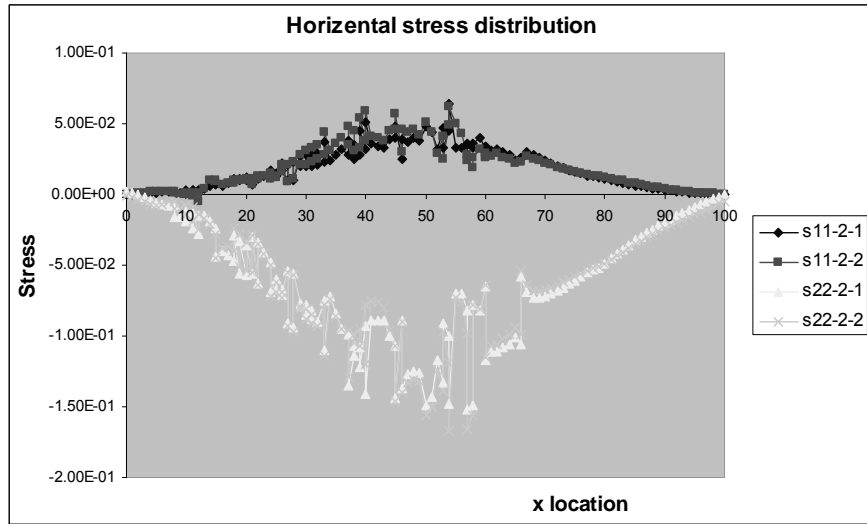
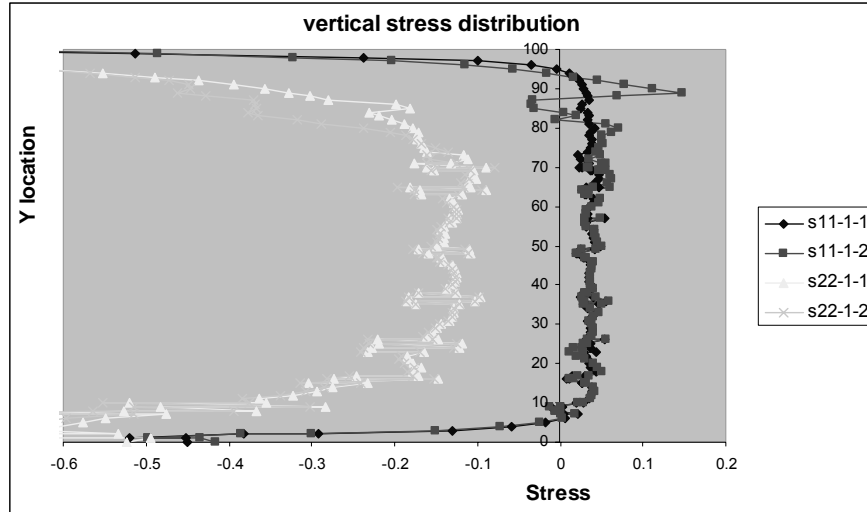


Figure 5-5      Stresses distribution for the fine-plus mix sample

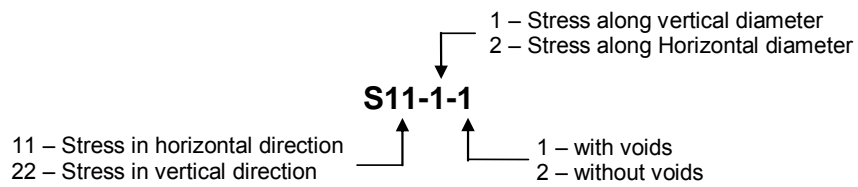
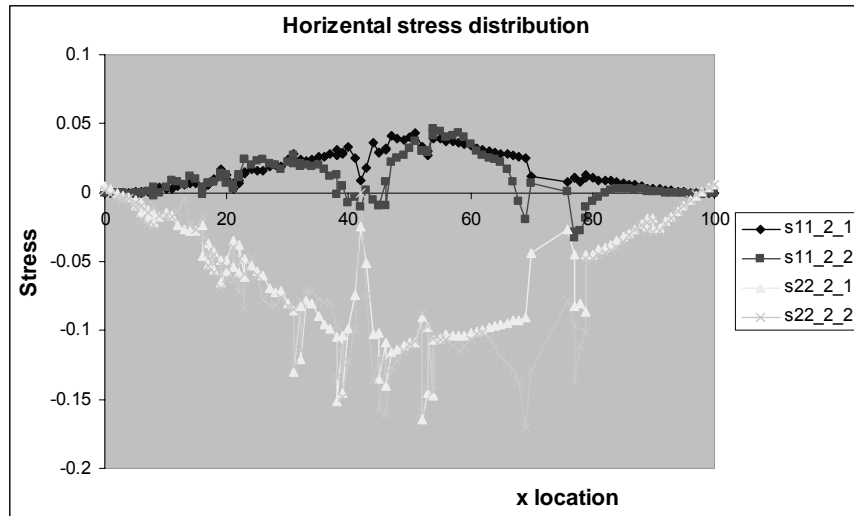
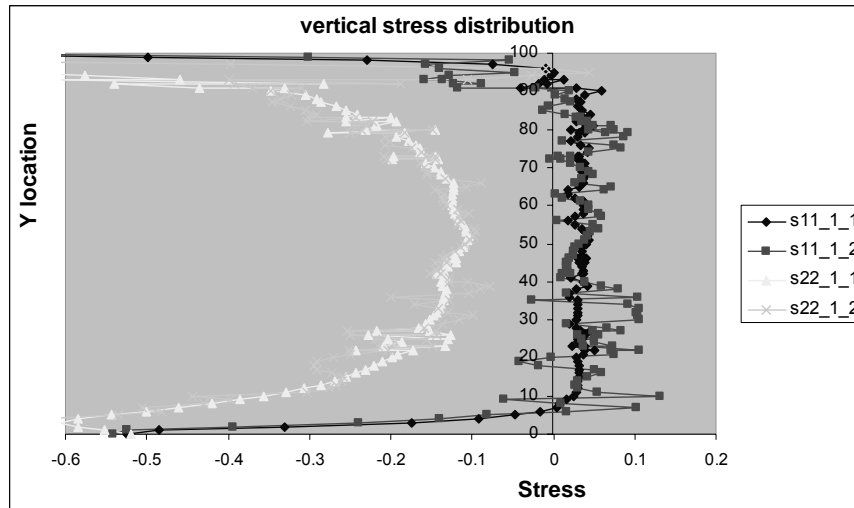
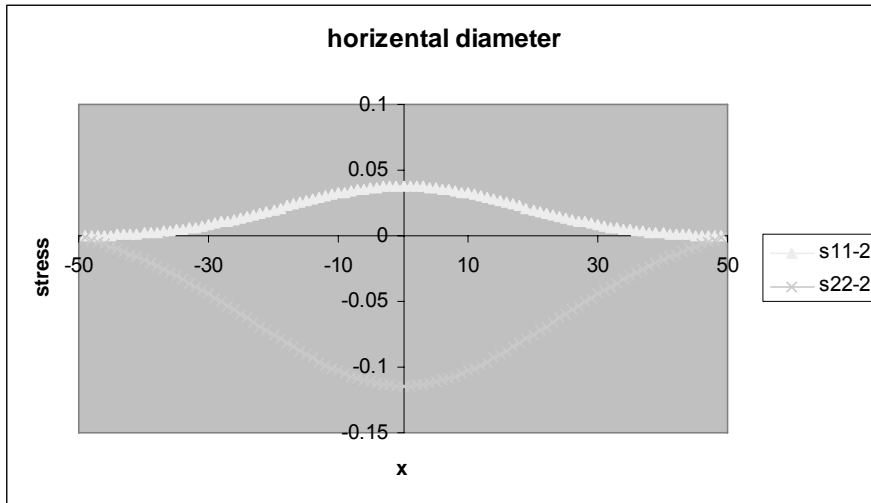
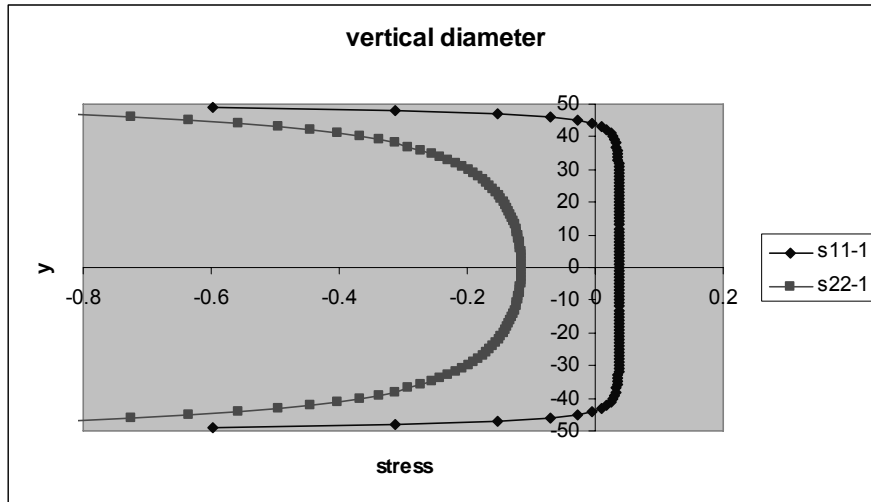


Figure 5-6 Stresses distribution for coarse-mix sample



1 – Stress along vertical diameter  
 2 – Stress along Horizontal diameter  
**S11-1-1**  
 11 – Stress in horizontal direction    1 – with voids  
 22 – Stress in vertical direction      2 – without voids

Figure 5-7 Stresses distribution along sample diameters (theoretical solution)

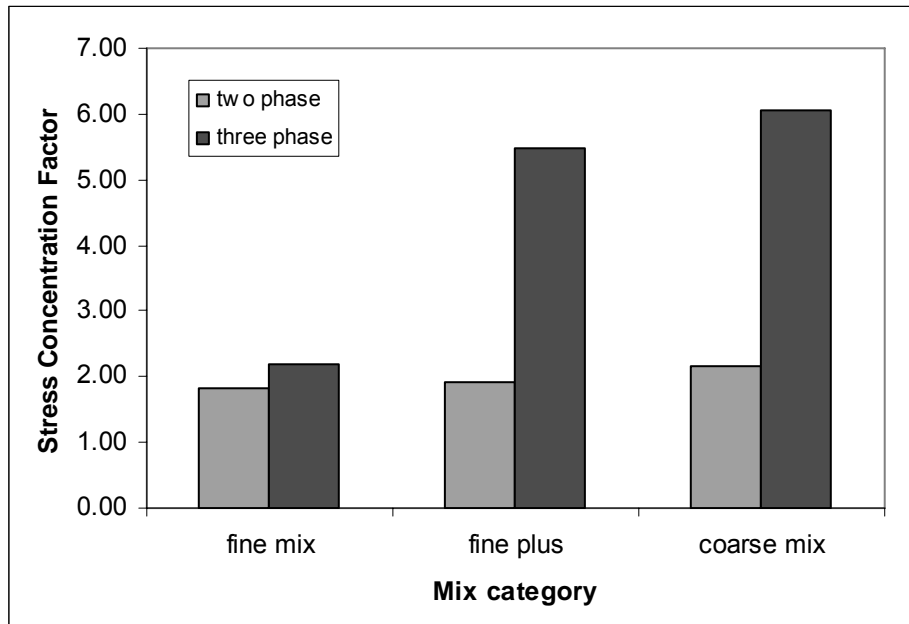
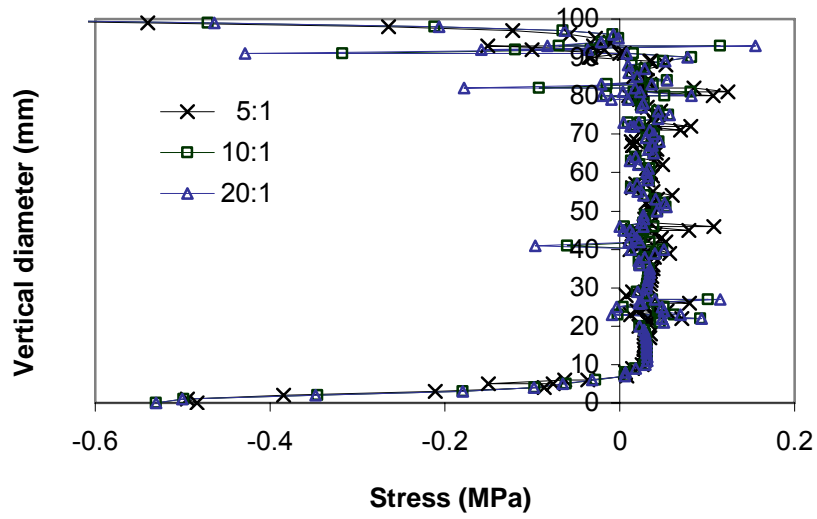


Figure 5-8 Stress concentration comparison



Note: s11 along vertical diameter with voids removed

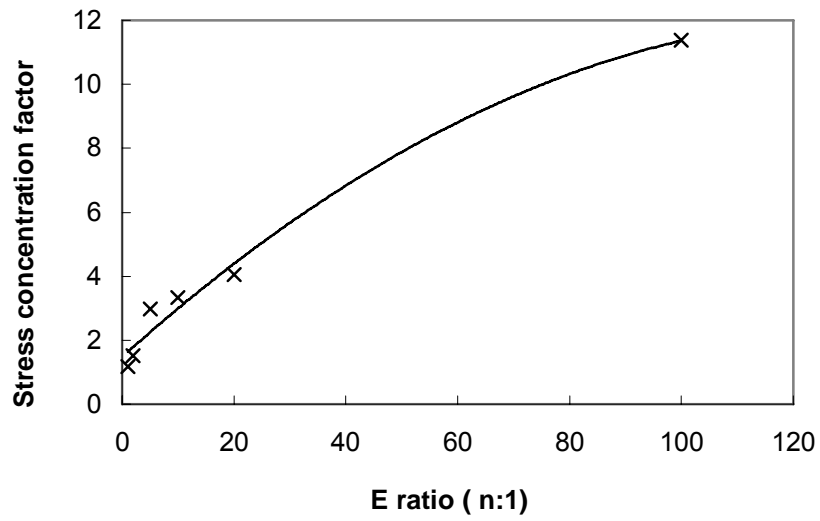


Figure 5-9 Stress distributions and stress concentration factors for different E ratios

## Chapter 6      **Viscoplastic parametric study of asphalt concrete**

### **6.1 Introduction**

Simple performance tests are used to characterize the viscoelastic material properties in pavement design. Indirect tensile test and dynamic modulus test are widely used to predict the mechanical properties of asphalt concrete in terms of resilient modulus, phase angle and dynamic modulus. In practice, the interpretation of the test is simplified using elasticity. For indirect tensile test, the simplified theoretical solutions for the plane stress condition along the horizontal and vertical diameters (Hondros, 1959b) are usually used to obtain stresses (Figure 6-1). This is mainly due to the complex geometry of the specimen and the difficulty of obtaining a theoretical solution for a viscoplastic material. For dynamic modulus test, uniaxial loading with uniform stress distribution is assumed to calculate stresses and strains in the sample. However, these will cause difficulties in understanding the fundamentals of material behavior.

Asphalt concrete mixture shows temperature and time dependency under loading. Viscoelastic (Schapery, 1984; 1990; Park *et al.*, 1996; Zhang *et al.*, 1997; Lee and Kim, 1998a) and viscoplastic (Perzyna, 1966a; Seibi *et al.*, 2001; Schwartz *et al.*, 2002; Collop *et al.*, 2003; Tashman *et al.*, 2005a) material models were introduced into study of asphalt concrete mixture. Besides these models based on strain decomposition, Kichenin *et al.* (1996) proposed a model with two-dissipative mechanisms, associating an elastic-viscous and an elastoplastic model in parallel. This stress overlay based model reflects the stress transfer between the two mechanisms and is suitable to describe materials consisting of multiple constituents. However, these continuum mechanics models have difficulties to capture the material behavior due to phase variations of different mix designs.

X-ray imaging based digital test was developed to take into account this material heterogeneity and stress nonuniformity (Zhang *et al.*, 2006). In order to study the viscoplastic material characteristics of asphalt mixture, a two-layer viscoplastic model was used to characterize the mixture behavior, serving as the basis for the numerical performance test. A macroscopic parametric study was conducted to obtain the sensitivity of each parameter to the deformation response of the sample. Finally, microscopic models for indirect tensile test and dynamic modulus test were built considering the viscous behavior of the asphalt binder or mastics and the phase configuration of the asphalt concrete mixture to build realistic digital specimen and digital tests that enables the characterization of mixture properties as well as properties of individual material.

In order to study the viscoplastic material characteristics of asphalt mixture, a two-layer viscoplastic model was used to characterize the mixture behavior, serving as

the basis for the numerical performance test. A macroscopic parametric study was conducted to obtain the sensitivity of each parameter to the deformation response of the sample. The sensitivity analysis will serve as a guide to calibrate the material model so that the simulation results can be matched with the actual test results. Finally, microscopic models for indirect tensile test and dynamic modulus test were built considering the viscous behavior of the asphalt binder or mastics and the phase configuration of the asphalt concrete mixture.

## 6.2 Theoretical elastic Solution

According to the simplified theoretical solution for the plane stress condition (Hondros, 1959b) along the horizontal and the vertical diameter, The stress distributions along the vertical and horizontal diameters are independent on material properties and they are plotted in Figure 6-1.

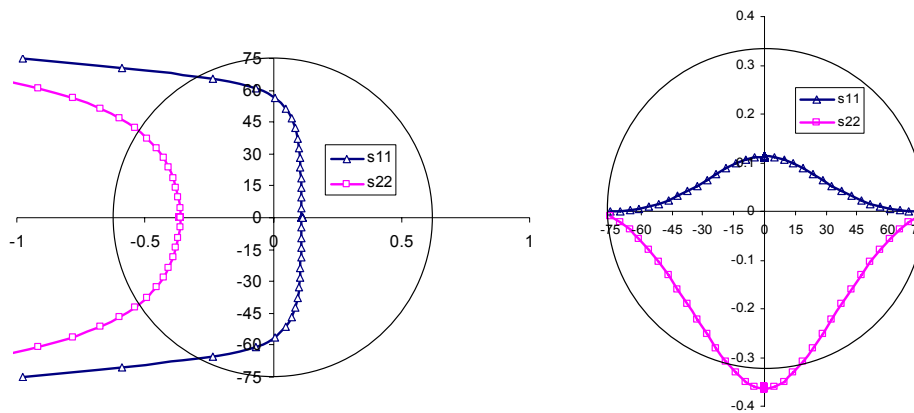


Figure 6-1 Elastic solution of stresses for IDT test

Based on the stresses obtained from this solution and the strains from the deformation measurement of the indirect tensile test (SHRP, 1993), the elastic modulus and Poisson's ratio can be derived. Zhang et al. (1997) extended the elastic solution to viscoelastic one and used the indirect tensile test to characterize viscoelastic material parameters. However, the viscoelastic solution still didn't account for the plastic contribution on the total strain response and only used the instantaneous and the recoverable part of the test results. In this part, the whole response of the testing will be used to characterize the viscoplastic material properties.

## 6.3 Macroscopic study – viscoplastic simulation

### 6.3.1 Finite element model

Macroscopic finite element models were built to simulate the indirect tensile test and dynamic modulus test.

### 6.3.1.1 Indirect tensile test

Finite element geometry models were built to reflect the actual displacement and traction boundary of the specimen. Due to the symmetrical geometry of the whole specimen, only a quarter of the sample was modeled with proper boundary conditions (Figure 6-2). The location of the displacement measurement point was determined according to actual testing configurations for a sample of six inch diameter.

In the actual indirect tensile test, the boundary is applied by loading strips. Since the modeling of loading strips will involve contact problems, which is very time-consuming in the simulation of repeated loading, the numerical model uses distributed traction force to represent the loading. This will have minimal effect on the results for homogeneous sample. At the symmetric axel, a roller support boundary is applied to each node (Figure 6-2).

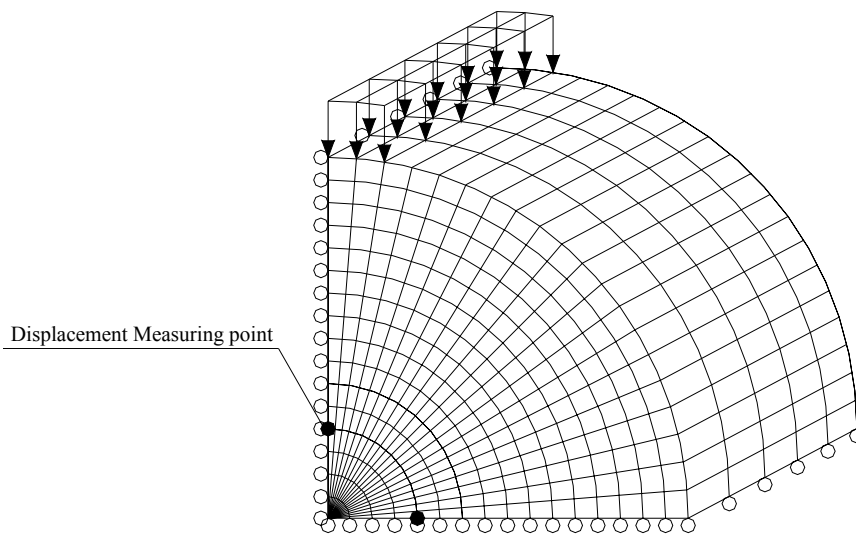


Figure 6-2 Geometry model of simulation IDT test

The loads are modeled as distributed boundary traction with repeated haversine pulse on a width of 3/8 inch for the entire thickness of the sample. The load amplitude and frequency were set to be the same magnitude and frequency as in the actual testing procedure (Figure 6-3).

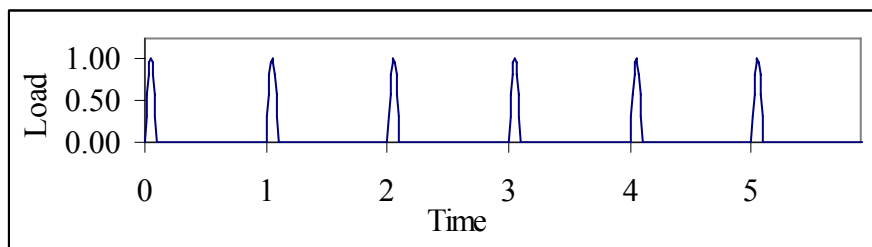


Figure 6-3 Indirect tensile test pulse loading

### 6.3.1.2 Dynamic modulus test

The simulation model of the dynamic modulus test is shown in Figure 6-4. Due to the axisymmetric configuration of the macroscopic model, a four node bilinear axisymmetric solid element with reduced integration and hourglass control was used.

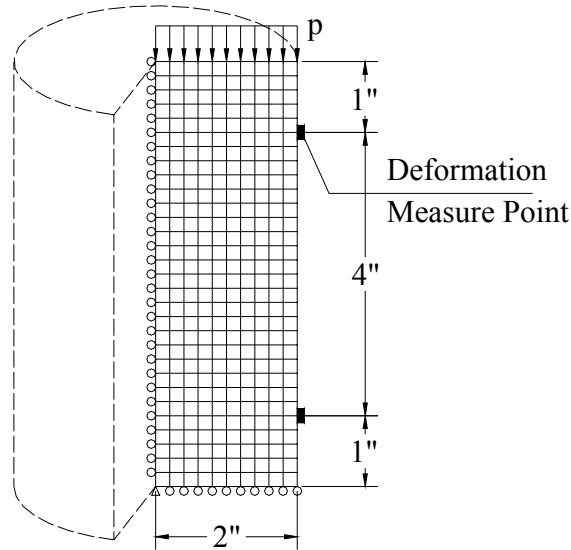


Figure 6-4 Finite element model for dynamic modulus test

Similar to the indirect tensile test, the surface traction was used as loading instead of loading plate to avoid the involvement of contact problem. The loads are modeled as distributed boundary traction with sinusoidal repetition (Figure 6-5) on the top edge of the sample.

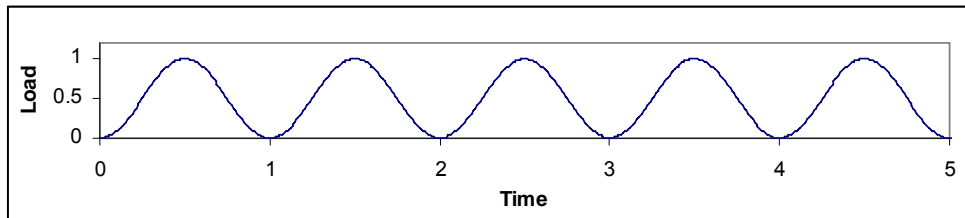


Figure 6-5 Dynamic modulus test sinusoidal loading

For both numerical tests, the accumulative deformation histories of the repeated loading simulation were recorded against loading time.

### 6.3.2 Material model

The stress overlay based two layer viscoplastic model (ABAQUS, 1995) was used to describe the constitutive relationship of the asphalt concrete mixture in the

macroscopic study and asphalt binder only in the microscopic study. The concept of this parallel network model is illustrated in Figure 6-6.

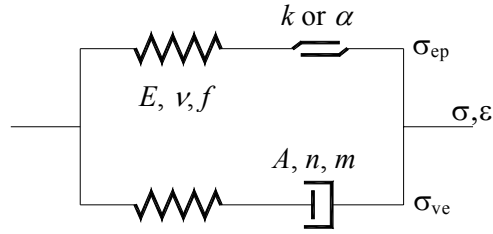


Figure 6-6 Two layer viscoplastic model

The total stress and strain in the networks can be expressed as in equations (6-1).

$$\begin{aligned}\sigma &= \sigma_{VE} + \sigma_{EP} \\ \varepsilon &= \varepsilon_{EP} = \varepsilon_{VE}\end{aligned}\quad (6-1)$$

where subscript  $VE$  represents the viscoelastic network and  $EP$  represents the elastoplastic network,  $f$  is the stiffness ratio of the viscoelastic network and is expressed as equation (6-2).

$$f = \frac{K_{VE}}{K_{EP} + K_{VE}} \quad (6-2)$$

where  $K$  is the instantaneous modulus. The von Mises type plasticity was used in the elastoplastic component. The flow rule is expressed in equations (6-3). The strain hardening type creep law was used. It is expressed as in equations (6-4).

$$\begin{aligned}\dot{\varepsilon}'_{ij} &= \frac{1}{2\mu} S_{ij} + \frac{1-2\nu}{E} \sigma_{ij} \delta_{ij} \\ \dot{\varepsilon}''_{ij} &= \dot{\varepsilon}^{pl} \cdot \frac{3}{2} \frac{S_{ij}}{q} \\ q &= \sqrt{\frac{3}{2} S_{ij} S_{ij}}\end{aligned}\quad (6-3)$$

$$\begin{aligned}\dot{\varepsilon}''_{ij} &= \dot{\varepsilon}^{cr} \cdot \frac{3}{2} \frac{S_{ij}}{q} \\ \dot{\varepsilon}^{cr} &= \left( Aq^n [(m+1)\bar{\varepsilon}^{cr}]^m \right)^{\frac{1}{m+1}} \\ q &= \sqrt{\frac{3}{2} S_{ij} S_{ij}}\end{aligned}\quad (6-4)$$

where  $\dot{\varepsilon}^{cr}$  is the uniaxial equivalent creep strain rate,  $\varepsilon^{cr}$  is the uniaxial equivalent creep strain,  $S_{ij}$  is the deviatoric stress tensor,  $q$  is the uniaxial equivalent deviatoric stress, and  $A, n, m$  are material constants.

There are seven parameters need to be calibrated. They are: elastic modulus  $E$ , Poisson's ratio  $\nu$ , modulus ratio  $f$ , viscous parameters  $A$ ,  $m$ ,  $n$ , and the initial yield stress  $\sigma_{yp}$ .

### 6.3.3 Numerical experiment

The simulation was conducted on the supercomputer at the high performance computing facility at Virginia Tech. The Inferno2 computing system uses parallel computing technology that provides high speed as well as large disk space and memory.

Simulations of the indirect tensile test have been done using the model in ABAQUS with the repeated half sine pulse loading and the accumulative deformation is obtained for each time increment. This historic deformation pattern will later be used together with the experimental counterpart to carry out parameter calibration.

The stress distributions along diameters are plotted in Figure 6-7. The stress distribution is almost the same for the elastic solution and the viscoplastic simulation. However, the total displacement is apparently different. Figure 6-8 shows the vertical displacement recorded along the vertical diameters for the elastic solution and the viscoplastic simulation. The total displacement response of the sample will be used to calculate the material parameters for the elastic, viscous and plastic components.

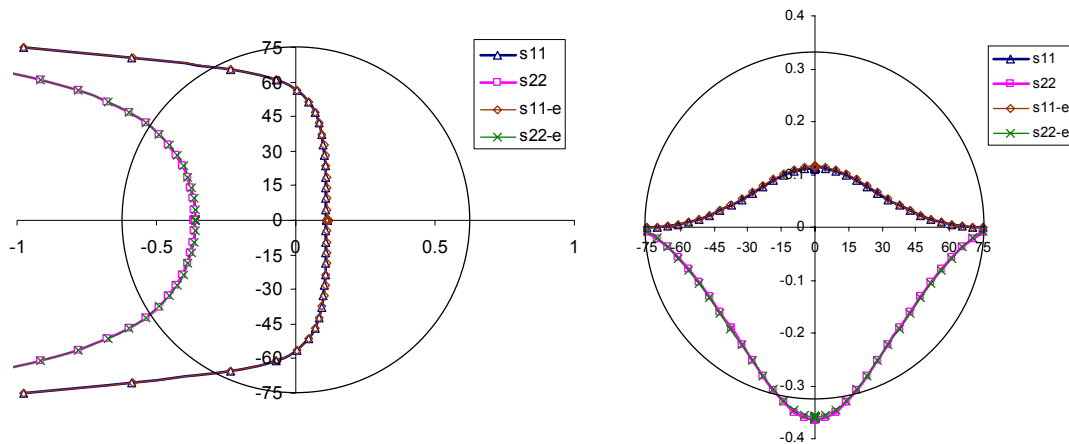


Figure 6-7 Stress distributions for elastic and viscoplastic solutions

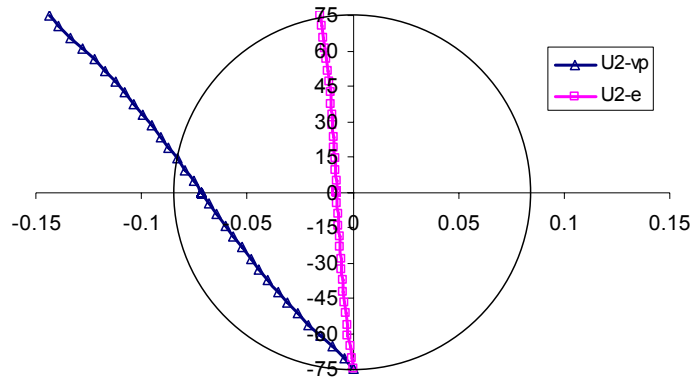


Figure 6-8 Displacement for elastic and viscoplastic solutions

### 6.3.4 Physical experiment

Some results of indirect tensile tests and dynamic modulus tests conducted in Virginia Tech Transportation Institute were used to compare with the simulation results. In the indirect tensile test, a controlled stress was applied and deformations along both the vertical diameter and the horizontal diameter were measured and recorded as historical outputs. These deformations were measured at the center sections of both diameters with the sector length of  $0.25D$  ( $D$  is the diameter of the sample). The setup of the test is illustrated in Figure 6-9. However, the test only recorded final part of the cumulative data, which made it difficult to use to characterize the model parameters. Due to this reason, the results of dynamic modulus test were used instead.

The test setting up for the dynamic modulus test is also illustrated in Figure 6-9. Measurement points are located four inches apart along the sample and three sets of them are mounted on each sample. Test results at  $5^{\circ}\text{C}$  and  $40^{\circ}\text{C}$  were used to back calculate material parameters for three-dimensional (3D) stress condition.

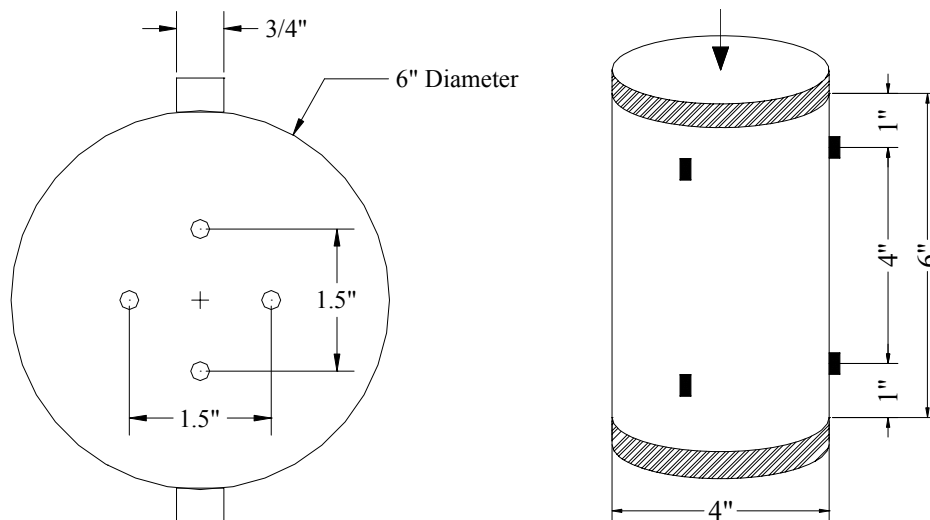
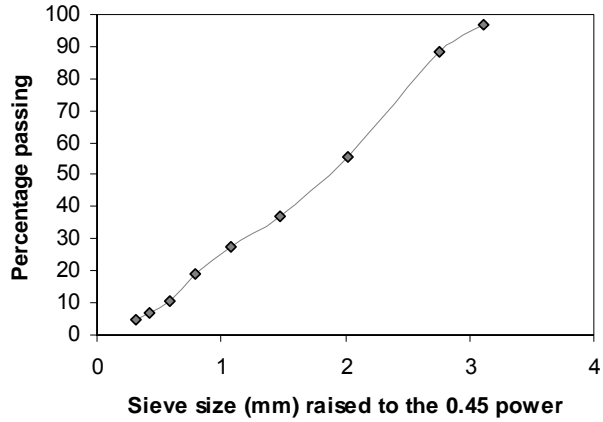


Figure 6-9 Illustration of setting ups for indirect tensile test and dynamic modulus test

For the mixture used in the comparison, the asphalt binder used is PG 64-22 with the asphalt content of 4.93%. The void in total mix is 6.5% and the aggregate gradation is shown in Table 6-1. The specific gravity of the sample is 2.458.

Table 6-1 Aggregate gradation for the sample used in the comparison

Sieve opening (mm)	% passing
12.5	96.6
9.5	88.6
4.75	55.6
2.36	37.3
1.18	27.6
0.6	19.2
0.3	10.8
0.15	6.7
0.075	4.9



### 6.3.5 Parameter back calculation

The parameters of the material model were obtained by back calculation using the simulation results and the testing data. The concept is to obtain a set of parameters that render closest deformation profile to the testing results (illustrated in Figure 6-10). In this study, the objective function is taken as equation (6-5).

$$\sum_{i=1}^N (\delta_i^m - \delta_i^p)^2 \quad (6-5)$$

where  $N$  is the number of time points for the deformation history,  $\delta_i^m$ ,  $\delta_i^p$  are measured and predicted final deflection values respectively. The instantaneous response was used to estimate the elastic modulus and the stiffness ratio between the two mechanisms.

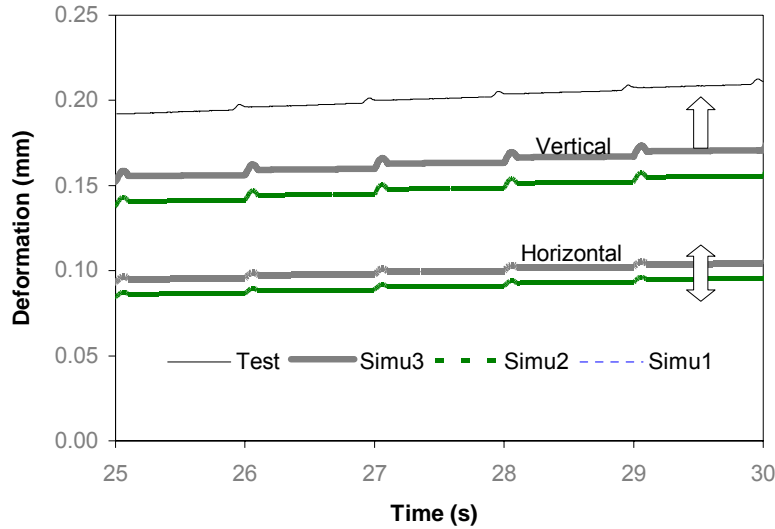


Figure 6-10 Illustration of the process of parameter adjustment

A sensitivity analysis for each independent material parameter was conducted before the optimization. The sensitivity is an input of the estimation process. The following steps were taken in the calibration procedure.

First, initial simulation profile was obtained with a set of parameters that are typical values for asphalt concrete mixture. Second, sensitivity analysis of each parameter was conducted to find the effect of each parameter to the simulation results. Finally, series of simulations were carried out to obtain the set of parameters leading to the minimization of the objective function.

#### 6.3.5.1 Sensitivity analysis

There are seven parameters in the two layer viscoplastic model used in this study. However, in order to simplify the procedure, some of the parameters that have less sensitivity were fixed at typical values. Poisson's ratio is taken as 0.3 for both networks and linear hardening was assumed for the elastoplastic network. This reduces the number of parameters to six.

For the indirect tensile test, the elastic modulus and the stiffness ratio of the viscous part can be obtained from the instantaneous response of the deformation profile. The effect of each parameter on the deformation profile is plotted in Figure 6-11 through Figure 6-16. The effect of each parameter on the final deformation is plotted in Figure 6-17 and the percentage change of the deformation caused by 10% change of each individual parameter is calculated and listed in Table 6-2. The elastic modulus and the stiffness ratio not only affect the instantaneous part of the response, but also the permanent deformation. They should be adjusted with the long term response profile. Other parameters mainly affect the plastic part of the response. Among them, the parameter  $A$ ,  $m$  and  $\sigma_{yp}$  have major effects on the permanent deformation profile.

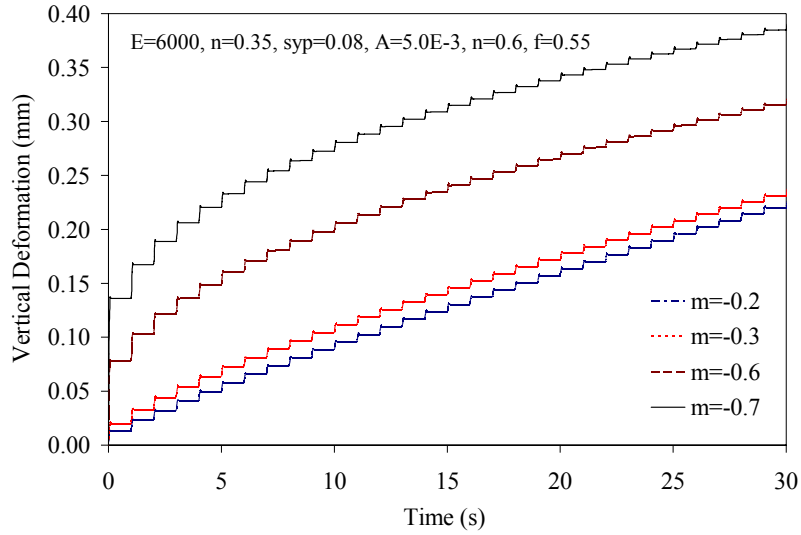


Figure 6-11 Sensitivity of parameter  $m$  on the deformation profile in IDT simulation with haversine pulse loading

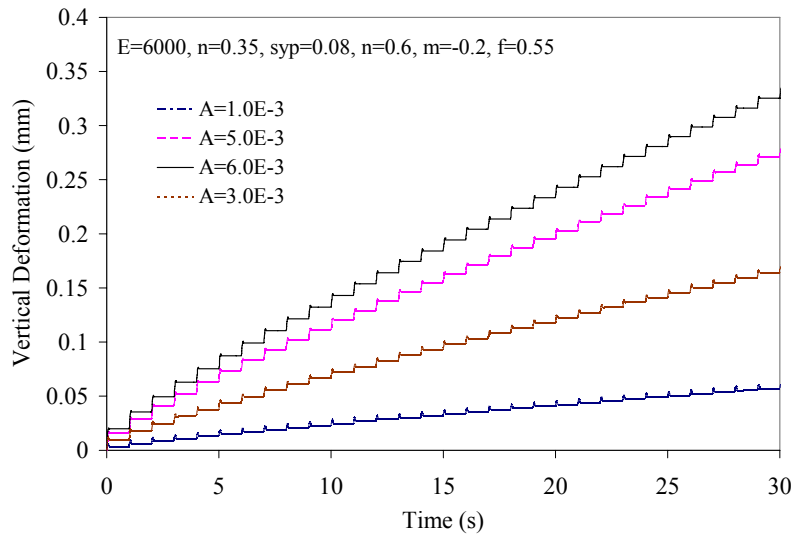


Figure 6-12 Sensitivity of parameter  $A$  on the deformation profile in IDT simulation with haversine pulse loading

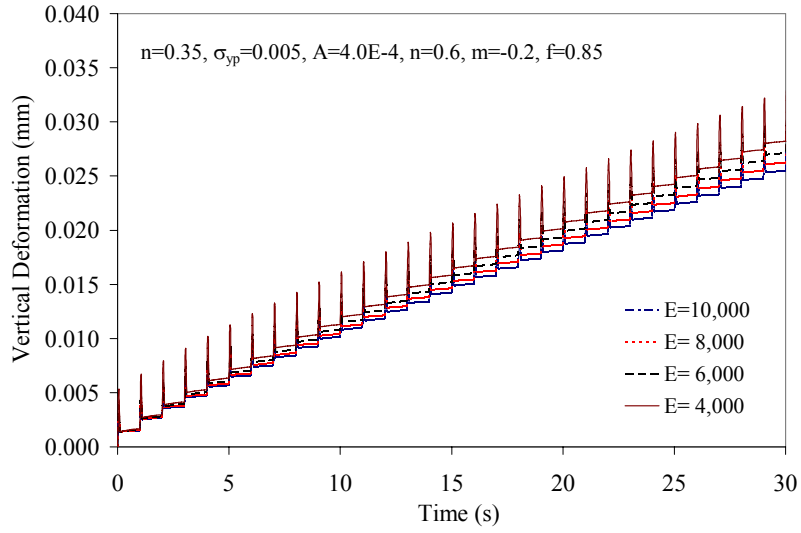


Figure 6-13 Sensitivity of parameter E on the deformation profile in IDT simulation with haversine pulse loading

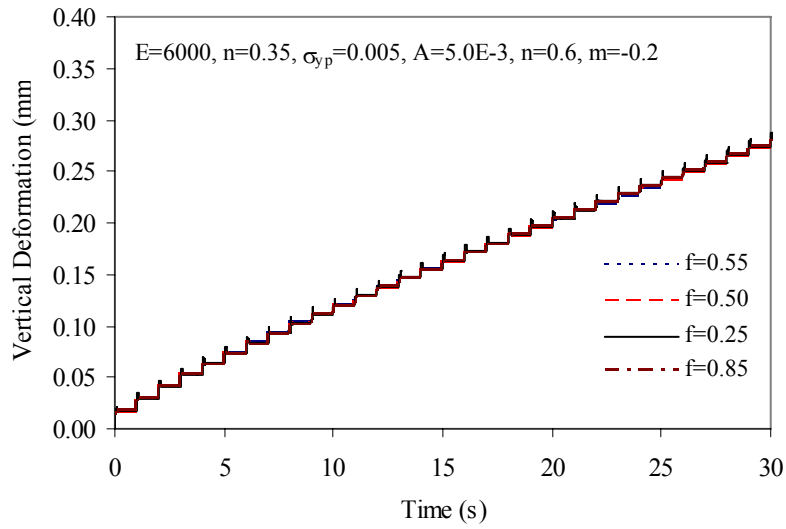


Figure 6-14 Sensitivity of parameter f on the deformation profile in IDT simulation with haversine pulse loading

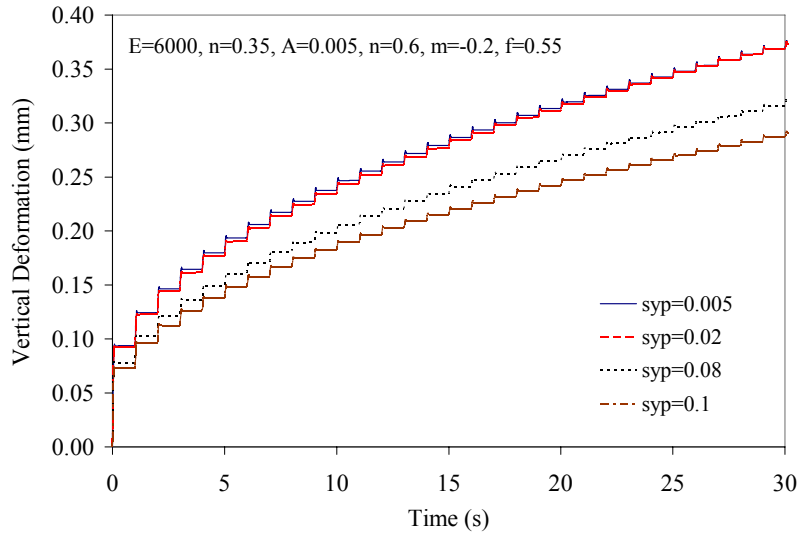


Figure 6-15 Sensitivity of parameter  $\sigma_{yp}$  on the deformation profile in IDT simulation with haversine pulse loading

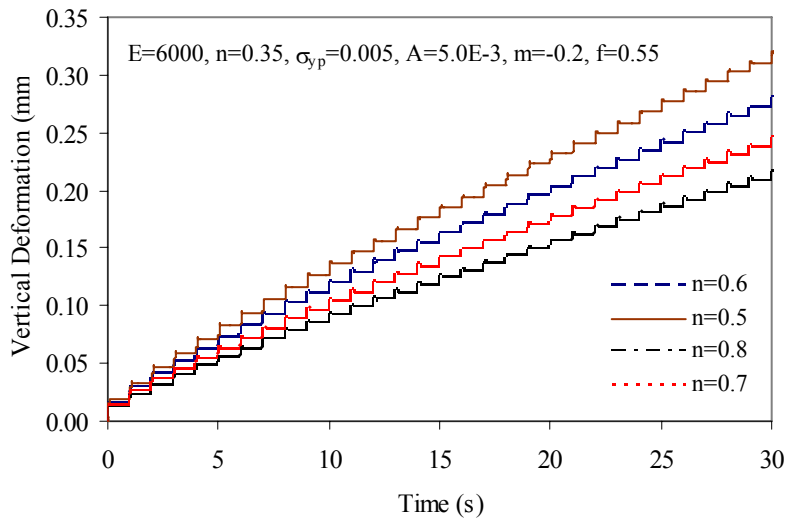


Figure 6-16 Sensitivity of parameter  $n$  on the deformation profile in IDT simulation with haversine pulse loading

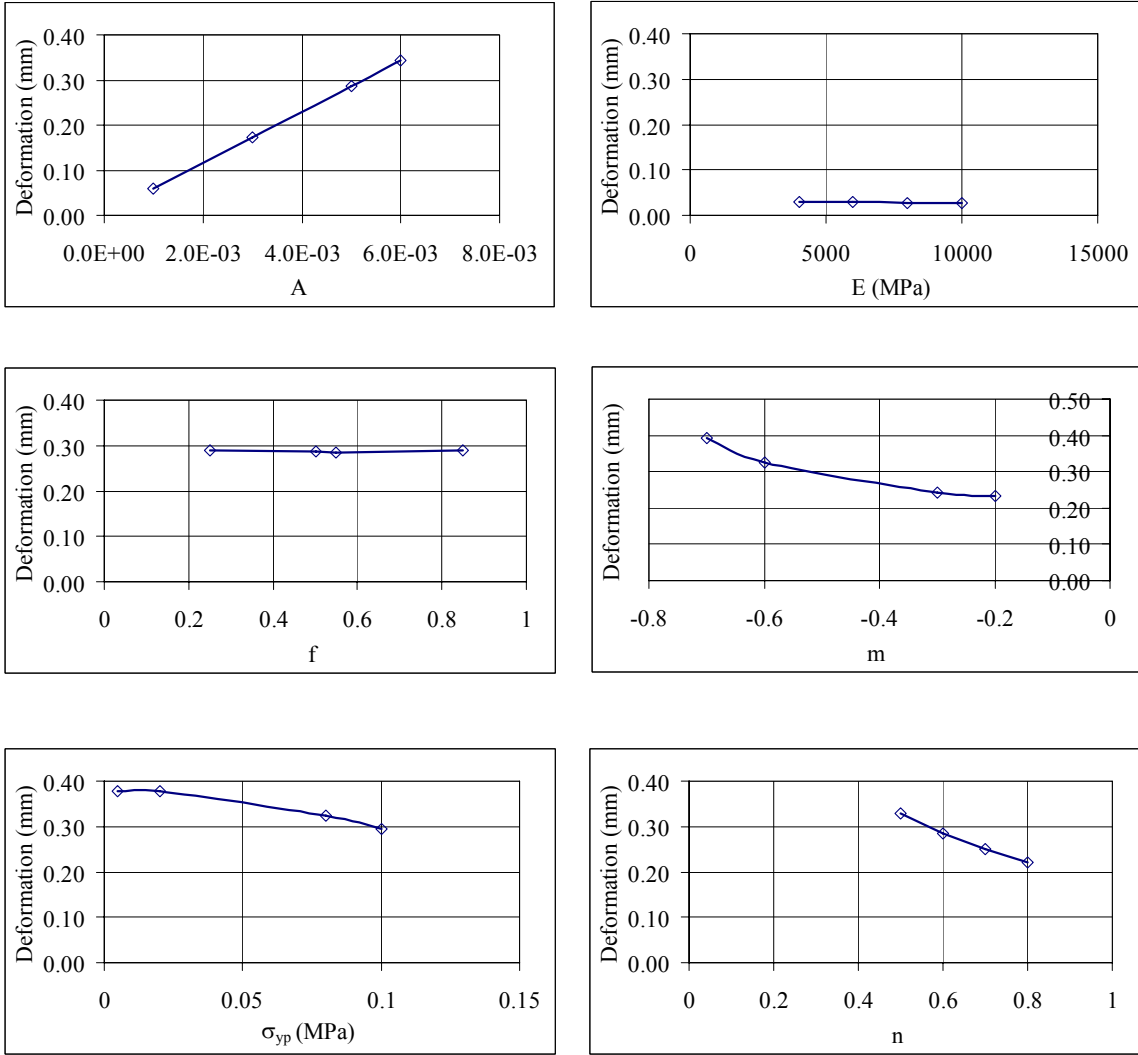


Figure 6-17 Parameter sensitivity to deformation profile

Table 6-2 Percentage change of deformation caused by 10% change of parameters

Model Parameters	Initial Values	Average Percentage Change of deformation from 10%
$E$ (MPa)	6000	1.06%
$\nu$	0.35	
$\sigma_{yp}$ (MPa)	0.08	0.04%
$A$	0.005	9.76%
$f$	0.55	0.28%
$m$	-0.2	3.41%
$n$	0.6	3.60%

The sensitivity study is also performed with the macroscopic simulation model for the dynamic modulus test configuration. The sensitivity of each parameter to the deformation profile is recorded and presented in Figure 6-18 to Figure 6-21. The effect of each parameter on the final deformation is plotted in Figure 6-22. It can be seen that all the viscous and plastic part parameters only affects the permanent deformation profiles, i.e. the general trend of the curve, except for parameter  $f$ , which is the ratio of the elastic stiffness for the two mechanism networks. It affects the instantaneous response of the simulation through setting the relative stiffness between the two networks.

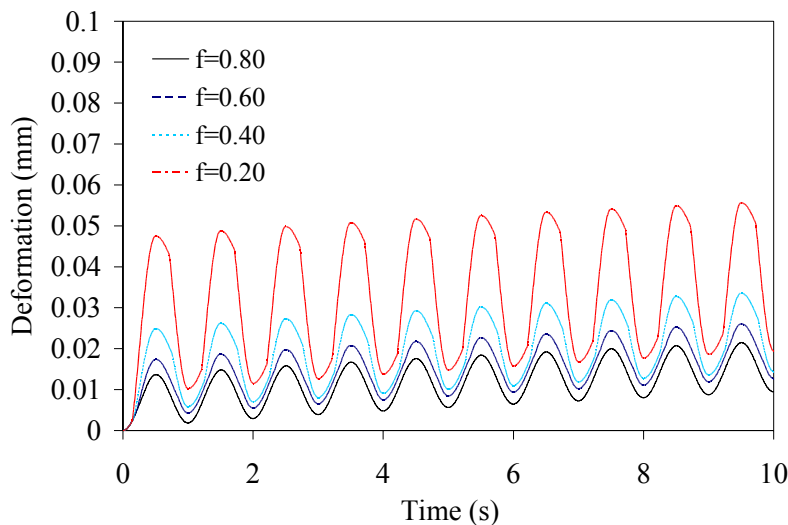


Figure 6-18 Sensitivity of parameter  $f$  on the deformation profile in dynamic modulus test simulation with haversine pulse loading

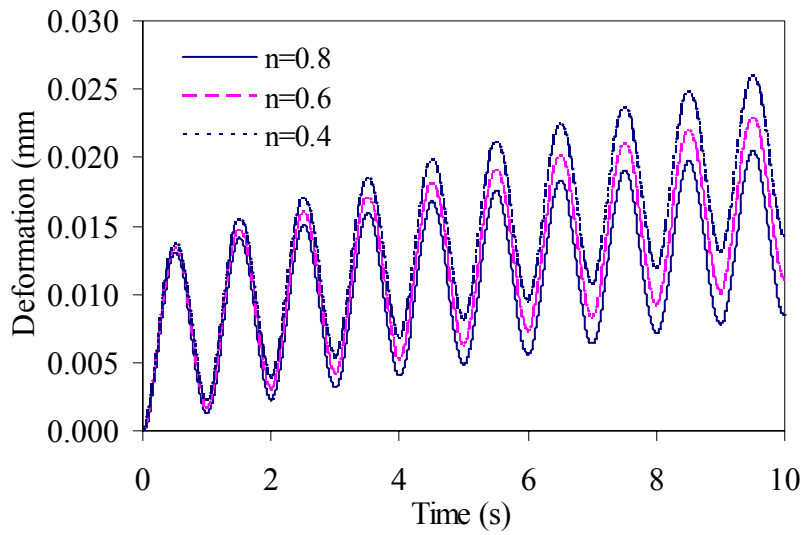


Figure 6-19 Sensitivity of parameter  $n$  on the deformation profile in dynamic modulus test simulation with haversine pulse loading

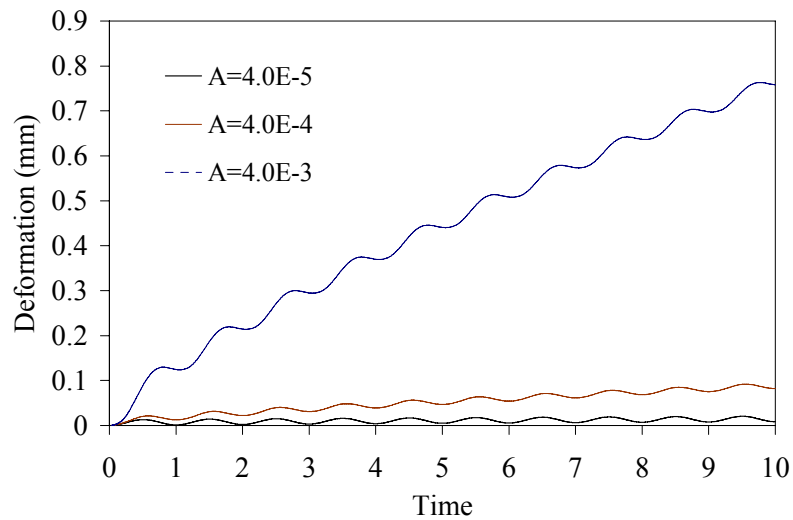


Figure 6-20 Sensitivity of parameter  $A$  on the deformation profile in dynamic modulus test simulation with haversine pulse loading

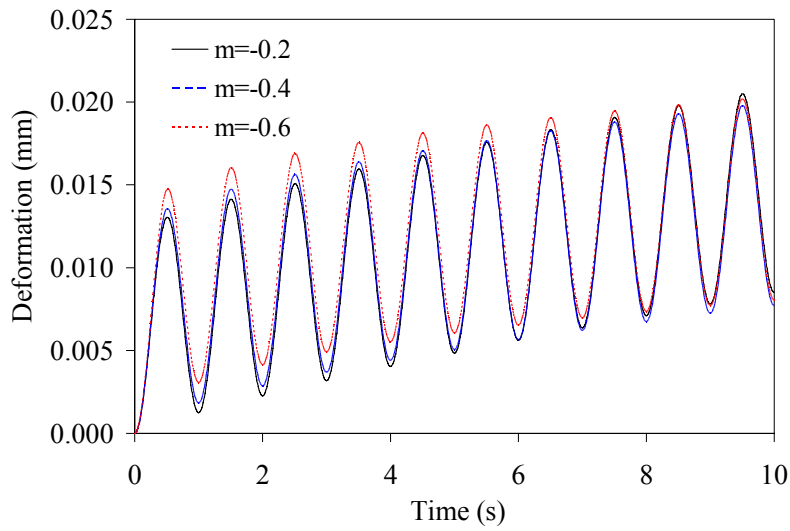


Figure 6-21 Sensitivity of parameter  $m$  on the deformation profile in dynamic modulus test simulation with haversine pulse loading

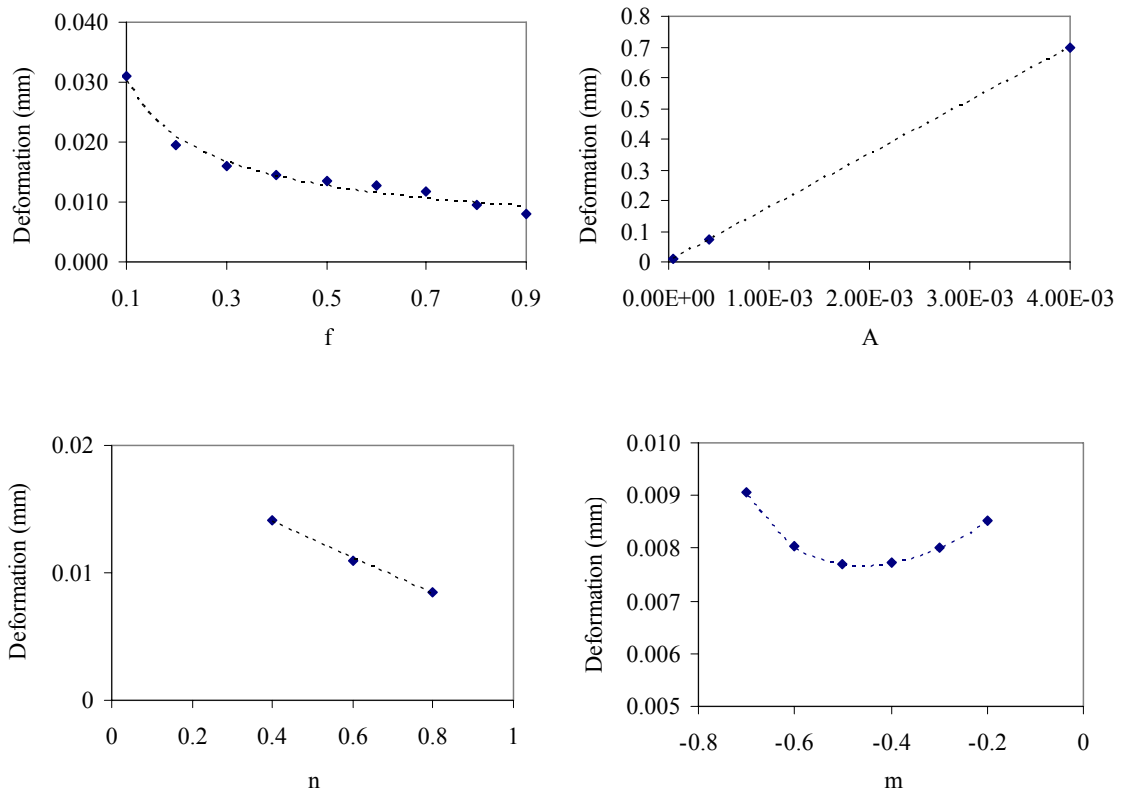


Figure 6-22 Parameter sensitivity to deformation profile in dynamic modulus simulation, the deformation is for permanent value after 10 cycles

### 6.3.5.2 Parameter back calculation

The simulation deformation profile and the actual testing records are usually in the manner as Figure 6-10 or Figure 6-23 and Figure 6-24. The material parameters were adjusted following the back calculation process based on the sensitivity analysis results. The optimized parameters for dynamic modulus testing results are listed in Table 6-3. By using these optimized parameters in the material model, the simulation results and the testing results are plotted together against time in Figure 6-23 and Figure 6-24. The temperatures of the testing are 5°C and 40°C, respectively.

Table 6-3 Optimized material parameters used simulation

Parameters	5°C	40°C
E (N/mm <sup>2</sup> )	30,000	4,100
$\nu$	0.3	0.35
$\sigma_y$ (N/mm <sup>2</sup> )	0.08	0.08
$\sigma_u$ (N/mm <sup>2</sup> )	0.8	0.8
$\varepsilon_u$	0.6	0.6
A	1.0E-06	4.0E-05
n	0.8	0.8
m	-0.2	-0.2
f	0.85	0.85

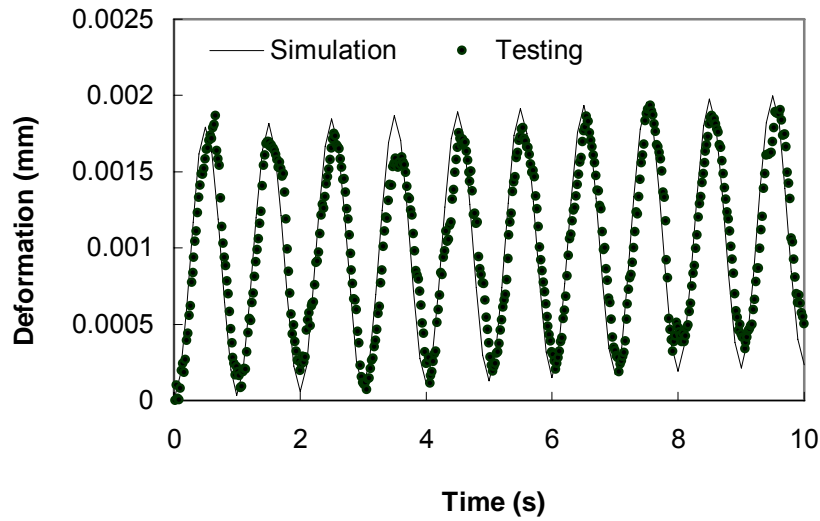


Figure 6-23 Simulation and experimental result at 5°C for macroscopic dynamic modulus testing, an actual test with 1Hz frequency was used

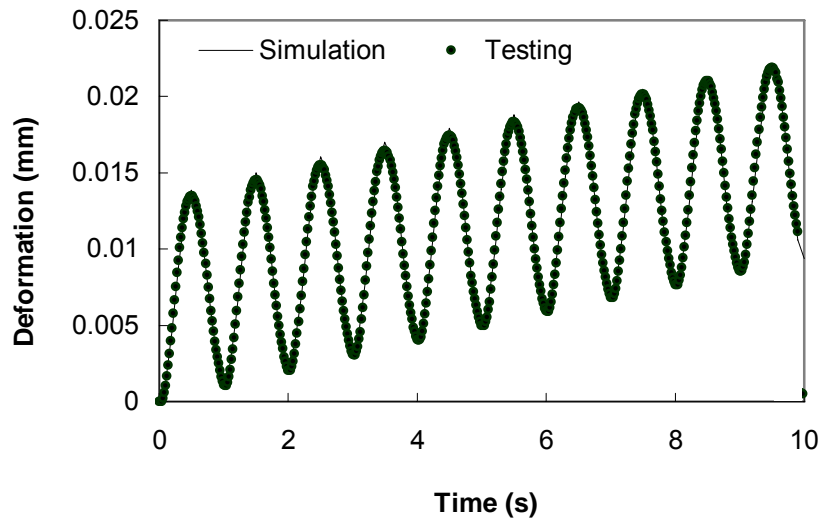


Figure 6-24 Simulation and experimental result at 40°C for macroscopic dynamic modulus testing, an actual test with 1Hz frequency was used.

Furthermore, from both deformation and loading profiles, we can get dynamic modulus and phase angle for a specified mixture. Figure 6-25 shows the steady state deformation and loading profiles with variation of the value of parameter  $m$ . It can be observed from deformation curves in the sensitivity study for all parameters that the magnitude of the curve remains almost the same while the profile trends have significant changes. This may imply that only parameters of the elastic part will considerably affect

the estimation of the dynamic modulus while those of viscous and plastic parts have major effect on the phase angle.

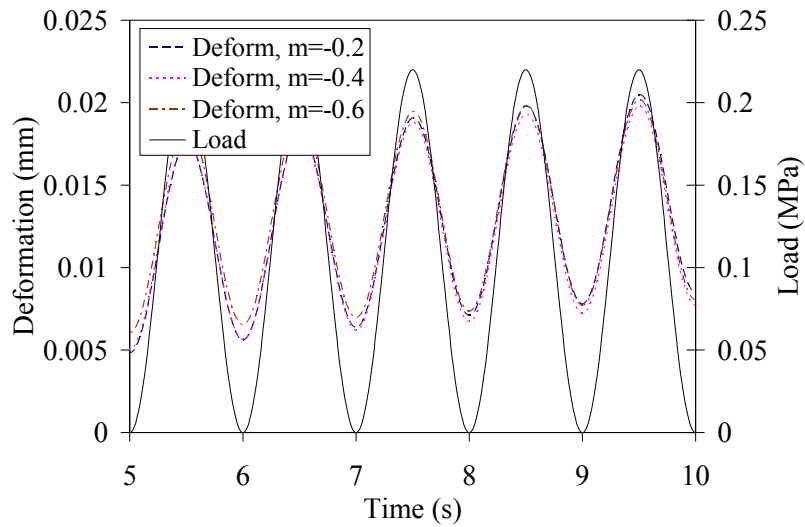


Figure 6-25 Steady state deformation profiles for parameter  $m$  ( $-1.0 < m < 0$ ), plot shows both load and deformation profiles than can be used to obtain the dynamic modulus

Figure 6-26 to Figure 6-29 show the effects of parameters  $A$ ,  $m$ ,  $n$  and  $f$  on the phase angle. Among them, parameter  $A$  has the largest effect.

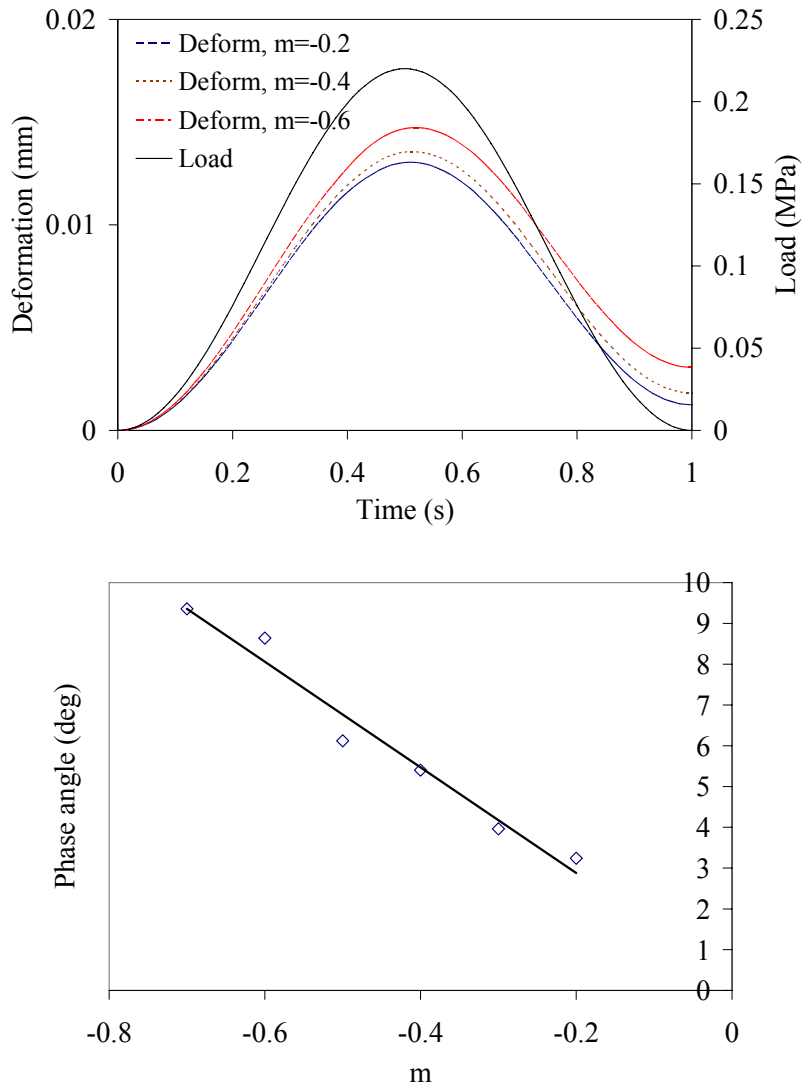


Figure 6-26 Effect of parameter m on the phase angle for numerical dynamic modulus test

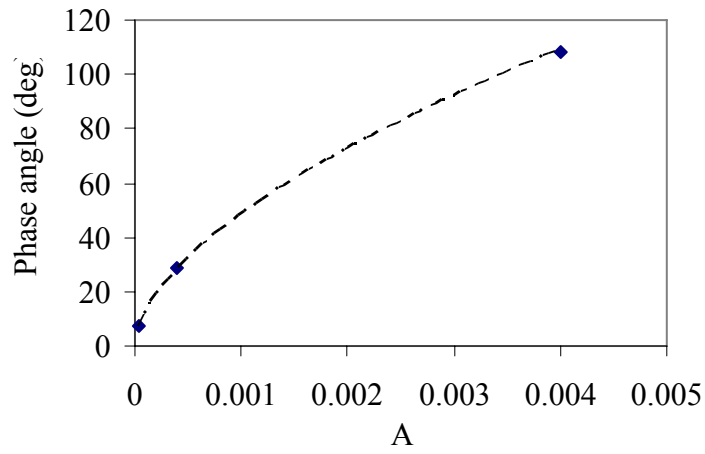
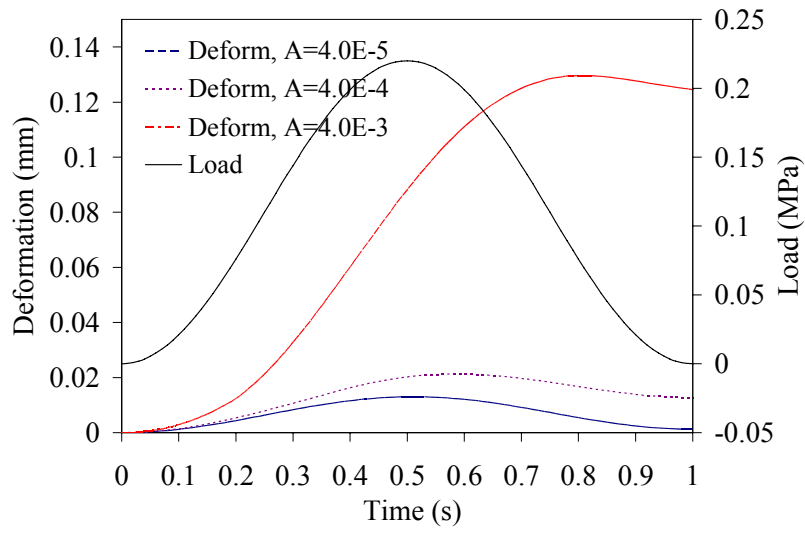


Figure 6-27 Effect of parameter A on the phase angle for numerical dynamic modulus test

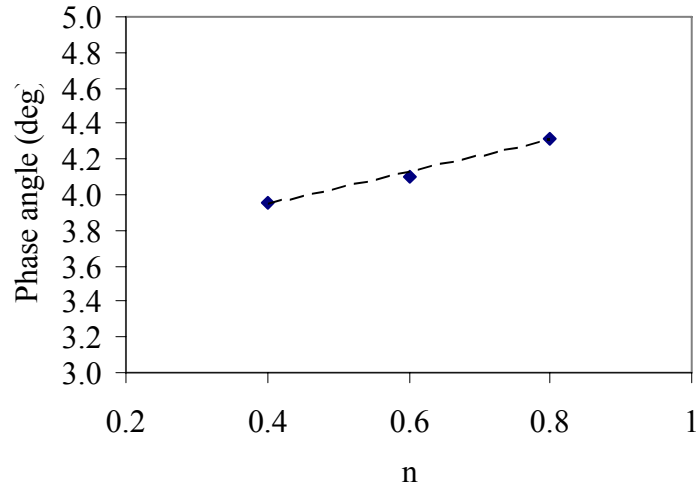
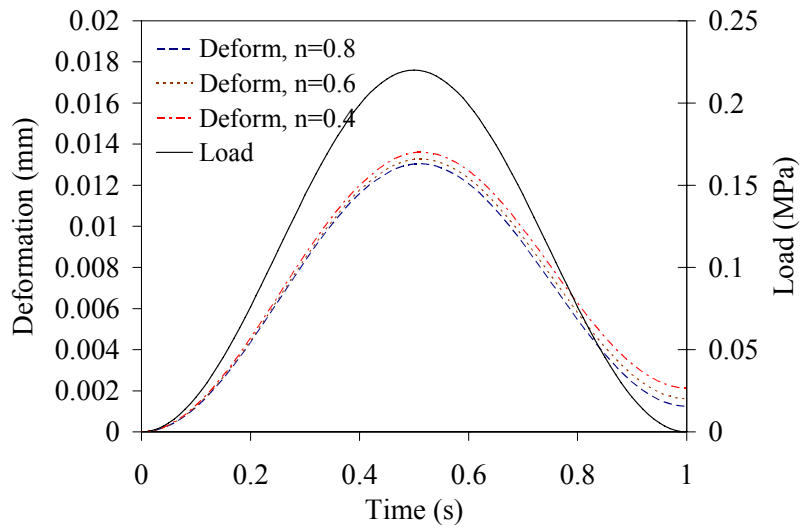


Figure 6-28 Effect of parameter  $n$  on the phase angle for numerical dynamic modulus test

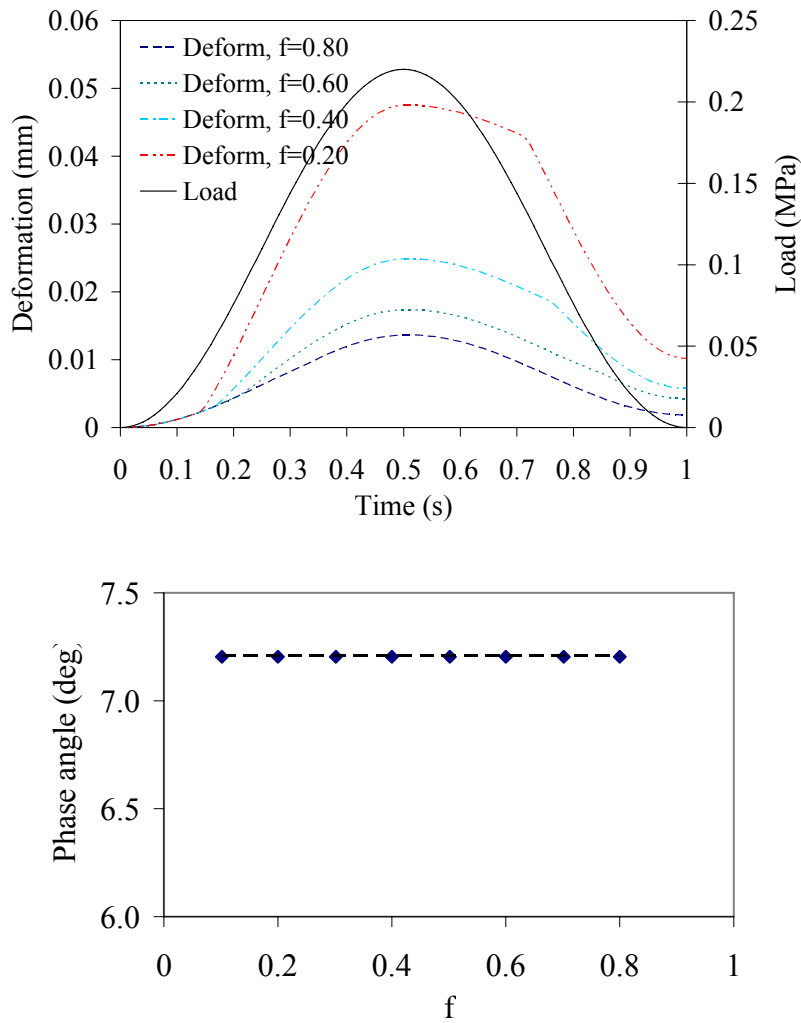


Figure 6-29 Effect of parameter  $f$  on the phase angle for numerical dynamic modulus test

Although the graphs (Figure 6-23 and Figure 6-24) show that the model was calibrated to simulate the sample responses very well, it should be noted that for different mixes or different samples, i.e. for samples with different microstructure configurations, the material parameters should be calibrated again. Nevertheless, the model can not take into account the microstructure of samples explicitly. In order to study the effect of phase variation on the sample response, which is very important (Zhang *et al.*, 2006), the microstructure of sample should be incorporated in the digitalized model.

## 6.4 Microscopic study

Three dimensional microscopic models were built for the indirect tensile test and dynamic modulus test considering phase variation of different mixtures to achieve the final stage of the overall development: the digital specimen and the digital test

functionality. The microstructural information is from the x-ray scanning of the real sample. Linear elastic material model is used for aggregates while the two layer viscoplastic material model is used for asphalt binder. The voids are removed before the application of the repeated loading. The loading is applied through the form of boundary traction. The displacement of the loading point is monitored and the displacement history is recorded along with the loading history.

Due to computing time and the limitation of the computer memory and disk space, especially for repeated loading simulation with viscoplastic material model, all the images with original 512×512 resolution were re-digitalized before the building of the finite element model. This is done by maintaining the volume fractions of both the voids and aggregates during the conversion. A FORTRAN program was developed to automatically carry out the conversion of the microstructure and the generation of the finite element model (Figure 6-30).

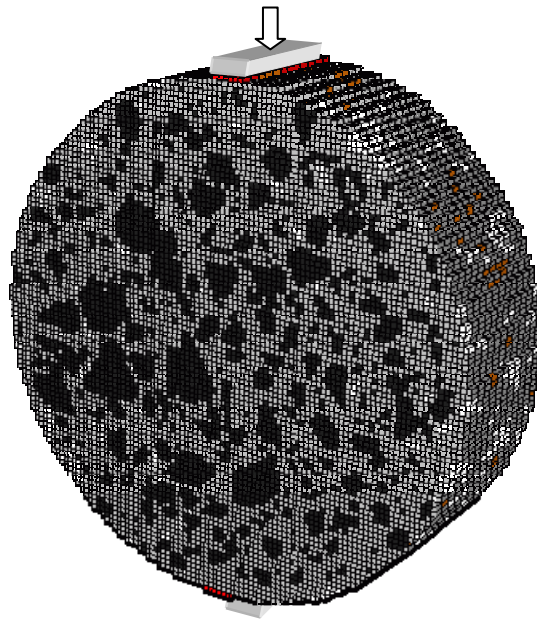


Figure 6-30 Microscopic finite element model for the indirect tensile test

In order to validate these concepts, mixtures from the WesTrack project were numerically tested with the procedure developed in details in Chapter 4 and Chapter 5. Three mixtures were subjected to sinusoidal loading with the same pattern and magnitude so that we can obtain comparable deformation responses for different mixtures. The results plotted in Figure 6-31 indicate the different strain responses for different mixtures with the same material properties for each component. The graph shows the deformation history of the three mixes mentioned before. The fine-plus mix, as expected, demonstrated larger deformation than the fine mix. However, the coarse mix experienced less deformation than the fine plus mixture. This may be due to the selection of material parameters and the interpretation of the phases from scanning images based on volume fractions. The loss of accuracy when converting images from high resolution to low resolution was minimized by keeping consistent phase fractions. Meanwhile, three levels

of re-digitalization are conducted and numerically tested with the same material model and same set of material parameters. The simulation of ten loading cycles with the same sample size and loading pattern were obtained (Figure 6-32).

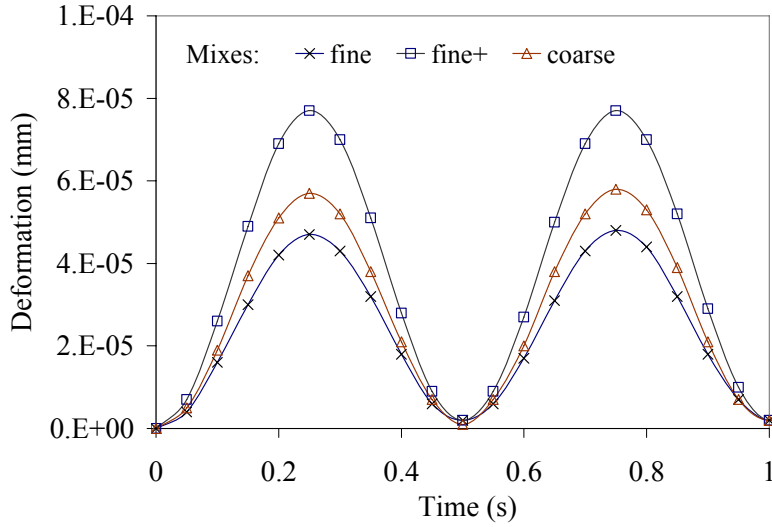


Figure 6-31 Microscopic numerical testing of samples from WesTrack mixtures

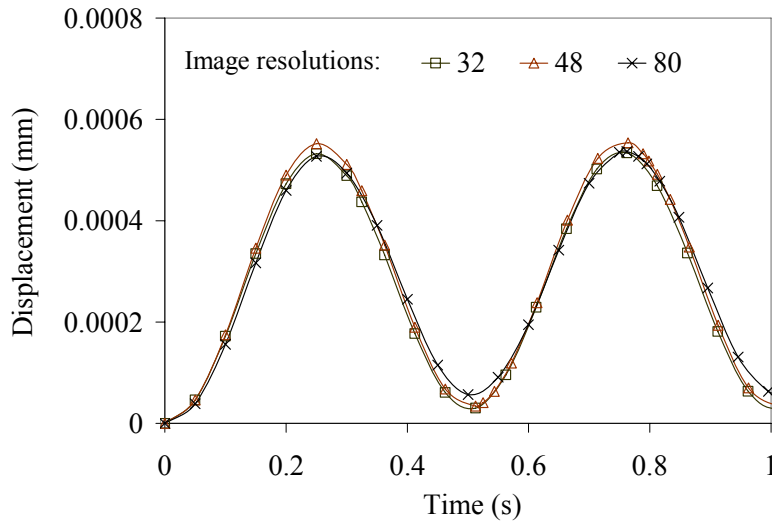


Figure 6-32 Displacement profile for mesh size 5mm, 3mm, and 2mm

The parameters can be calibrated using the back-calculation method following the same approach as in the macroscopic study illustrated previously. As for the time history, we can expect that the difference of the deformation for these three mixes increases with the increase of the loading cycles. This shows the importance of the sample microstructure when dealing with large number of cycles of repeated loading which is the real situation of asphalt pavement.

The dynamic modulus test of the same sample can be achieved by changing the traction boundary conditions. A uniaxial loading will be applied along the main axis of the sample instead of its diametrical axis. Due to the lack of microstructural and mechanical experiment data, the further study will be conducted in future. Instead, small samples will be study in next chapters.

## **6.5 Conclusions**

This chapter presents the macroscopic study with viscoplastic material model. Material parameters were obtained through back calculation, which includes a detailed sensitivity study. This forms the basis of model back calculation for microscopic study involving sample microstructure. The simulation model includes methodology development with elastic and viscoplastic material models for aggregates and asphalt binder, respectively. By using a rate dependent material model for asphalt binder, this method rendered qualitatively realistic simulation of the response of the asphalt mixture comparing with the experimental results.

It was found from the statistic microscopic study that the mesh size affects the simulation results in terms of elastic stiffness of the deformation response. Generally, a coarse mesh will lead to a stiff deformation response. However, due to the effects of microstructure of the sample, softening may be observed with the configuration of voids and aggregates. In the sense of engineering estimation, the resolution change may cause minimal effects on the material parameter estimation as long as we use a mesh size small enough to capture the phase configuration (i.e. voids volume fraction and aggregates volume fraction) and we keep them unchanged during resolution transformation. This means that detailed asperity may not affect the response significantly.

The microscopic model enables study of effects of phase configuration on the mixture performance and calibration of material models independently on phase configurations. This leads to large advantages in both the model calibration and performance evaluation.

Future work will be focused on parameter estimation using this back calculation based on the simulation results, testing data and sensitivity analysis. Specifically, simulation and physical test will be carried out on small samples with different aggregate contents. Then, the viscoplastic model for asphalt binder can be further refined and will be used to conduct other testing simulation with the microstructure of the mixture.

## **Chapter 7      Small sample testing and simulation**

### **7.1 Introduction**

The combination of x-ray tomography imaging and finite element simulation provides an alternative for material characterization and a profound understanding of the behavior of composite materials (Wang *et al.*, 2001; Zhang *et al.*, 2005b; 2005a; Zhang *et al.*, 2006). In previous chapters, methods were developed to link the material response to the sample microstructure, which was characterized through x-ray tomography imaging. Programs were developed enabling the mapping of real microstructure into finite element simulation model. The back calculation based on the sensitivity analysis of material parameters were also carried out in a macroscopic statistic manner. The simulation successfully captured material performance qualitatively for different composite configurations, e.g. layered wood panels or asphalt mixtures with different aggregate gradations and void volume fractions.

In order to further verify the algorithms and procedures with laboratory test, small asphalt concrete samples that can be scanned with a microtomographic scanner were prepared with different aggregate volume fractions. The purpose of the experiment is to study the effect of aggregate volume fraction on the behavior of the sample and to further develop the concept and verify the algorithm and method developed in the characterization of composite materials.

X-ray microtomographic scanner was used in this study to obtain the microstructure of small asphalt samples and the incorporated testing stage was used to conduct uniaxial compressive test. The dimensions of the small sample were carefully determined to accommodate both the penetrating capability of the scanner and the loading and deformation limits of the testing stage. Due to these limitations, only small samples were prepared, scanned, and tested under a simple loading pattern for the verification purpose.

### **7.2 Methods**

#### **7.2.1 Testing sample design and preparation**

Totally eight samples were prepared in the asphalt laboratory of Virginia Tech Transportation Institute. The major variation factor of these samples is aggregate volume fraction.

### 7.2.1.1 Sample design

Sample size is designed according to x-ray energy and the testing chamber size. All samples are cylinders with 6mm diameter and 9mm height (Figure 7-1).

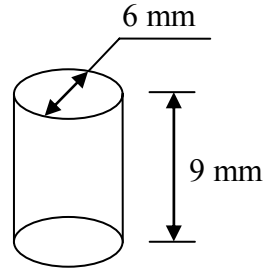


Figure 7-1 Testing sample geometry

Samples were designed with three levels of aggregate volume fraction that ranges from 5% to 50% (shown in Table 7-1). Samples with pure binder were also made. They were tested under uniaxial compression to obtain material properties of asphalt binder. The actual aggregate volume fractions may be different with the designed values due to the presence of voids, which are difficult to control for this kind of small samples, especially for samples with higher aggregate volume fraction. In this case, the actual volume fractions of aggregates and voids will be quantified through 3-D image analysis following the concept described in Chapter 4 and 5.

Table 7-1 Testing sample designation

Serial No.	Descriptions	Binder	Aggregates	Numbers
1a	Pure binder, without aggregates	PG64-22	None	1
1b				1
2a	with aggregates	PG64-22	5%	1
2b				1
3a	with aggregates	PG64-22	25%	1
3b				1
4a	with aggregates	PG64-22	50%	1
4b				1

The size of aggregates will be the same for all sample groups and the only variation will be the total volume fraction of aggregates. Aggregates passing No.16 sieve and remaining on No.30 (i.e. 0.6 ~ 1.18mm) were used. The minimum asphalt content is in the samples with maximum aggregate volume fraction.

### *7.2.1.2 Sample preparation*

All samples were prepared in VTTI asphalt laboratory. The process includes mould preparation, mixture design and sample preparation.

#### 7.2.1.2.1 Mould preparation

An aluminum mould was designed to make batch samples. Demould device and releasing agent were used to ensure the shape of the sample during demoulding. The sketch of the mould design is illustrated in Figure 7-2. All small samples are made longer than the design length and were cut to the required length before scanning and testing.

#### 7.2.1.2.2 Mixture design

Mixtures were made by controlling the weight of each component proportionally. The weight of each component was estimated from the targeted volume fractions of aggregates, i.e. 5%, 25% and 50 %. The calculation results are tabulated in Table 7-2 and Table 7-3.

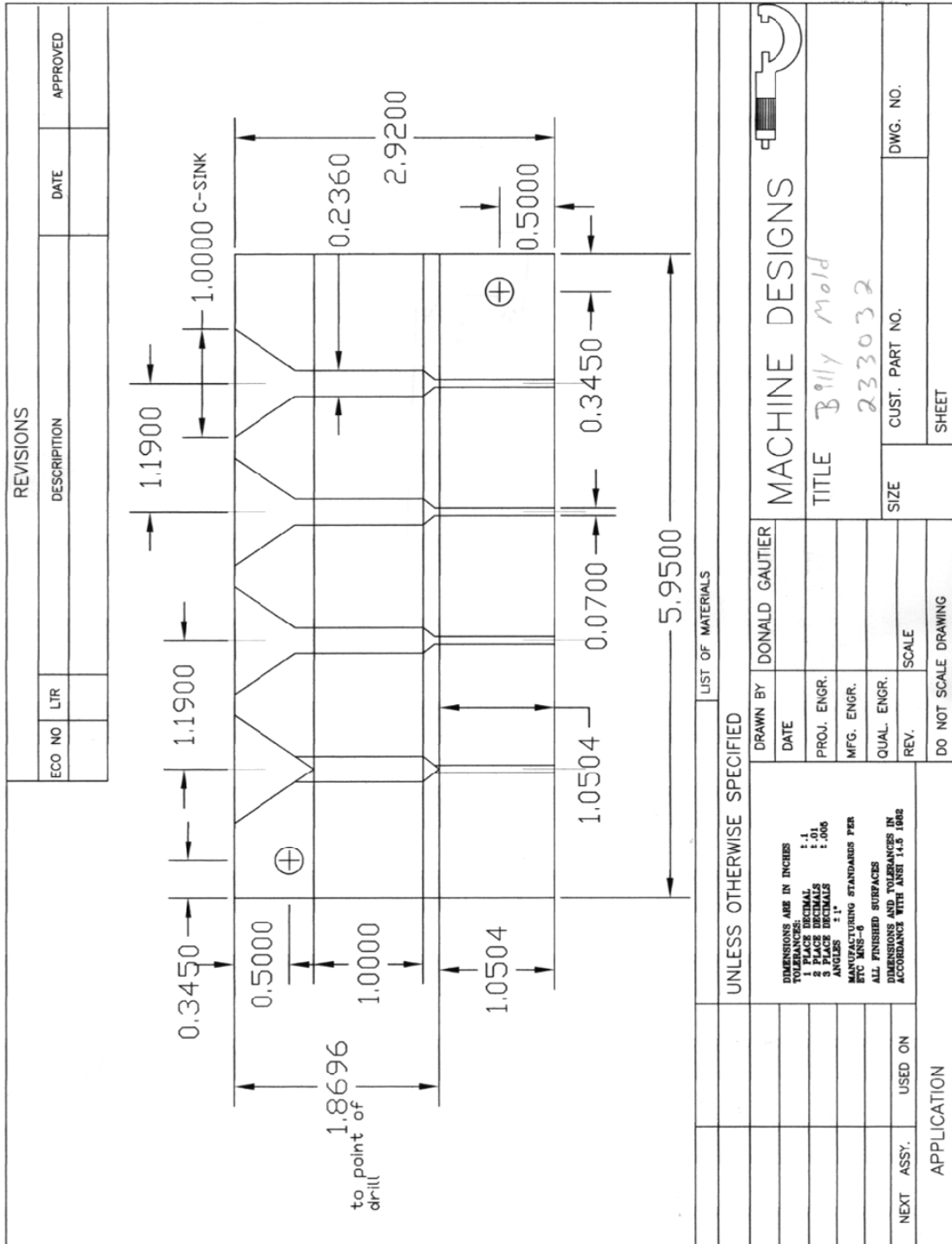


Figure 7-2 Mould design

Table 7-2 Weight of aggregates and binder for the sample size

Material	Diameter (mm)	Height (mm)	Volume (mm <sup>3</sup> )	Specific Gravity	Weight (g)
Aggregate	6	9	254	2.67	0.68
Asphalt	6	9	254	1.02	0.26

Table 7-3 Weight of aggregates and binder for different volume fractions

Volume fraction (%)		100	50	25	5
Weight (g)	Aggregates	0.68	0.34	0.17	0.034
	Asphalt	0.0	0.13	0.20	0.25

#### 7.2.1.2.3 Sample preparation

Asphalt binder was heated in the oven until melt and was poured into a small container with pre-calculated weight. Aggregates with proportional weight, shown in Table 7-3, were then added into the container with the weighted binder. The container may need to be put into the oven again during mixing. The mixture was put into the mould quickly before it cools down. Reheat is needed if the mixture hardens before being put into the mould. During this process, the sample was compacted with a stick in order to meet the designed volume fraction.

After being released from the mould, the sample was cut into 6mm length with a heated knife. Sample dimensions were measured with a microcalliper and the average value of each sample is listed in Table 7-4. Samples were put into refrigerator to maintain their shape and dimension before test. However, it takes time to put them into the testing stage before test, so the final dimension of the sample will be measured with on-screen imaging tools just before the starting of each test.

Table 7-4 Sample dimensions

Samples		Diameter	Height
Sample 1	a	6.05	9.16
	b	6.12	9.00
Sample 2	a	6.34	9.53
	b	6.19	9.10
Sample 3	a	5.84	9.08
	b	6.03	8.80
Sample 4	a	6.24	9.40
	b	5.73	8.65

## 7.2.2 Sample scanning and testing

SkyScan microtomographic system and testing stage (SKYSCAN, 2006) were used in this study to obtain the microstructure of small samples and to conduct uniaxial compressive test.

### 7.2.2.1 System specifications

#### 7.2.2.1.1 X-ray CT scanner specifications

- X-ray source: 20-50 kV with 40 W maximum power, filter holder is optional for energy selection and source filtration
- Detector: 1.3 MP CCD that is coupled to scintillator by lens with 1:6 zoom range
- Spatial resolution: 6 to 30  $\mu\text{m}$  pixel size with approximately 10  $\mu\text{m}$  low-contrast resolution
- Sample size: 5 to 30 mm in diameter, 50 mm in length
- Reconstruction: volumetric reconstruction with Feldkamp algorithm (Feldkamp et al., 1984)
- Testing stages: for micro-positioning, compression, extension and torsion test

#### 7.2.2.1.2 Testing stage

The material testing stage, shown in Figure 7-3, can perform compression, tension and torsion test. The loading-displacement or the stress-strain curve can be saved as an image or text file. Meanwhile, it allows the tomographic scanning of the sample during the test. The testing sample can be held under specific loading for scanning. The testing stage applies displacement to the top and bottom of the sample in equal amount but in opposite directions. This keeps the central part of the sample relatively static for scanning purpose.



Figure 7-3 Testing stage of the microscopy system (SKYSCAN, 2006)

The limitations to the testing sample geometries are listed below.

Maximum sample diameter:		6	mm
Sample length:	Compression:	10-17	mm
	Tension:	3-10	mm
	Torsion:	5-14	mm
Maximum loading:	Compression/Tension:	50	N
	Torsion:	10	N-cm
Loading speed range:	Compression/Tension:	1-16	m/s
	Torsion:	0.5-6.0	deg/s
Maximum displacement:	Compression/Tension:	10	mm
	Torsion:		unlimited

In all testing modes, the program controlling the material testing stage records the force-displacement curve, which can be saved as a text file. By changing the speed and direction of applied displacement, dynamic and cyclic loading conditions can be achieved in certain range. However, the limitations in stress loading control limited our study for sinusoidal or haversine-pulse loading patterns. In this study, only uniaxial compressive test with constant loading speed was conducted.

#### 7.2.2.2 Sample scan

Samples with aggregates were scanned before testing. The principal concepts and algorithms for scanning and image analysis are similar to those for large samples

described in chapter 4 and 5. For these small samples, the whole sample was scanned with one rotation under cone beam without vertical movement. The resolution of the scanning image was 512 by 512.

### 7.2.2.3 *Sample test*

All samples were tested at room temperature and uniaxial compression test was performed on these samples.

The testing stage is displacement controlled. The displacement speed was chosen according to the allowable range of the testing device. It was set at 15 $\mu$ m/s. The resistant force was monitored and recorded during the loading. When the force reaches the maximum allowable value of the testing stage, the displacement application will stop. For the small sample in this study, the application of displacement was stopped when the recorded load reaches 0.8 MPa, i.e. 22.64N force on the sectional area. This loading magnitude meets the limitation of the equipment. Prior to each test, the testing stage was calibrated according to the procedure recommended by the manufacturer. Force-displacement data was stored as a text file for each sample.

### 7.2.3 **Sample reconstruction, test simulation and parameter back calculation**

After scanning, sectional images of the small sample were reconstructed. The reconstructed sectional images were then used to conduct three-dimensional analysis, which determines volume fractions for aggregates, binder and voids. They were used to obtain the threshold value that will be used in the generation of the finite element model. 3-D visualization of these samples was carried out to generate the digital representations of these physical samples. The void volume fraction was quantified through image analysis for samples with different aggregate volume fractions.

Reconstructed sectional images were read with programs developed in IDL and transferred into a data file containing the microstructural information. The data file was read by a FORTRAN program to generate an input of the finite element model. The principal process is similar to that illustrated in previous chapters dealing with large asphalt concrete samples and wood panel samples. However, in this study, adaptive meshes were used for asphalt binder to account for large distortions that may occur in the thin asphalt layers between two aggregates. The aggregate and void volume fractions were determined through 3-D image analysis. The average value from the two samples of each group was used as the input of the model generation program to adjust proper threshold values between phases.

The simulation of the uniaxial compression test was conducted with a similar setting-up as a dynamic modulus test. The two layer viscoplastic material model, discussed in details in Chapter 6, was used for asphalt binder and an elastic model was used for aggregates. In this simulation model, loading plates were modeled as rigid surfaces. The movement of the top rigid surface was controlled with a downward displacement velocity of 15 $\mu$ m/s, which is the same as that in the physical test. In the simulation output, the reaction force on the moving rigid surface was recorded. Stresses of each element and displacements of each node were also requested in the field output for the whole loading process.

Parameters in the material model were estimated using the back calculation procedures based on the sensitivity study of the model conducted in Chapter 6. Following the back calculation procedures, the material parameters were calibrated for both asphalt binder and aggregates (i.e. viscoplastic and elastic material models) from one of these tests. Then, the same set of material parameters was used in the simulation of other samples with different aggregate volume fractions.

## 7.3 Results and discussions

### 7.3.1 Sample scanning and reconstruction

Figure 7-4 shows a small sample that is scanned within the testing stage. The height of the sample was measured on screen with software. This is the value at the beginning of the test. The black parts at top and bottom of the picture are loading plates. Figure 7-5 shows a reconstructed sectional image of the small sample. The particles with white color are aggregates. The region of interests (ROI) of the sectional image (the square with dashed line in the left image) was carefully selected in order for the generated finite element model to get accurate geometry and microstructure. Image processing module was developed to remove the part outside ROI. The right image in Figure 7-5 is a processed image, which is generated along with the finite element generation module. This operation can also be carried out during the sectional image reconstruction. However, this may lose some edge pixels in some sections, which will be reflected in the 3-D visualization.

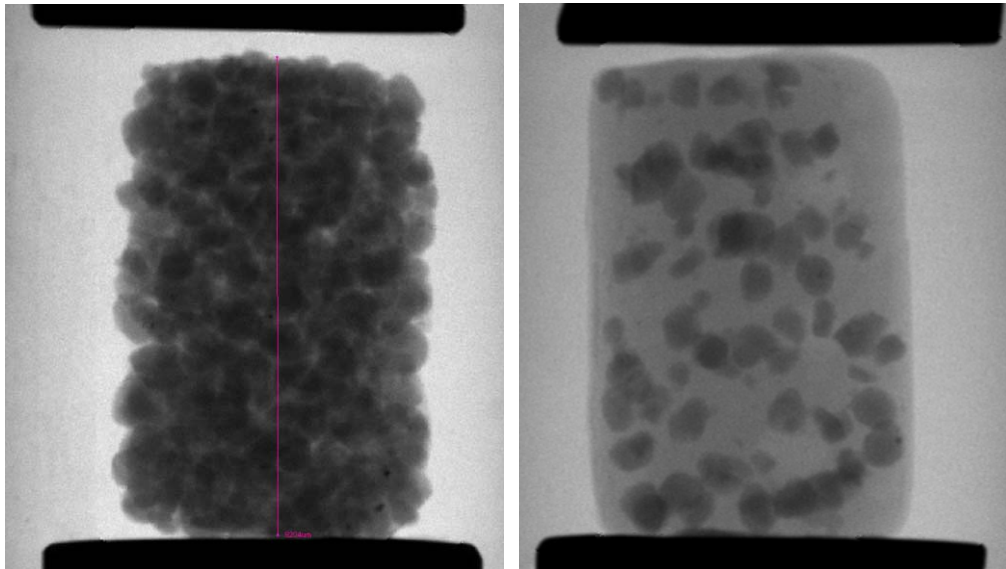


Figure 7-4 Samples with different aggregate volume fraction during scanning and before testing, (left) ~50% aggregates and (right) ~5% aggregates

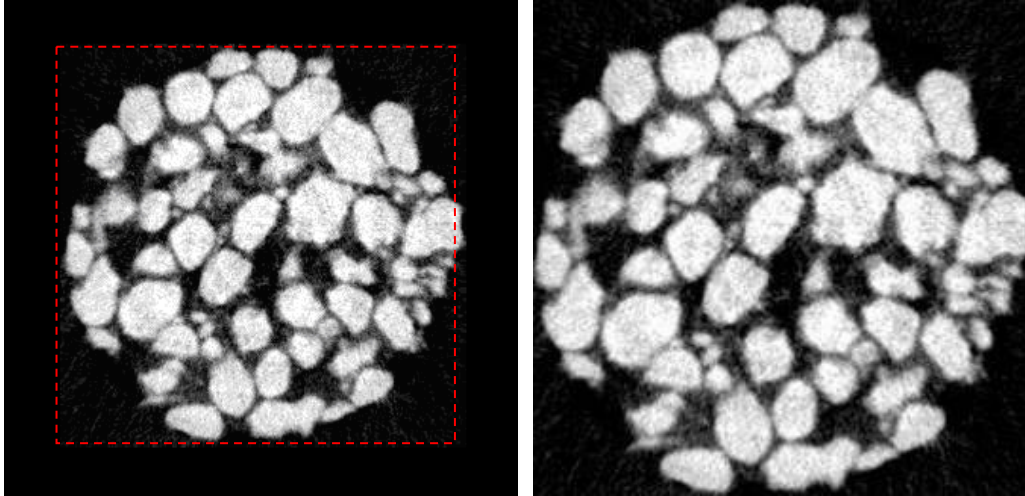


Figure 7-5 (left) Reconstructed sectional image used for 3-D visualization of the digital sample and (right) processed image generated during microscopic finite element model generation

### 7.3.2 Volume fraction of aggregates and voids

Due to the presence of voids, which is difficult to control in the small sample, the exact volume fraction in design is difficult to reach. The actual volume fractions of aggregates and voids were obtained through 3-D analysis of the reconstructed sample. The volume fraction of aggregates and voids for each sample is listed in Table 7-5. These values are important for the generation of the finite element model and the image resolution transformation during the model generation process.

Table 7-5 Volume fraction (%) of aggregates and voids

Sample ID		2a	2b	3a	3b	4a	4b
Volume fraction	Aggregates	5.87	4.04	22.42	23.49	50.52	49.27
	Voids	3.48	1.18	1.77	2.46	12.97	11.95

For these small samples, the void volume fraction seems related to the aggregate content. Figure 7-6 shows the relationship of measured void volume fraction and the aggregate volume fraction. If more samples would be made, we may form a more accurate trend between the volume fractions of these two phases for this kind of small samples. This may imply that we could estimate the void content by controlling the aggregate content based on some statistic results from 3-D image analysis. However, it should be pointed out that other factors, such as the shape and gradation of the aggregate will affect the volume fraction relationship as well.

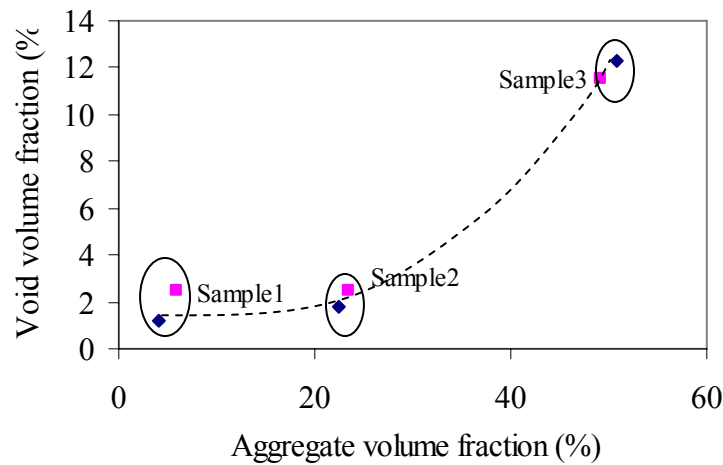


Figure 7-6 Aggregate volume fraction and void volume fraction statistical relationship, obtained from small sample 3-D analysis

### 7.3.3 Sample testing

#### 7.3.3.1 Loading speed and repetition

Most materials are subjected to loading rate effect, especially in the range of very high loading rate. The displacement speed range of this testing stage is 1-16  $\mu\text{m/s}$ , which is considered small to study the loading rate effect with small sample response. Due to its displacement control, the testing stage has also limitations on applying cyclic loading patterns although it can apply alternate compression and tension displacement.

The maximum displacement recorded varies from 1mm to 3mm. The typical force-displacement curve for each sample category is plotted in Figure 7-7. The sample with 50% aggregate volume fraction is significantly stiffer than other samples while the sample with 25% aggregate volume fraction has slightly larger stiffness over others. Generally, the more aggregates, the larger the stiffness. The oscillation of the curve is partially due to severe deformation of the sample, which induced the increase of the sectional area. However, only the beginning part of the curve was used to compare with finite element simulation results and to back calculate material parameters.

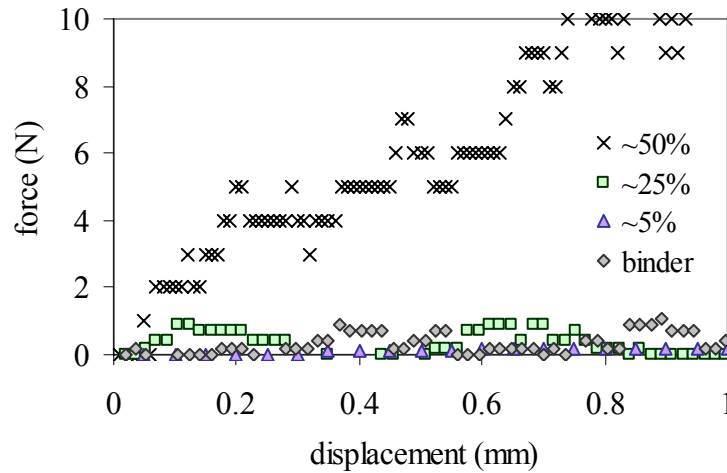


Figure 7-7 Typical force-displacement curves for different sample categories

### 7.3.3.2 Samples with pure binder

The resistant force recorded in the displacement controlled test, shown in Figure 7-8, is fairly small for the sample with pure binder even when the test stopped due to reaching of the maximum displacement of the testing stage.

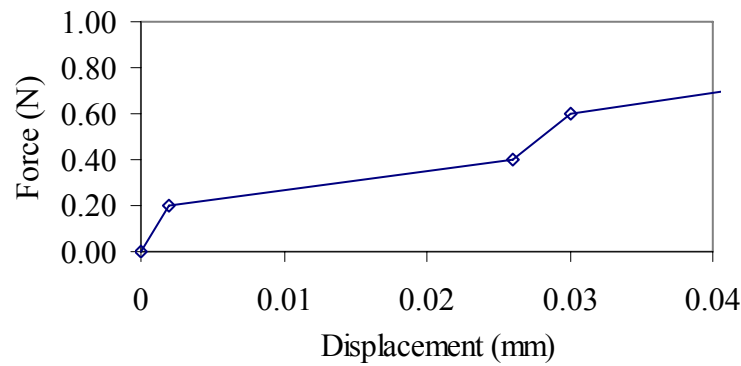


Figure 7-8 Load-displacement curve for pure binder under uniaxial compression

According to the force-displacement relationship, we calculated and established the stress-strain relationship, shown in Figure 7-9, for the pure binder sample. From this, we estimated elastic modulus, yielding stress and hardening property of the asphalt binder. These values were used as initial parameters for the back calculation.

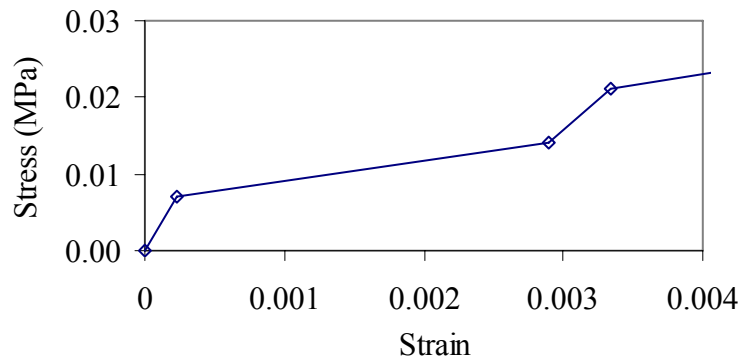


Figure 7-9 Stress-strain curve for pure binder under uniaxial compression

### 7.3.3.3 Samples with aggregates

Samples with different aggregate volume fractions were tested under the same loading speed as that for samples of pure binder. The displacement was controlled during the test while the maximum loading was also monitored in order to avoid significant damage of the sample microstructure. The recorded force-displacement curves of these tests are plotted in Figure 7-10. After adding aggregates into the asphalt binder, the behavior of the composite material is significantly different from that of pure binder, especially for samples with higher aggregate volume fraction. However, samples with 5% aggregate volume fraction only have slight difference with pure binder samples in term of force-displacement response.

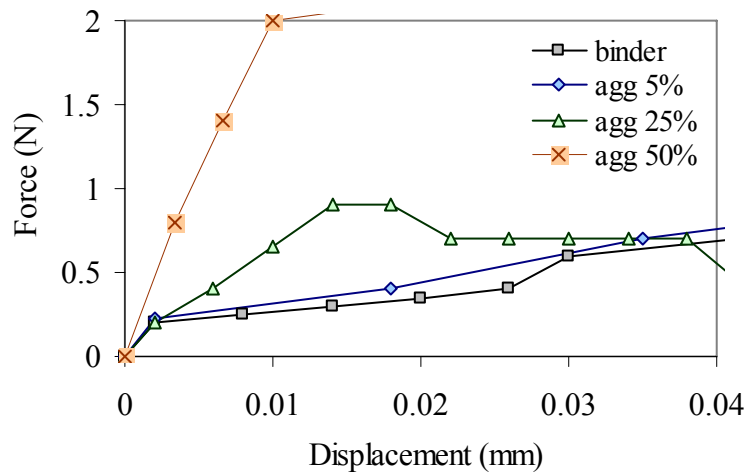


Figure 7-10 Force-displacement curves for samples with aggregates, sample2 (5%), sample3 (25%) and sample4 (50%), under uniaxial compression

### 7.3.4 3D visualization and test simulation

The visualization of reconstructed 3-D digital samples representing different aggregate volume fractions are shown in Figure 7-11. In the visualization, model parts for voids and binder were set to be partially transparent in order to show clearly the different configurations of aggregates. Similarly, other phases rather than aggregates, such as voids and binder can also be visualized separately. This is particularly useful in the study of void structure or connectivity.

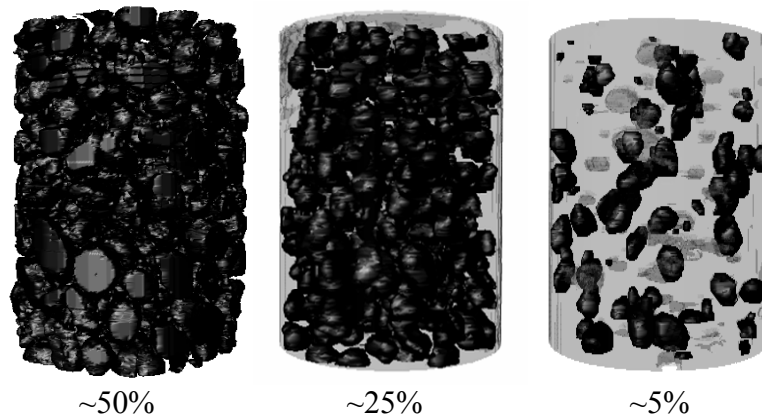


Figure 7-11 3-D visualization of small samples with different aggregate volume fractions: (left to right) 50%, 25% and 5%

The simulation of the test was conducted on the super computer in Virginia Tech's high performance computing facility which utilizes parallel computing and provides memory and disk space for solving large problems. The finite element model has approximately 30,000 elements. So, the mesh size is small enough to capture the size and shape of aggregates and voids and to reflect their effects on the deformation response. The simulative finite element model with sample microstructure is shown in Figure 7-12.

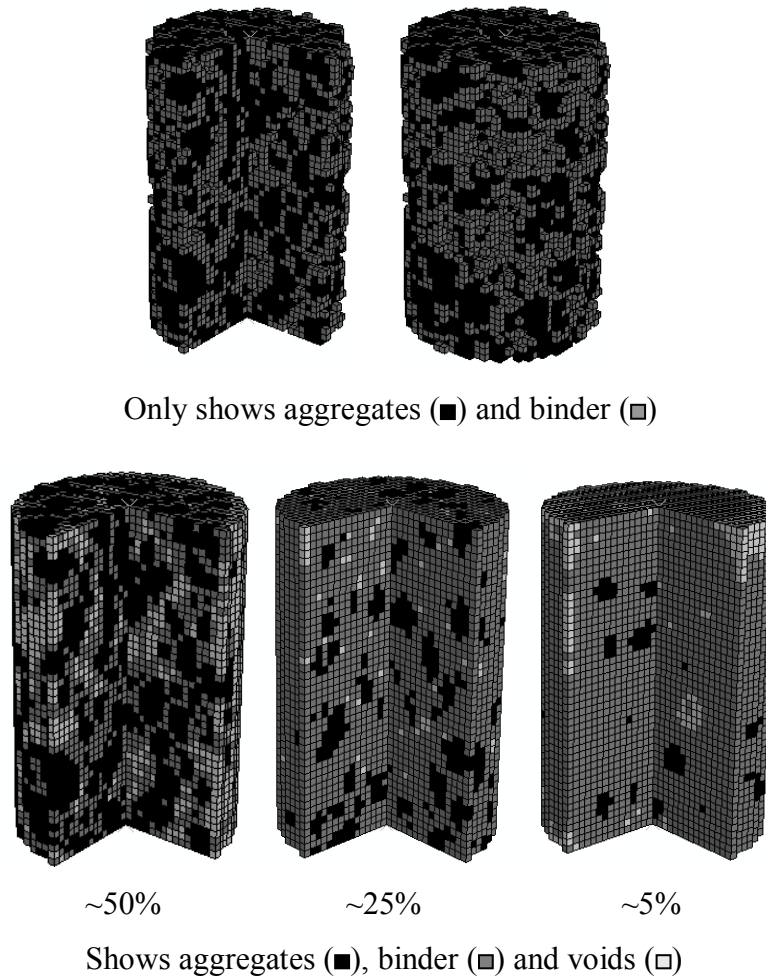


Figure 7-12 Finite element model for small samples, one quarter of the digital sample is taken out to show the internal microstructure

The whole simulation model, illustrated in Figure 7-13, includes the deformable part with microstructure and rigid loading plates. When comparing the aggregate configurations before and after loading from the displacement contour plot (Figure 7-13), we can observe some areas with much larger deformations associated with aggregate rotation. They are usually close to places with high concentration of voids.

The requirement of output visualization and post-processing were considered when building the model. The output data files from ABAQUS analysis were processed with a written FORTRAN program to generate tabulated data of step time, reaction force and displacement at loading point.

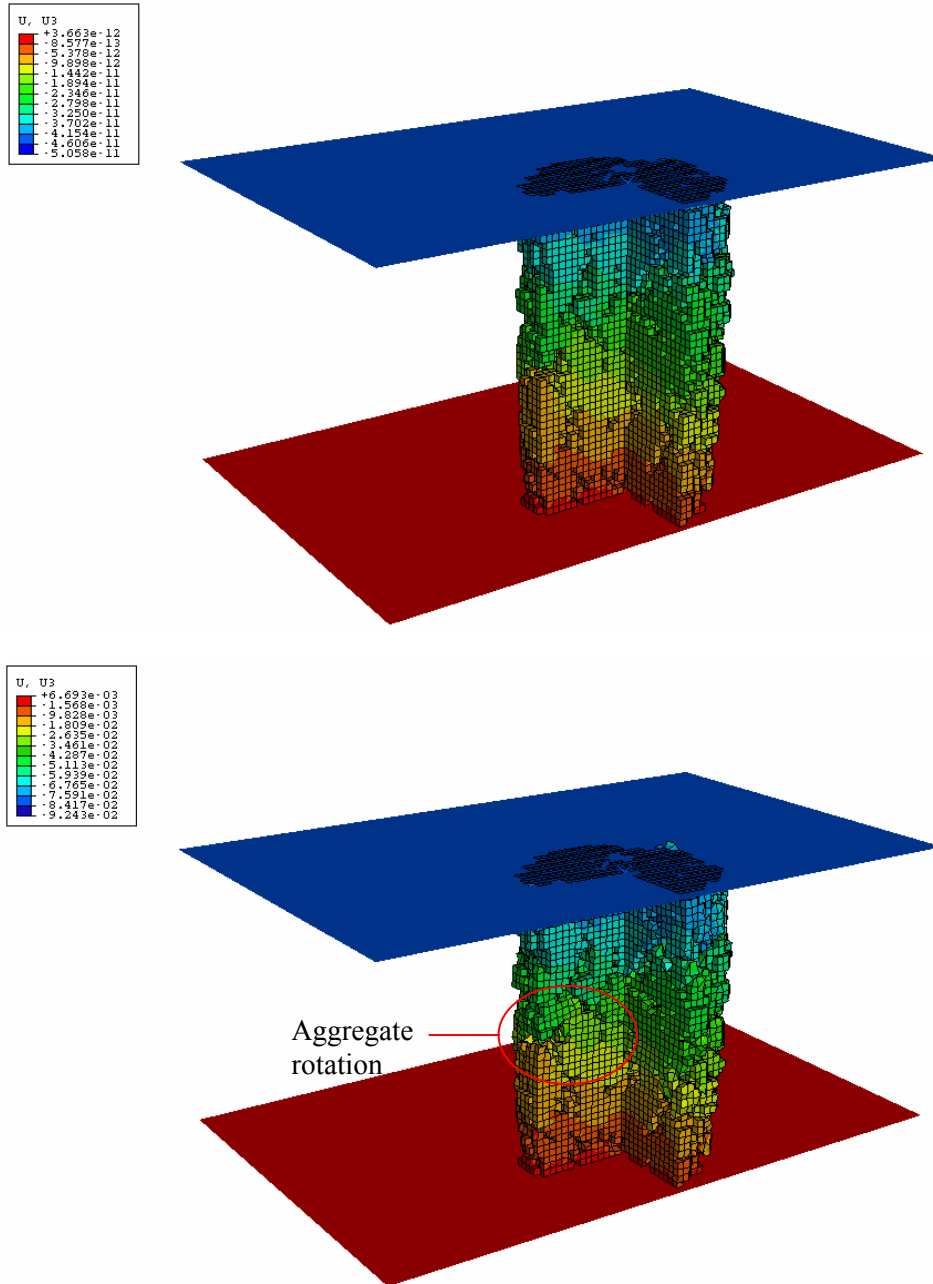


Figure 7-13 Finite element simulation model for the uniaxial compressive test of small asphalt samples, (upper) displacement before loading, (lower) displacement after loading

#### 7.3.4.1 Pure binder sample simulation

Numerical simulation of pure binder sample, shown in Figure 7-14, was conducted to obtain material properties of asphalt binder by comparing simulation response with testing counterpart. From the stress-strain relationship established in the test of pure binder sample, we obtained initial material parameters for the simulation.

Figure 7-15 shows the force-displacement relationship for the simulation with these parameters.

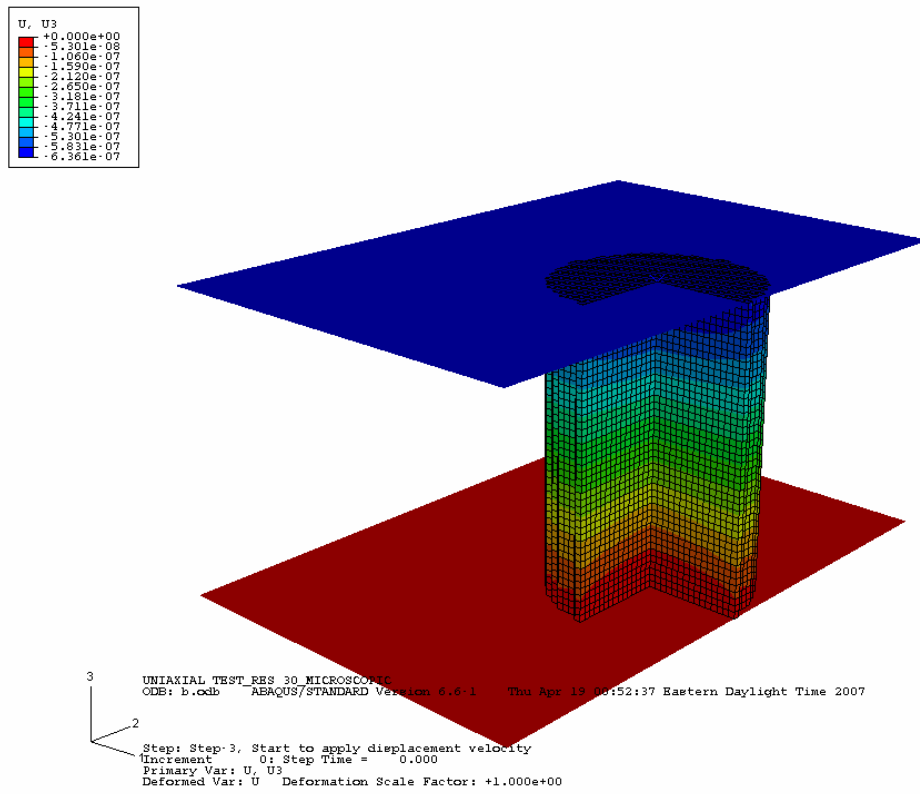


Figure 7-14 Finite element model for the pure binder sample simulation

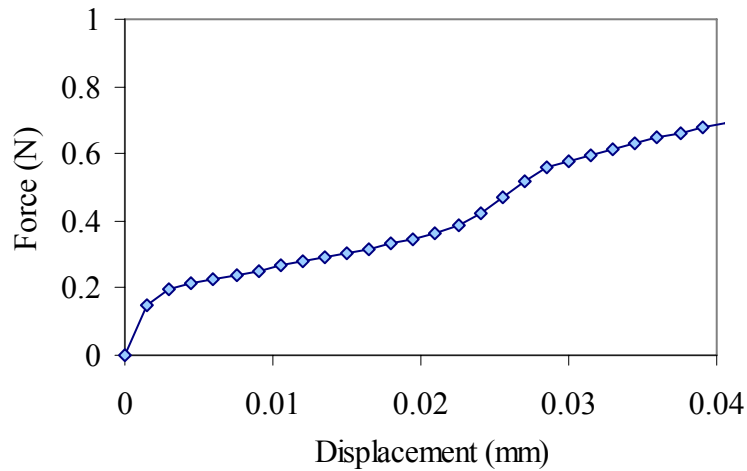


Figure 7-15 Simulation of pure binder samples with initial parameters from the sample test for the viscoplastic network of the model

### 7.3.4.2 Material parameter back calculation

Initial parameters in the viscoplastic model for asphalt binder were obtained from the stress-strain curve established from pure binder test. Based on the simulation and test of the pure binder sample, material parameters were optimized starting with initial values by minimizing the objective function, equation (7-1).

$$\sum_{i=1}^N (F_i^m - F_i^p)^2 \quad (7-1)$$

where  $N$  is the number of displacement points,  $F_i^m$ ,  $F_i^p$  are measured and predicted reaction forces, respectively. Material parameters obtained through back calculation are listed in Table 7-6. The final force-displacement curve for the simulation with these parameters was plotted side by side with the points obtained from the test in Figure 7-16. It can be seen that the results between simulation and test are very close.

Parameters for the elastic model used for aggregates are obtained through back calculation based on one set of sample with aggregates. However, the viscoplastic material parameters will remain the same and unchanged during the optimization of the elastic part. This will make the calibration relatively easier.

Table 7-6 Material parameters from back calculation

Parameters		Back calculated values
Asphalt binder	E	(N/mm <sup>2</sup> ) 31.83
	v	0.45
	σ <sub>y</sub>	(N/mm <sup>2</sup> ) 0.0070736
	σ <sub>u</sub>	(N/mm <sup>2</sup> ) 0.028294
	ε <sub>u</sub>	0.004
	A	1.0E-6
	n	0.8
	m	-0.18
	f	0.85
Aggregates	E	(N/mm <sup>2</sup> ) 210
	v	0.167

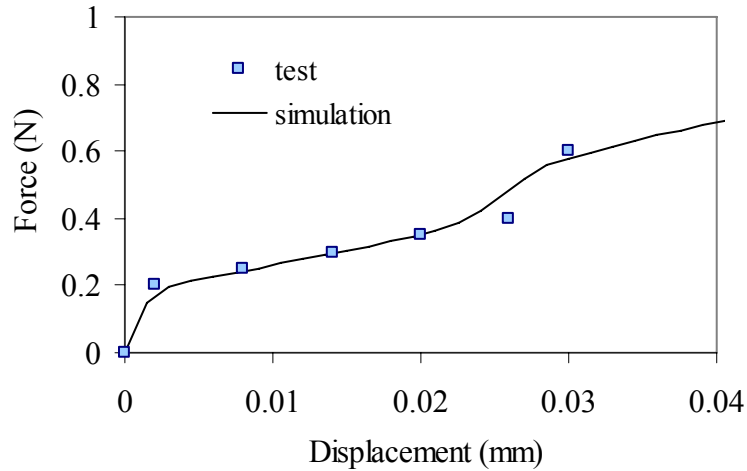


Figure 7-16 Force-displacement relationships from pure binder simulation and test, the back calculated parameters were used in the simulation

### 7.3.4.3 Simulation of samples with aggregates

The parameters of pure binder were used in all the simulations for samples with aggregates. The remaining elastic parameters for aggregates were obtained by adjusting parameters of the elastic model only in the simulation of the sample with 5% aggregate volume fraction. The back calculated parameters for aggregates are also listed in Table 7-6.

The back calculated parameters listed in Table 7-6 were used in the remaining simulations, i.e. for samples with aggregate volume fraction of 25% and 50%. The force-displacement curves for the simulation of all samples with aggregates are plotted in Figure 7-17. It is similar to the testing results in that adding of aggregates with leads to the increase of stiffness of the material.

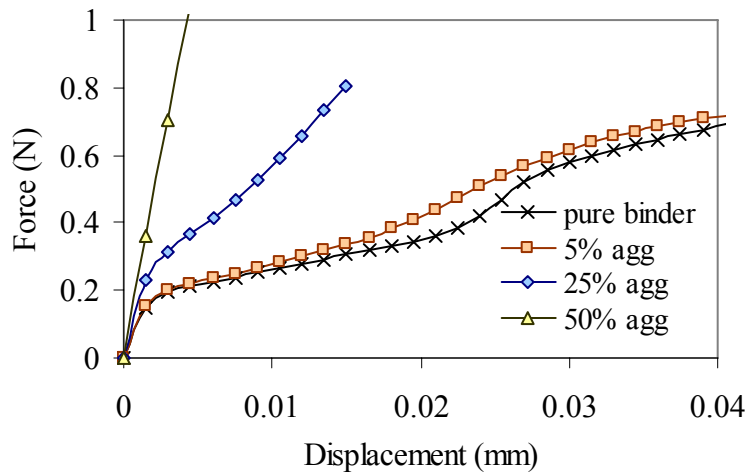


Figure 7-17 Force-displacement relationship from simulation

By putting the results of physical test together with those of numerical simulation, the force-displacement profiles, shown in Figure 7-18, indicates the validity of our method. It can be seen clearly that the results between simulation and test are close, especially for samples with lower aggregate content. The material parameters obtained from the test of pure binder and the sample with 5% aggregate are able to be used in the simulation of tests of other samples, which have different aggregate contents but the same material properties. It may also imply that material parameters obtained from individual material test could be used in the simulative test of composite material incorporated with its real microstructure. In this case, the real microstructural configuration is very important in the simulative test of composite materials besides the properties of individual component.

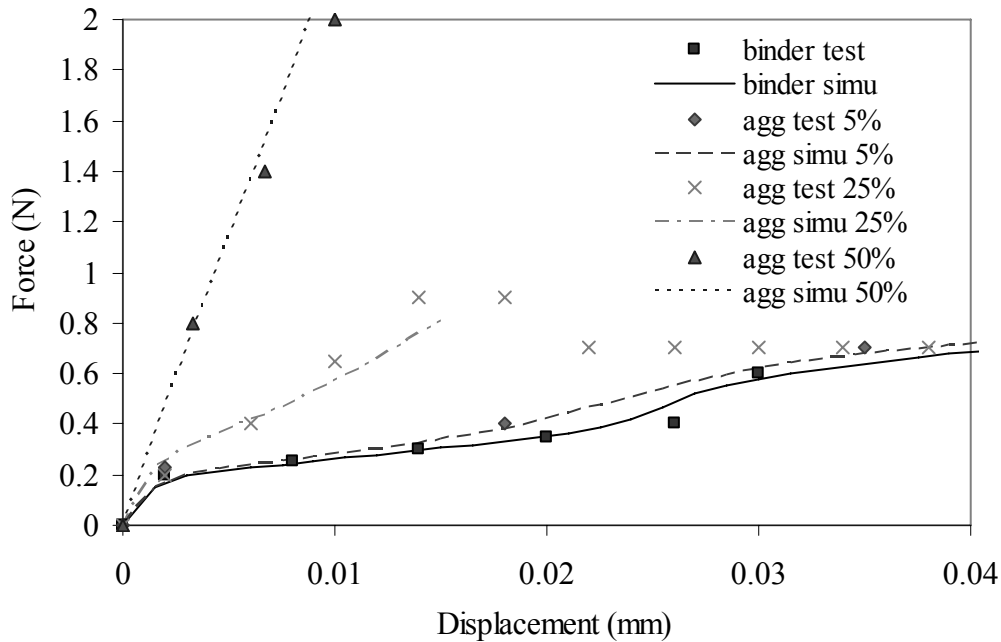


Figure 7-18 Simulation results with calibrated material parameters comparing with testing results

In both the physical and simulative test, the stiffness of samples with asphalt binder only is fairly small compared with samples with aggregates. This may be due to the lack of reinforcement provided by aggregates and aggregates' interlock action that is partially enhanced by asphalt binder. The interlock action may account for a large portion of the resistance to deformation. The more aggregates, the more contact, hence the more resistance. The stiffness of each sample was calculated at a displacement of 0.01mm from both physical and simulative test results. The relationship between stiffness and aggregate volume fraction, shown in Figure 7-19, shows the possible trend of increase of stiffness with the increase of aggregate content. It also indicates an increased rate of stiffness enhancement with the increase of aggregate volume fraction.

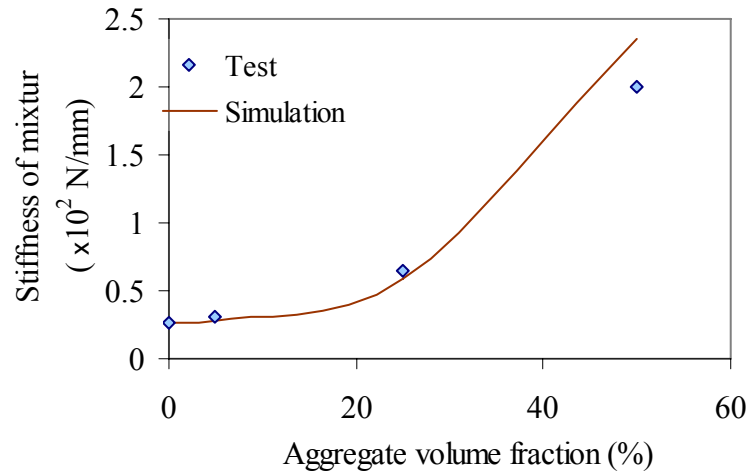


Figure 7-19 Stiffness vs. aggregate volume fraction for small samples at the deformation of 0.01mm

Both void volume fraction and aggregate volume fraction will affect the behavior of the mixture in terms of stress non-uniformity in the sample (Zhang *et al.*, 2006). The stress concentration factors were calculated for each group from stress distribution profile, shown in Figure 7-20, along the main axis. In the graph, axis 3 is the sample axial direction and axis 1 and 2 are diametrical directions. The sudden changes in the displacement profile, shown in Figure 7-21, may indicate a large local distortion or failure of the material either in shear or tension. However, it is not rational to relate stress concentration factors to the performance of sample groups with different aggregate contents. As our study indicated in Chapter 5, the stress concentration factor may serve as a good simple performance indicator if the volume fraction of each constituent is at a similar level.

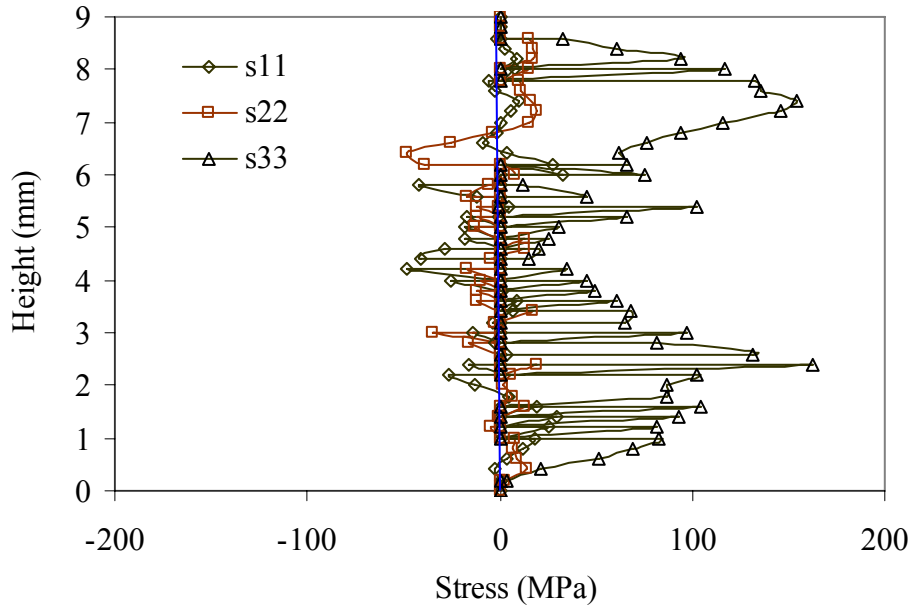


Figure 7-20 Stress distribution along the main axis of sample4a

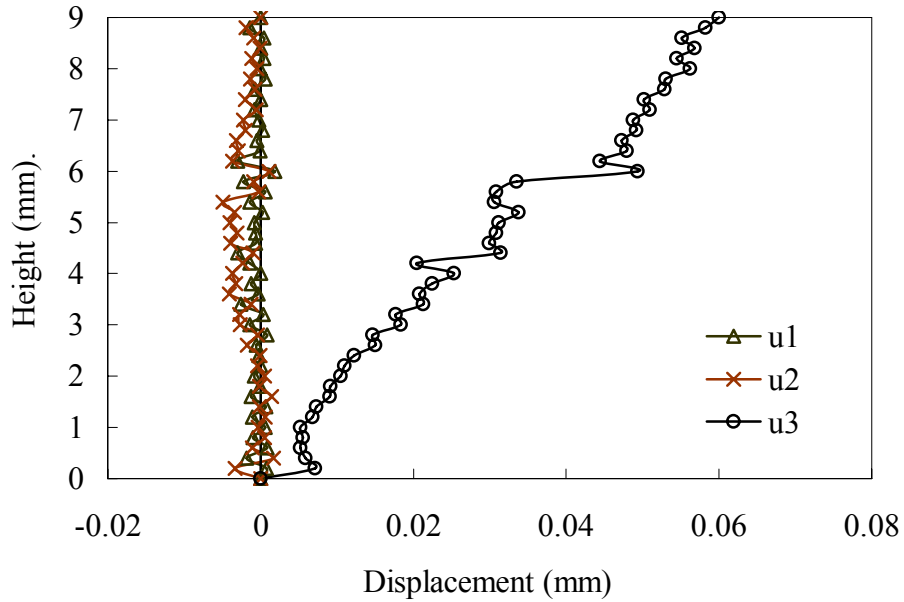


Figure 7-21 Displacement magnitude along the main axis of sample4a

## 7.4 Conclusions

The simulation model with sample microstructure obtained from micro-CT scanning was built to capture the phase configuration for different aggregate volume

fractions. 3-D image analysis determines the volume fraction of each constituent of the sample, which is the basis of thresholding that is very important for the microstructural model generation. The modeling includes displacement boundary applied through rigid surfaces and the moving speed of the boundary. Material parameters for the viscoplastic model were estimated from the sample test of pure binder through back calculation based on sensitivity analysis results. Test of sample with 5% aggregates was used for the calibration of the elastic model for aggregates. The same set of estimated material parameters were used in the simulation of samples with other aggregate contents. All the simulative tests captured the force-displacement relationship observed in their physical tests. It was found that the addition of aggregates will lead to an increased stiffness of the asphalt-aggregate composite with an increased rate. The results of 3-D image analysis may indicate that there is a relationship between void volume fractions and aggregate contents.

## **Chapter 8      Conclusions**

### **8.1    Overview**

Through (1) utilization of x-ray tomography imaging and 3-D image analysis, (2) development of macroscopic and microscopic simulative testing models for sensitivity analysis and material characterization, and (3) verification of the model through the physical and numerical tests of small asphalt samples and wood panels, viscoplastic responses of asphalt concrete related to void and aggregate contents and engineering properties of OSB related to density variations were studied. The major results of this research are: (1) a description of the generation of microscopic finite element simulative test model from x-ray scanning to data post-processing, (2) presentation of the verification of the model with small sample tests, (3) implementation and utilization of the model in various material characterizations, and (4) determination of factors affecting the accuracy and the limitations of its application.

### **8.2    Summary of conclusions**

X-ray scanning technology enables internal structure visualization and characterization of composite materials, such as wood OSB panel and asphalt concrete. Image processing technology enables phase identification and quantification (such as voids) in composite materials. Density profile was obtained from image analysis through density-void ratio (or pixel value) correlations.

In-plane density variation in OSB is an inherent property due to randomness in mat forming. In this work, elastic properties and in-panel stress concentrations of single-layer OSB under several density distributions and flake orientations were predicted using a finite element model. A FORTRAN program was written to automatically create the simulation model in ABAQUS for sets of material property inputs. It was found that the variation of in-plane density resulted in significant variation of localized stress concentrations both in- and out-of-plane. The overall panel elastic behavior varied slightly with the density deviations at the same mean density level, as long as there is no damage initiated in the board.

A three-layer (two face layers and one core layer with different flake alignment level) FEM model was formulated to investigate performance of anisotropic wood composite based on the one-layer FEM study. The FEM geometry model was built based on X-ray tomography and image analysis reflecting the actual microstructure of the testing samples to account for real density variation. Engineering properties characterized

numerically with FEM simulation are close to those measured with test, which is the first attempt to conduct digital testing of wood composite material.

Microscopic simulation model for IDT test was generated for the numerical test of three mixes from WesTrack data. The simulative test renders non-uniform stress and strain responses in the testing sample comparing with analytical solutions based on homogeneity. An evaluation of the stress distribution with and without consideration of voids indicated that voids induce significant non-uniform stress distribution. The modeling includes segmented sample simulations with statistically acceptable consistencies. The stress concentration varies significantly with the void distribution and the relative stiffness between aggregate and binder. We suggest that the IDT test should be combined with FEM simulation to offer better interpretation of the test results. The stress concentration factor may serve as a good simple performance indicator.

In the macroscopic study of the viscoplastic material model, material parameters were obtained through back calculation, which includes a detailed sensitivity study. This forms the basis of model back calculation for microscopic study involving sample microstructure. The simulation model includes methodology development with elastic and viscoplastic material models for aggregates and asphalt binder, respectively. By using a rate dependent material model for asphalt binder, this method rendered qualitatively realistic simulation of the response of the asphalt mixture comparing with the experimental results.

It was found from the statistic microscopic study that the mesh size affects the simulation results in terms of elastic stiffness of the deformation response. Generally, a coarse mesh will lead to a stiff deformation response. However, due to the effects of microstructure of the sample, softening may be observed with the configuration of voids and aggregates. In the sense of engineering estimation, the resolution change may cause minimal effects on the material parameter estimation as long as we use a mesh size small enough to capture the phase configuration (i.e. voids volume fraction and aggregates volume fraction) and we keep them unchanged during resolution transformation. This means that detailed asperity may not affect the response significantly.

The methods and procedures were verified through experimental and numerical test of small asphalt samples with different aggregate contents. The simulation model with test sample microstructure obtained from micro-CT scanning was built to capture the phase configuration of the sample due to specific aggregate volume fraction. 3D image analysis determines volume fraction of each constituent in the sample, which is the basis of thresholding in the microstructural model generation. The modeling includes displacement boundary applied through rigid surfaces and the moving speed of the boundary. Material parameters for the viscoplastic model were estimated from the sample test of pure binder through back calculation based on sensitivity analysis. Test of a sample with 5% aggregates was used for elastic model calibration. The same set of estimated material parameters were used in the simulation of samples with other different aggregate contents. All the simulative tests captured the force-displacement relationship observed in correspondent physical tests. It was found that the addition of aggregates will lead to an increased stiffness of the asphalt-aggregate composite with an increased rate. The results of 3-D image analysis may indicate that there is a relationship between void volume fractions and aggregate contents.

### **8.3 Implications**

For engineering materials such as wood panels, their engineering properties are related to density, flake type and packing process. The method developed in this work has potential applications in evaluating these materials from internal structure analysis, engineering property estimation and quality control.

We used resolution transformation during the generation of the microscopic model. From both the statistic study of repeated loading for different resolutions and the verification study of small samples, it seems that the resolution transformation will not cause qualitative effects on the results as long as the volume fractions of individual phases maintain.

From the study of the small samples, it may be implied that material parameters obtained from individual material test may be used directly in the simulative test of composite action of these materials with the incorporated real microstructure.

The interface between different materials is usually a weak zone. In this study, we haven't treated this zone as a particular phase. However, from the estimated material properties, the effect of this zone may be reflected in some parameters. Specifically for this study, the elastic modulus of aggregates may be affected. The asphalt binder properties were obtained from pure binder test, so we think they are not affected.

### **8.4 Recommendations of future research**

The microscopic finite element model simulation requires large memory and storage space and needs fast processors. If high resolution images are used for cyclic loading simulation, high performance computer has to be used. In order to overcome these limitations, new mesh generation method or mesh refinement techniques should be studied. However, three-dimensional mesh generation for multi-phase material is difficult, especially when avoiding using of linear tetrahedral element, which is over-stiff and inferior.

The focus of this study is in the range of small deformation. For the simulation of asphalt concrete with high loading rates, dynamic simulations may be used with damage initiation and revolution to study the performance of the asphalt concrete under cyclic loading with a large number of repetitions, which induce large deformation.

## References

Bio-Imaging Research Inc., ACTIS Reference Guide.

ABAQUS (1995). "User's Manual." *Hibbitt, Karlsson & Sorensen, Inc., Pawtucket, R.I.*

Abbas, A. R., A. T. Papagiannakis and E. A. Masad (2004). "Linear and Nonlinear Viscoelastic Analysis of the Microstructure of Asphalt Concrete." *Journal of Materials in Civil Engineering*, **16**(2): 133-139.

Adams, D. F. and D. R. Doner (1967). "Transverse normal loading of a unidirectional composites." *Journal of Composite Materials*, **1**: 152-164.

Aguilar Madeira, J. F., H. Rodrigues and H. Pina (2005). "Multi-objective optimization of structures topology by genetic algorithms." *Advances in Engineering Software*, **36**(1): 21-28.

Barnes, D. (2000). "Integrated model of the effect of processing parameters on the strength properties of oriented strand wood products." *Forest Products Journal*, **50**(11/12): 33-42.

Bentur, A. and I. Odler (1996). "Development and nature of interfacial microstructure." *Interfacial Transition Zone in Concrete (Edited by Maso J.C.), RILEM Report 11*: 18-44.

Braz, D., L. M. G. Da Motta and R. T. Lopes (1999). "Computed tomography in the fatigue test analysis of an asphaltic mixture." *Applied Radiation and Isotopes*, **50**(4): 661-671.

Chakraborty, S., M. Mukhopadhyay and O. P. Sha (2002). "Determination of Physical Parameters of Stiffened Plates using Genetic Algorithm." *Journal of Computing in Civil Engineering*, **16**(3): 206-221.

Chang, S. J., J. R. Olsen and W. P. C. (1989). "NMR imaging of internal features in wood." *Forest Prod. J.*, **39**(6): 43-49.

Chau, K. W. and F. Albermani (2003). "Knowledge-Based System on Optimum Design of Liquid Retaining Structures with Genetic Algorithms." *Journal of Structural Engineering*, **129**(10): 1312-1321.

- Chehab, G. R. and Y. R. Kim (2005). "Viscoelastoplastic Continuum Damage Model Application to Thermal Cracking of Asphalt Concrete." *Journal of Materials in Civil Engineering*, **17**(4): 384-392.
- Chiroiu, C., L. Munteanu, V. Chiroiu, P. P. Delsanto and M. Scalerandi (2000). "A genetic algorithm for determination of the elastic constants of a monoclinic crystal." *Inverse Problems*, **16**: 121-132.
- Chow, C. L., X. J. Yang and C. Edmund (2001). "Viscoplastic Constitutive Modeling of Anisotropic Damage Under Nonproportional Loading." *Journal of Engineering Materials and Technology*, **123**(4): 403-408.
- Collop, A. C., A. T. Scarpas, C. Kasbergen and A. d. Bondt (2003). "Development and finite element implementation of a stress dependent elasto-visco-plastic constitutive model with Damage for Asphalt." *TRB 2003 Annual Meeting CD-ROM*.
- Dai, C. and P. R. Steiner (1994a). "Spatial structure of wood composites in relation to processing and performance characteristics. Part 2. Modeling and simulation of a randomly-formed strand layer network." *Wood Sci. Technol.* , **28**(2): 135-146.
- Dai, C. and P. R. Steiner (1994b). "Spatial structure of wood composites in relation to processing and performance characteristics. Part 3. Modeling the formation of multi-layered random strand mat." *Wood Sci. Technol.*, **28**(3): 229-239.
- Dai, Q. and M. H. Sadd (2004). "Micromechanical Modeling of Damage-Coupled Viscoelastic Behavior of Asphalt Materials." *17th ASCE Engrg. Mech. Conf.*: Univ. of Delaware, Newark, DE, USA.
- Darwin, D. and F. O. Slate (1970). "Effect of paste-aggregate bond strength on behavior of concrete." *ASTM Journal of Materials*, **5**(1): 86-98.
- Desai, C. S. (2001). *Mechanics of Materials and Interfaces, The Disturbed State Concept*. Boca Raton, Florida, CRC Press LLC.
- Desai, C. S., S. Somasundaram and G. Frantziskonis (1986). "A hierarchical approach for constitutive modelling of geologic materials." *International Journal for Numerical and Analytical Methods in Geomechanics*, **10**(3): 225-257.
- Desrues, J., R. Chambon, M. Mokni and F. Mazerolle (1996). "Void Ratio Evolution inside Shear Bands in Triaxial Sand Specimen Studied by Computed Tomography." *Geotechnique*, **46**(3): 529-546.
- Dolinsek, J., P. Jeglic, T. Apih, G. Lahajnar, O. Naglic and A. Sever (2000). "Temperature-dependent bitumen softening studied by NMR." *Journal of Physics D: Applied Physics*, **33**(13): 1615-1624.

- Duvaut, G. and J. L. Lions (1972). *Les Ine'quations en Me'chanique et en Physique*. Dunod, Paris.
- Ellis, S., D. J. and S. Avramidis (1994). "Determination of parallam macroporosity by two optical techniques." *Wood Fiber Sci.*, **26**(1): 70-77.
- Epps, J., C. L. Monismith, S. H. Alavi and T. M. Mitchell (1997). "WesTrack Full-Scale Test Track: Interim Findings."
- Etse, G. and K. Willam (1999). "Failure analysis of elastoviscoplastic material models." *Journal of Engineering Mechanics*, **125**(1): 60-69.
- Faruque, M. O. and C. S. Desai (1985). "Implementation of a general constitutive model for geological materials." *International Journal for Numerical and Analytical Methods in Geomechanics*, **9**(5): 415-436.
- Feldkamp, L. A., L. C. Davis and J. W. Kress (1984). "Practical cone beam algorithm." *Journal of the Optical Society of America A*, **1**: 612-619.
- Funt, V. B. and B. E. C. (1987). "Detection of internal log defects by automatic interpretation of computer tomography images." *Forest Prod. J.*, **37**(1): 56-62.
- Garboczi, E. J. and D. P. Bentz (1991). "Digital simulation of the aggregate-cement paste interfacial zone in concrete." *Journal of Materials Research*, **6**(1): 196-201.
- Geimer, R. L. (1976). "Flake alignment in particleboard as affected by machine variables and particle geometry." Research Paper 275, USDA Forest Prod. Lab. Madison, WI.
- Gibson, N. H., C. W. Schwartz, R. A. Schapery and M. W. Witezak (2003). "Viscoelastic, Viscoplastic, and Damage Modeling of Asphalt Concrete in Unconfined Compression." *Transportation Research Record*, **1860**: 3-15.
- Guler, M., P. J. Bosscher and M. E. Plesha (2002). A porous elastoplastic compaction model for asphalt mixtures with parameter estimation algorithm. *15th ASCE Engineering Mechanics Conference*. June 2-5, 2002, Columbia University, New York, NY.
- Gurson, A. L. (1977). "Continuum Theory of Ductile Rupture by Void Nucleation and Growth: Part I - Yield Criteria and Flow Rules for Porous Ductile Media." *Journal of Engineering Materials and Technology*, **99**: 2-15.
- Hall, C. C., S. L. Jupe, A. C. Jacques, S. D. M. Livingston, R. Ramadan, A. O. A. Amde, A. Barnes and W. Paul (2000). "Non-destructive tomographic energy-dispersive diffraction imaging of the interior of bulk concrete." *Cem. Concr. Res.*, **30**(3): 491-495.

- Hondros, G. (1959a). "The evaluation of Poisson's ratio and the modulus of materials of a low tensile resistance by the Brazilian (indirect tensile) test with a particular reference to concrete." *Australian Journal of Applied Science*, **10**: 243-268.
- Hondros, G. (1959b). "Evaluation of Poisson's Ratio and the Modulus of Materials of a Low Tensile Resistance by the Brazilian (Indirect Tensile) Test with Particular Reference to Concrete." *Australia Journal of Applied Science*, **10**(3): 243-268.
- Hughes, T. J. R. and R. L. Taylor (1978). "Unconditionally stable algorithms for quasi-static elasto/visco-plastic finite element analysis." *Computers & Structures*, **8**(2): 169-173.
- Hunt, M. O. and S. K. Suddarth (1974). "Prediction of elastic constants of particleboard." *Forest Prod. J.*, **24**(5): 52-57.
- Ju, J. W. and K. H. Tseng (1996). "Effective elastoplastic behavior of two-phase ductile matrix composites: A micromechanical framework." *International Journal of Solids and Structures*, **33**(29): 4267-4291.
- Kang, H. D. and K. J. Willam (1999). "Localization Characteristics of Triaxial Concrete Model." *Journal of Engineering Mechanics*, **125**(8): 941-950.
- Kang, H. D. and K. J. Willam (2000). "Performance evaluation of elastoviscoplastic concrete model." *Journal of Engineering Mechanics, ASCE*, **126**(9): 995-1000.
- Kichenin, J., K. D. Van and K. Boytard (1996). "Finite-element simulation of a new two-dissipative mechanisms model for bulk medium-density polyethylene." *Journal of Materials Science*, **31**(6): 1653-1661.
- Kim, J. R., A. Drescher and D. E. Newcomb (1997). "Rate Sensitivity of Asphalt Concrete in Triaxial Compression." *J. Mat. in Civil Engrg., ASCE*, **9**(2): 76-84.
- Kim, Y.-R., D. N. Little and R. L. Lytton (2003). "Fatigue and Healing Characterization of Asphalt Mixtures." *Journal of Materials in Civil Engineering*, **15**(1): 75-83.
- Kim, Y. R., J. S. Daniel and H. Wen (2002). "FATIGUE PERFORMANCE EVALUATION OF WESTRACK ASPHALT MIXTURES USING VISCOELASTIC CONTINUUM DAMAGE APPROACH." *Research Project No. HWY-0678*, North Carolina Department of Transportation, (FHWA/NC/2002-004): 231.
- Landis, E. N. and K. T. Denis (1999). "X-ray microtomography for fracture studies in cement-based materials." *Proceedings of SPIE - The International Society for Optical Engineering, Society of Photo-Optical Instrumentation Engineers, Bellingham WA USA*, **3772**: 105-113.

- Lang, E. M. and M. P. Wolcott (1996). "A model for viscoelastic consolidation of wood-strand mats: Part I. Structural characterization of the mat via Monte Carlo simulation." *Wood Fiber Sci.*, **28**(1): 100-109.
- Lee, H. J. and Y. R. Kim (1998a). "Viscoelastic Constitutive Model for Asphalt Concrete under Cyclic Loading." *ASCE Journal of Engineering Mechanics*, **124**(1): 32-40.
- Lee, H. J. and Y. R. Kim (1998b). "Viscoelastic Continuum Damage Model of Asphalt Concrete With Healing." *ASCE Journal of Engineering Mechanics*, **124**(11): 1224-1232.
- Lee, J. N. and Q. Wu (2003). "Continuum modeling of engineering constants of oriented strandboard." *Wood Fiber Sci.*, **35**(1): 24-40.
- Lenth, C. A. and F. A. Kamke (1996). "Investigations of flakeboard mat consolidation. Part I. Characterizing the cellular structure." *Wood Fiber Sci.*, **28**(2): 153-167.
- Masad, E., V. K. Jandhyala, N. Dasgupta, N. Somadevan and N. Shashidhar (2002). "Characterization of Air Void Distribution in Asphalt Mixes Using X-Ray Computed Tomography." *J. Mat. Civil Engrg.*, **14**(2): 122-129.
- Mindess, S. (1996). "Tests to determine the mechanical properties of the interfacial zone." *Interfacial Transition Zone in Concrete (Edited by Maso J.C.)*, RILEM Report 11: 47-63.
- Nemat-Nasser, S. and D. T. Chung (1992). "An explicit constitutive algorithm for large-strain, large-strain-rate elastic-viscoplasticity." *Computer Methods in Applied Mechanics and Engineering*, **95**(2): 205-219.
- Oeser, M. and B. Moller (2004a). "3D Constitutive Model for Asphalt Pavements." *International Journal of Pavement Engineering*, **5**(3): 153 - 161.
- Oeser, M. and B. Moller (2004b). "3D Constitutive modeling for asphalt pavements." *International Journal of Pavement Engineering*, **5**(3): 153-161.
- Panoskaltzis, V. P. and D. Panneerselvam (2005). AN ANISOTROPIC HYPERELASTIC-VISCOPLASTIC DAMAGE MODEL FOR ASPHALT CONCRETE MATERIALS AND ITS NUMERICAL IMPLEMENTATION. *5th GRACM International Congress on Computational Mechanics, 29 June-1 July, 2005, Limassol, Cyprus.*
- Park, S. W., Y. R. Kim and R. A. Schapery (1996). "A Viscoelastic Continuum Damage Model and Its Application to Uniaxial Behavior of Asphalt Concrete." *Mechanics of Materials*, **24**(4): 241-257.
- Peirce, D., C. F. Shih and A. Needleman (1984). "A tangent modulus method for rate dependent solids." *Computers & Structures*, **18**(5): 875-887.

- Perl, M., J. Uzan and A. Sides (1983). "Visco-elasto-plastic constitutive law for a bituminous mixture under repeated loading." *Transportation Research Record*, **911**: 12-26.
- Perzyna, P. (1963). "The Constitutive Equations for Work-Hardening and Rate-Sensitive Plastic Materials." *Proceedings on Vibration Problems*, **4**: 281-290.
- Perzyna, P. (1966a). "Fundamental problems in viscoplasticity." *Advances in Applied Mechanics*, **9**: 244-368.
- Perzyna, P. (1966b). "Fundamental problems in viscoplasticity." *Advances in Applied Mechanics*, **9**: 243-377.
- Radaelli, F., M. Balzarini, S. Nicula and A. Ortenzi (1998). "Rock structure characterization through imaging techniques integration." *Proceedings of the European Petroleum Conference, Soc Pet Eng (SPE) Richardson, TX., USA*, **1**: 23-25.
- Reddy, M. A., K. S. Reddy and B. B. Pandey (2004). "Selection of Genetic Algorithm Parameters for Backcalculation of Pavement Moduli." *International Journal of Pavement Engineering*, **5**(2): 81 - 90.
- Rogasik, H. C., J. W. Wendroth, O. Young, I. M. Joschko and M. K. Ritz (1999). "Discrimination of soil phases by dual energy X-ray tomography." *Soil Sci Soc Am J.*, **63**(4): 741-751.
- Sadd, M. H., Q. Dai and V. Parameswaran (2002). "Microstructural Simulation of Asphalt Material: Modeling and Experimental Studies." *J. Mat. in Civil Engrg., ASCE*, **16**(2): 107-115.
- Sadd, M. H., Q. Dai, V. Parameswaran and A. Shukla (2004). "Simulation of Asphalt Materials Using a Finite Element Micromechanical Model and Damage Mechanics." *Transportation Research Record*, **1832**.
- Schapery, R. A. (1969). "On the Characterization of Nonlinear Viscoelastic Materials." *Polymer Engrg. and Sci.*, **9**(4): 295-310.
- Schapery, R. A. (1984). "Correspondence principles and a generalized J-integral for large deformation and fracture analysis of viscoelastic media." *International Journal of Fracture*, **25**(3): 195-223.
- Schapery, R. A. (1990). "A Theory of Mechanical Behavior of Elastic Media with Growing Damage and Other Changes in Structure." *J. Mech. Phys. Solids*, **38**: 215-253.
- Schapery, R. A. (1999). "Nonlinear viscoelastic and viscoplastic constitutive equations with growing damage." *International Journal of Fracture*, **97**(1 - 4): 33-66.

- Schmidt, H. and G. Thierauf (2005). "A combined heuristic optimization technique." *Advances in Engineering Software*, **36**(1): 11-19.
- Schwartz, C. W., N. H. Gibson, R. A. Schapery and M. W. Witzak (2002). "Viscoplasticity Modeling of Asphalt Concrete Behavior." *Recent Advances in Material Characterization and Modeling of Pavement Systems* (Tutumluer, E., Masad, E., and Najjar, Y., ed.), *ASCE-Geotechnical Special Publication*, **123**: 144-159.
- Scrivener, K. L. and P. L. Pratt (1996). "Characterisation of interfacial microstructure." *Interfacial Transition Zone in Concrete* (Edited by Maso J.C.), *RILEM Report 11*: 3-17.
- Seibi, A. C., M. G. Sharma, G. A. Ali and W. J. Kenis (2001). "Constitutive Relations for Asphalt Concrete Under High Rates of Loading." *Transportation Research Record*, **1767**: 111-119.
- Shaler, S. M. (1986). "The usefulness of selected polymer composite theories to predict the elastic moduli of orientated flakeboard." Pennsylvania State Uni.: 163pp.
- Shashidhar, N. (1999). "X-ray tomography of asphalt concrete." *Transp. Res. Rec.*, **1681**: 186-192.
- Shi, B. M., Y. Wu, Z. Chen and J. H. Inyang (1999). "Monitoring of internal failure evolution in soils using computerization X-ray tomography." *Eng. Geol.*, **54**(3): 321-328.
- SHRP (1993). "Resilient modulus for asphalt concrete." SHRP Test Designation: AC07, Protocol: P07.
- Sides, A., J. Uzan and M. Perl (1985). "A comprehensive viscoelastoplastic characterization of sand-asphalt under compression and tension cyclic loading." *Journal of Testing and Evaluation*, **13**(1): 49-59.
- Simo, J. C. (1987). "On a Fully Three-Dimensional Finite-Strain Viscoelastic Damage Model: Formulation and Computational Aspects." *Computer Methods in Applied Mechanics and Engineering*, **60**: 153-173.
- SKYSCAN (2006). SkyScan Brochure 2006, SkyScan Microtomography, Micro-CT Manual, SkyScan.
- Subramanian, L. (1993). "Analysis of the influence of voids on the hygroelastic properties of paper." Dept. of Mechanical Engineering, **M.S. thesis**, Florida Atlantic University: 164p.
- Suchsland, O. (1962). "The density distributions in strand boards. Michigan Quart. Bull." **45**(1): 104-121.

- Suchsland, O. and H. Xu (1989). "A simulation of the horizontal density distribution in a strandboard." *Forest Prod. J.*, **39**(5): 29-33.
- Sugimori, M. and F. Lam (1999). "Macro-void distribution analysis in strand-based wood composites using an X-ray computer tomography technique." *J. Wood Sci.*, **45**: 254-257.
- Tashman, L., E. Masad, H. Zbib, D. Little and K. Kaloush (2005a). "Microstructural Viscoplastic Continuum Model for Permanent Deformation in Asphalt Pavements." *Journal of Engineering Mechanics*, **131**(1): 48-57.
- Tashman, L., E. Masad, H. Zbib, D. Little and K. Kaloush (2005b). "microstructural viscoplastic continuum model for permanent deformation in asphalt pavements." *Journal of Engineering Mechanics, ASCE*, **131**(1): 48-57.
- Tseng, K. K. (2004). "Modeling and simulation of porous elastoviscoplastic material." *Journal of Engineering Mechanics, ASCE*, **130**(5): 547-550.
- Tvergaard, V. (1981). "Influence of Voids on Shear Band Instabilities under Plane Strain Condition." *International Journal of Fracture Mechanics*, **17**: 389-407.
- Uzan, J. (2005). "Viscoelastic--Viscoplastic Model with Damage for Asphalt Concrete." *Journal of Materials in Civil Engineering*, **17**(5): 528-534.
- Verhelst, F., A. D. B. Vervoort and G. Marchal (1995). "X-ray computerized tomography: Determination of heterogeneities in rock samples." *Cite, A.A. Balkema*, **1**: 105-109.
- Wang, L., J. D. Frost, G. Z. Voyiadjis and T. P. Harman (2002). "Quantification of Damage Parameters Using X-ray Tomography Images." *Journal of Engineering Mechanics*(Accepted for Publication).
- Wang, L., H. S. Paul, T. Harman and J. D'Angelo (2004). "Characterization of Aggregates and Asphalt Concrete using X-ray Tomography." *AAPT*, **73**: 467-500.
- Wang, L. B. (2003). "Stress Concentration Factor of Poroelastic Material by FEM Simulation and X-ray Tomography Imaging." " *ASCE Engineering Mechanics Conference, Seattle, WA*.
- Wang, L. B., J. D. Frost and N. Shashidhar (2001). "Microstructure Study of Westrack Mixes from X-ray Tomography Images." *TRR*, **1767**: 85-94.
- Wang, W. M., L. J. Sluys and R. d. Borst (1997). "Viscoplasticity for instabilities due to strain softening and strain-rate softening." *International Journal for Numerical Methods in Engineering*, **40**(20): 3839-3864.

- Wijk, G. (1978). "Some New Theoretical Aspects of Indirect Measurements of the Tensile Strength of Rocks." *Int. J. Rock Mech. Min. Sci. & Geomech. Abstr.*, **15**: 149-160.
- Wu, Q., J. N. Lee and G. Han (2003). "The influence of voids on the engineering constants of oriented strandboard: a finite element model." *Wood Fiber Sci.*, **35**(4): 92-104.
- Zhang, B., L. Wang and M. T. Tumay (2006). "An Evaluation of the Stress Non-Uniformity Due to the Heterogeneity of AC in the Indirect Tensile Test." *ASCE Geotechnical Special Publication*(No. 146): 29-43.
- Zhang, B., Q. Wu, L. Wang and G. Han (2005a). "Characterization of Internal Void Structure of Strand-based Wood Composites using X-ray Tomography and Digital Tools." *Proceedings of McMat2005: 2005 Joint ASME/ASCE/SES Conference on Mechanics and Materials*, June 1-3, 2005, Baton Rouge, Louisiana, USA.
- Zhang, B., Q. Wu, L. Wang and G. Han (2005b). "The Influence of in-plane Density Variation on Engineering Properties of Oriented Strandboard: a Finite Element Simulation." *Proceedings of McMat2005*, Baton Rouge, Louisiana, USA.
- Zhang, W., A. Drescher and D. E. Newcomb (1997). "Viscoelastic Analysis of Diametral Compression of Asphalt concrete." *ASCE Journal of Engineering Mechanics*, **123**(6): 596-603.
- Zienkiewicz, O. C. and I. C. Corneau (1974). "Visco-plasticity - plasticity and creep in elastic solids - a unified numerical solution approach." *International Journal of Numerical Methods of Engineering*, **8**(4): 821-845.

## VITA

Bing Zhang received a Bachelor of Engineering degree in Harbor and Waterway Engineering from Hohai University in Nanjing, China in July 1991 and a Master of Engineering degree in Structural Engineering from Nanyang Technological University, Singapore in February 2003. In January 2003, he entered the PhD program in Civil Engineering. He successfully defended his dissertation on May 14, 2007.